NAMSOON EOM

SURFACE FORCE MEASUREMENT BETWEEN ATOMIC LAYER DEPOSITION PREPARED HAFNIA SURFACES

SURFACE FORCE MEASUREMENT BETWEEN ATOMIC LAYER DEPOSITION PREPARED HAFNIA SURFACES

NAMSOON EOM

A thesis submitted for the degree of Doctor of Philosophy in Physics

Applied Mathematics Department

The Australian National University

August, 2017

Surface Force Measurement between Atomic Layer Deposition Prepared Hafnia Surfaces, A thesis submitted for the degree of Doctor of Philosophy in Physics,

SUPERVISOR:

Vincent S. J. Craig

DECLARATION

This thesis is an account of my own original research undertaken between August 2013 and August 2017 at The Applied Mathematics Department, School of Physics and Engineering, The Australian National University, Canberra, Australia. However, some aspects of this work were undertaken in collaboration with others. The optical reflectometry and the atomic force microscope force measurements associated with the citric acid studies were performed by Shuhei Shinohara of the Institute for Materials Chemistry and Engineering at the Kyushu University of Japan. The calculations of the van der Waals interactions in multilayered systems were performed by Dr. Drew Parsons of School of Engineering and IT, Murdoch University, Western Australia, Australia.

None of the work presented in this thesis has been submitted to any other institution for any degree or diploma. To the best of my knowledge, it contains no material previously published or written by another person, except where due reference is made in the text.

August, 2017

Namsoon Eom

ACKNOWLEDGMENTS

First and foremost, I would like to express my gratitude to my supervisor, Vincent Craig, for his endless support from beginning to end of my Ph.D.-project. As I hope he knows, his mentoring, friendship, and guidance have been essential for my completion of my project, and I consider myself lucky to have been his Ph.D.-student.

During my project, I was fortunate enough to be co-supervised by Drew Parsons and E-Jen Teh as well. They have provided solid foundations for my project, and I would like to thank them for their encouragement, training, and assistance during the last four years.

Furthermore, I would like to thank Rick Walsh for teaching me the ins and outs when it comes to laboratory work, surface science, and data analysis.

I would also like to extend my gratitude to the rest of the members of the colloid group at the Department of Applied Mathematics at ANU: Alison Sham, Jane Qian, Marie Jehannin, Matthew Quinn, Muidh Alheshibri, Shannon Notley, and Virginia Mazzini for all their help, support, and friendship during my time at ANU.

Finally, many thanks to the rest of the members of the department for collegial banter, scientific sparring, a pleasant workplace, and good times.

ABSTRACT

Surface forces play a fundamental role in colloidal systems as they control the stability, adhesion, friction and rheology of colloids. Information on all of these can be obtained from an analysis of the normal forces measured between particles. Therefore, processing of colloidal products can be informed by knowledge of the forces between the constituent particles. For wet particles systems, the interaction forces between two particles can rarely be predicted from theory; rather, it requires experimentation or direct measurement.

This requires that the surfaces used have the same surface properties as the particles. In practice this is rarely possible, as surface force measurements require surfaces with extremely low roughness and precise geometry and the majority of materials do not conform to these requirements. To address these challenges, this thesis investigates the forces measured between surfaces of low roughness and controlled chemistry produced by the use of atomic layer deposition (ALD).

This thesis reports the forces between hafnia surfaces produced by ALD and shows that like ALD produced titania surfaces and silica surfaces, the expected van der Waals forces at high pH are not manifest, suggesting that most real surfaces have unexpectedly repulsive surface forces at high pH and small separations. This will fundamentally alter how these particulate systems behave when being processed, reducing the adhesion and the friction and enhancing the stability compared to the expected interaction from DLVO theory.

Here, the interaction forces between very smooth Hafnia surfaces have been measured using the colloid probe technique and the forces evaluated within the DLVO framework, extended to include both hydration forces and the influence of roughness. The measured forces across a wide range of

pH at different salt concentrations are well described with a single parameter for the surface roughness.

These findings show that even small degrees of surface roughness significantly alter the form of the interaction force and therefore indicate that surface roughness needs to be included in the evaluation of surface forces between all surfaces that are not ideally smooth.

The knowledge gained in the first part of this work as to how to account for the roughness effect, was then applied in investigating the influence of adsorbed citric acid and palmitic acid coatings on the surface forces between hafnia surfaces. The knowledge of the surface forces and citric acid adsorption that we obtained will be useful in understanding the stability and flocculation of colloids and nanoparticles which will influence the rheology of the colloidal dispersions and the distribution of colloids and nanoparticles in the environment. The measured surface force between hafnia surfaces that are hydrophobised by palmitic acid coating promises a very easy way to hydrophobise hafnia surfaces. The investigation into the forces measured between these smooth hydrophobic surfaces provides insight into the origin of the long-ranged hydrophobic force measured between surfaces covered with a monolayer of amphiphiles. A previously unrecognized interaction mechanism of interactions between single patches formed by the mobile amphiphile has been proposed based on the measured forces.

PUBLICATIONS

Publications in peer reviewed journals:

- **Eom N**, Walsh R, Liu GM, Parsons D, Craig VSJ, "Surface forces in particle technology: Wet systems", *Procedia Engineering*, (2015), 102, 24-34

- **Eom N**, Parsons D, Craig VSJ, "Roughness in Surface Force Measurements: Extension of DLVO Theory to Describe the Forces between Hafnia Surfaces", *The Journal of Physical Chemistry B*, (2017), 121, 6442-6453, DOI: 10.1021/acs.jpcb.7b03131

- Shinohara S, **Eom N**, Teh E, Tamada K, Parsons D, Craig VSJ, "The role of citric acid in the stabilisation of nanoparticles and colloidal particles in the environment: Measurement of surface forces between Hafnium Oxide surfaces in the presence of citric acid", *Langmuir*, (2018), DOI: 10.1021/acs.langmuir.7b03116

- **Eom N**, Parsons D, Craig VSJ, "Measurement of long range attractive forces between hydrophobic surfaces produced by vapor phase adsorption of palmitic acid", *Soft Matter*, (2017), 13, 8910-8921, DOI: 10.1039/C7SM01563A

Publications not included in this thesis:

- Eom N, Parsons D, Craig VSJ, "Accurate measurement of the Young's Modulus of a single grapheme monolayer using an Atomic Force Microscope", In preparation

CONTENTS

1

2

3

CHAPTER 1

INTRODUCTION

1.1 SURFACE FORCE INTERACTIONS

Colloidal systems are ubiquitous in modern society. They are defined as systems in which one phase is dispersed in another.[1-3] There are naturally occurring colloidal materials such as fog and smoke and countless artificial ones including paints, food and cleaning products. The fact that the dispersed phase has a range of dimensions from a few nanometres to a few tens of micrometres highlights the importance of the surface properties, as a microscopic particle has a large surface to volume ratio.[4] The surface forces acting between colloidal particles is crucial in determining the behaviour of a colloidal system and knowledge of these forces is powerful from an industrial point of view because it can be applied to manipulate the system to behave in a desired way. The surface forces between colloidal particles has been investigated in many research projects and the scientific knowledge obtained has been applied to various industries for example, food science[5-6], detergency[7-9], water purification[10-11], lubricants[12-14], petroleum recovery[15], mineral processing[16-17], and pharmaceuticals[18-19].

DLVO theory[20-21] named after the four scientists, Derjaguin, Landau, Verwey and Overbeek, has been a dominating framework for interpreting the surface forces between particles in solution for more than half a century. It describes the surface forces between two similar colloidal particles as a

balance between attractive van der Waals forces and repulsive electric double-layer forces.

In terms of the experimental method, the surface force apparatus (SFA) [22-23] and atomic force microscope (AFM) [24-25] have been the two major techniques for direct surface force measurement between colloidal surfaces. Since Tabor and Winterton[22] measured the surface forces between mica sheets in 1968, several other solid surfaces such as gold[26-27], silica[28-29], zinc sulphide[30-31], polystyrene[32-34], alumina[35-36], and zirconia[37-39] have been investigated. Recently, the surface forces between air bubbles[40] and oil drops[41-42] have also been measured. In the case of solid surfaces, the main limitation in finding surfaces suitable for the direct measurement of surface forces is that the surfaces have to be extremely smooth and have geometries suitable for the chosen measurement technique in order to be able to draw meaningful interpretations from the data. Not many materials can be prepared to satisfy these conditions for surface force measurements.

1.2 OBJECTIVES AND STRUCTURES OF THE THESIS

Recently Walsh et al.[43] made a breakthrough in this conundrum by adopting the atomic layer deposition (ALD)[44-47] technique to produce atomically smooth model surfaces suitable for surface force studies. ALD is a popular thin film deposition method widely used in nanotechnology research thanks to its capability to deposit uniform and conformal films in a layer by layer fashion onto three dimensional surfaces.[44] When appropriate film growth conditions are employed, smooth amorphous films can be grown.[43, 48]

Subsequently, the surface force between ALD prepared titanium oxide, also known as titania, surfaces in aqueous solution were successfully measured and were compared with the theoretically predicted dispersion forces and fitted using the DLVO theory.[49] An interesting result was obtained at high pH where the measured surface force was repulsive at small separations between two surfaces, whilst the DLVO theory predicted a large attractive force. It is well known that DLVO theory has a limited applicability.[50]

For instance, it does not take into account specific ion effects which are ubiquitous and it cannot be applied at high salt concentrations.[51] It often disagrees with experimental results and as a result the unexplained forces have been categorized as non-DLVO forces[52]. The repulsive force observed between titania surfaces also contradicts the theory. [49, 53] According to DLVO theory, any short-range repulsive force should be masked by the large attractive force due to the strong van der Waals forces associated with the high dielectric constant of titania.

In order to find out whether this unexplained phenomenon is peculiar to titania[49, 53] or occurs rather generally we will investigate other mineral oxide surfaces. We have chosen hafnium oxide, also known as hafnia, as it has a high dielectric constant and is a material available to us through the ALD technique. To date the surface force between hafnia surfaces have never been measured.

Hafnia has a wide number of applications that make use of the high chemical and thermal stability, as well as a relatively high dielectric constant and a high refractive index. It has been extensively studied as an alternative gate dielectric material in metal-oxide-semiconductor field effect transistors, to solve the leakage current problem found in silica.[54-57] Hafnia has also been employed in advanced ceramics that are found in various applications such as cutting tools[58], nanofiltration membranes[59-60], and thermal barrier coatings in engine[61]. The use of hafnia is expanding as the demand for higher fracture resistant ceramics is increasing. The colloidal processing of ceramics[62] is where defects can be introduced and thus the strength of ceramic materials is often determined at this stage.[63] In general, repulsive forces between colloidal particles facilitate stable suspensions and thus good mixing of different particles.[62] The potential outcomes of this work will not only be an elucidation of the anomalous repulsive force between titania[49, 53] surfaces but also a greater understanding of the behaviour of hafnia colloidal systems, which will be valuable in various applications. Further, we expect that we might obtain a deeper understanding of colloidal interactions in general and therefore contribute to understanding colloidal systems not directly investigated here.

In Chapter 2, background information on surface forces is presented, in particular, the DLVO theory is described. An overview of the popular surface force measurement techniques is also presented.

In Chapter 3, the experimental methodology of the work presented in this thesis is explained including atomic layer deposition (ALD) and atomic force microscopy (AFM).

In Chapter 4, experimental results from the measurement of the surface forces between ALD prepared hafnia surfaces are presented and discussed. In particular the effect of roughness on surface forces is investigated and quantified.

In Chapter 5, the effect of citric acid on the surface forces between hafnia surfaces is investigated. Citric acid as an effective stabilizer for metal oxide particles is demonstrated. Importantly, the influence of the adsorption of citric acid (which is a model for humic and fulvic acids) on the flocculation properties of nanoparticles, and thus, in turn, on the transport of engineered nanoparticles in the environment is discussed.

In Chapter 6, the surface forces between hafnia surfaces that are hydrophobised by palmitic acid vapor treatment are presented. A simple method is developed to hydrophobise hafnia surfaces, and the forces measured are discussed. A new mechanism for the anomalous attraction between such hydrophobic surfaces is proposed, which quantitatively fits the measured interactions.

In Chapter 7 provides a brief summary of the entire work and the important conclusions and describes future directions for this research.

This work aims to contribute to a deeper understanding of surface forces in general and the specific properties of a range of previously unexplored surfaces by using the ALD technique. A series of successful employments of ALD in surface force studies may promote a wide usage of the technique, which in return will enrich our knowledge in colloidal science.

CHAPTER 2

INTRODUCTION TO SURFACE FORCES

This chapter provides an introduction to the theory of surface forces, focusing on the DLVO theory[20-21] of colloidal stability. It begins with an introduction of the two forces that comprise DLVO force: the van der Waals force and the electric double layer force. This chapter also touches on other non-DLVO forces that have been experimentally measured and on some of the popular surface force measurement techniques.

2.1 SURFACE FORCES

The properties of colloidal systems are largely dictated by the interactions between the colloidal particles in close proximity: the so-called surface forces[4, 64-66]. The surface forces include van der Waals forces[67], electric double layer forces[68], hydrophobic force[69-70], hydration force[71-72], steric force[73-74] and so on. We begin with the origin of the ubiquitous van der Waals force.

2.2 VAN DER WAALS FORCES

2.2.1 *Van der Waals forces between molecules*

One of the most important forces in surface and colloid science is the van der Waals forces between atoms, molecules, or particles. Named after the Dutch scientist Johannes Diderik van der Waals who first recognized the evidence of forces between what were soon to be called molecules. In his 1873 Ph.D. thesis[75], van der Waals extended the famous ideal gas law, $pV = Nk_BT$, the relationship between the pressure, p, volume, V, and temperature, T, of dilute gases of non-interacting point particles. Here, N is a given number of particles and k_B is the Boltzmann constant. Van der Waals found that to describe dense-gas pressures, he had to replace $pV = Nk_BT$ with:

$$\left[p + \left(\frac{a}{V^2}\right)\right](V - b) = Nk_BT \tag{2.1}$$

The net volume V became $(V - b)$, with a positive constant, b, that accounts for the small space occupied by the gas particles themselves. And with constant positive a, the pressure, p, of the dense-gas was less than the pressure of the ideal gas by an amount $\frac{a}{V^2}$. This difference implied that there are attractive forces between gas molecules. Such an attraction is also evident at cold temperatures when these same gasses liquefy.

After the 1870's formulation of the van der Waals gas equation, there was rapid progress in the study of the interactions between particles in gases. By the end of the 1930s, three kinds of dipole–dipole interactions were formulated for neutral-molecule interactions. In all three cases, the free energy, the work required to bring the gas particles from infinite separation to a finite separation, x, was found to vary as the inverse-sixth power of distance, - (C/x^6), with different positive coefficients C:[67]

1) Keesom interactions of permanent dipoles, - (C_{Keesom}/x^6). Two freely rotating dipoles will attract each other because they change orientation such that they are anti-parallel.

2) Debye interactions between a permanent dipole and a nonpolar molecule, - (C_{Debye}/x^6). The permanent dipole polarizes the nonpolar molecule, with the induced dipole being anti-parallel resulting in an attraction.

3) London dispersion interactions between two nonpolar but polarizable molecules, - (C_{London}/x^6). Momentary dipoles on one molecule can induce dipoles on another molecule giving rise to an attraction. The condensation of nonpolar gases is evidence of this interaction.

Keesom and Debye interactions can be calculated using classical physics. However, as the London dispersion force[76] (also called the dispersion force) is quantum mechanical in origin, calculating it requires quantum mechanical perturbation theory[77]. The origin of dispersion forces can be understood intuitively by considering the electrons around an atom at a very high frequency.[64] The dipole moment is zero for nonpolar atoms when averaged over time, however, at any given moment atoms have a dipole moment due to the instantaneous positions of the electrons. This dipole generates an electric field that induces a dipole in nearby atoms. As a result, an attractive force arises between the two atoms.

The van der Waals force is the sum of the Keesom, the Debye, and the London dispersion interaction: [67]

$$V_{vdW}(x) = -\frac{C_{Keesom} + C_{Debye} + C_{London}}{x^6} \qquad (2.2)$$

In the absence of strong molecular dipoles, such as in water, the dispersion interaction is usually the dominating force.[68]

2.2.2 *Van der Waals forces between macroscopic particles*

2.2.2.1 *Microscopic calculation: Hamaker approach*

In 1937 H. C. Hamaker[78] formulated van der Waals interactions between macroscopic particles, as distinct from the small-molecule interactions that had been considered previously. His calculation was based on the pairwise summation of the forces between all molecules in the particles. This is often called the microscopic approach because the calculation involves the polarizabilities and number densities of the atoms in the two interacting bodies.[79] Hamaker's approach assumes that the interaction between a pair of molecules is not influenced by the presence of a third molecule. He showed that the distance dependency of the van der Waals forces can be much longer ranged than the r^{-6} dependency exhibited by single molecules. According to Hamaker, the interaction energy per unit area, W, between two flat surfaces at a distance x is given by:

$$W(x) = -\frac{A_H}{12\pi x^2} \tag{2.3}$$

Here, A_H is the so-called Hamaker constant, and the van der Waals interaction energy per unit area $W(x)$ is derived by summing all the interactions between atomic and molecular dipoles in the particles. This approach by Hamaker is, however, questionable as it neglects many body effects.

2.2.2.2 *Macroscopic calculation: Lifshitz theory*

In 1956, Lifshitz[80] published a paper presenting an alternative, more rigorous and accurate calculation of the van der Waals force between solid bodies. Lifshitz showed that instead of summing pair-wise interatomic forces, one can treat matter as a continuum with certain dielectric properties, avoiding the calculation of the complicating many body effects. In the Lifshitz theory,

the fluctuations in the electromagnetic field between two macroscopic bodies separated by the medium results in the van der Waals interaction.

Lifshitz theory leads to an interaction that is reasonably well described by Equation 2.3, but is different from the Hamaker approach in determination of the Hamaker constant, A_H and the interaction decays more rapidly at larger separations due to the finite time required for the electromagnetic field to travel between molecules. This is known as retardation. The retardation effect was introduced by Casimir and Polder[81] in 1948, as the weakening of the interaction forces at larger separations. It arises from the finite amount of time for the electromagnetic field to propagate from one charge to the other. The retardation effect becomes significant when the distance between fluctuating charges is large enough. At large distances, by the time the second charge responds to the field generated by the first one, the momentary charge configuration of the first charge will have changed, and the charge fluctuations will fall out of step with each other. As a result, the strength of interaction is always weakened.[67] When the retardation effect is taken into account, the Hamaker constant, A_H, becomes the separation-dependent Hamaker coefficient, $A_H(x)$.

In Lifshitz theory, the Hamaker constant is calculated from the bulk dielectric and magnetic properties of the materials. The complicated structure of Lifshitz theory and the necessity of knowing the dielectric response function for the full range of relevant frequencies hindered its widespread acceptance. In 1969, Parsegian and Ninham[82] showed that application of Lifshitz theory could be simplified by constructing the dielectric function by interpolating the available spectral data. This paved the way for easier access to quantitative description of the van der Waals forces.

The Hamaker constant A_{132} for two half-spaces made of materials 1 and 2 separated by an intervening medium 3 is given by Equation 2.4.[80,82] Note that the magnetic contribution is not included in the equations below as it is negligible compared to the dielectric for most materials.

$$A_{132} = \frac{3}{2} k_B T \sum_{m=0}^{\infty\prime} \int_0^{\infty} x \ln(1 - \Delta_{13}\Delta_{23} e^{-x}) dx, \tag{2.4}$$

Here, Δ refers to the dielectric reflection coefficient between the medium and the materials. The prime against the summation in m indicates that the zero frequency term in m=0 is taken with a factor of 1/2. The zero frequency term corresponds to the sum of the Debye and Keesom interactions, which makes only a minor contribution to the total interactions except in materials with large permanent dipole moments. Taken between two whole materials j and k, the dielectric reflection coefficient, Δ_{jk}, at an imaginary frequency $i\omega$ is:

$$\Delta_{jk} = \frac{\varepsilon_j(i\omega_m) - \varepsilon_k(i\omega_m)}{\varepsilon_j(i\omega_m) + \varepsilon_k(i\omega_m)} \tag{2.5}$$

with

$$\omega_m = \frac{2\pi m k_B T}{\hbar} \quad \text{with } m = 1, 2, 3, 4, \ldots \tag{2.6}$$

$\varepsilon(i\omega)$ is the imaginary dielectric response function[82] of the Matsubara frequencies ω_m. The introduction of the imaginary dielectric function, $\varepsilon(i\omega)$ is a purely mathematical procedure and thus $\varepsilon(i\omega)$ itself is not a physical property of the materials but can be calculated from the real physical adsorption spectrum, which is the imaginary part of the frequency-dependent complex dielectric function $\varepsilon(\omega)$ of the materials. Today, the complex dielectric function $\varepsilon(\omega)$ can be determined from the dielectric data obtained using various techniques such as optical reflectance, ellipsometry, and electron loss spectroscopy. Although most of these methods yield only one of the components of the complex dielectric function, the transformation from the real to the imaginary component or vice versa can be performed using the Kramers-Kronig (K-K) relations.

In this thesis, the van der Waals interaction for the layered system was calculated using Lifshitz theory[83]. See Appendix-A (§A.2) for details of the van der Waals interaction between multilayered systems.

2.3 ELECTRIC DOUBLE-LAYER FORCE

Most solid surfaces are found to develop some type of electric charge when in contact with water or any liquid of high dielectric constant.[84-85] The presence or absence of a surface charge may not be important in macroscopic systems. However, in the microscopic world of colloids, the presence or absence of even a small surface charge can have significant impact on the stability of the system.[20, 86-88]

A surface may acquire an electric charge by the following mechanisms:[64]

1) Direct ionization or dissociation of surface groups: surface groups can be directly ionized, but one of the ions can be permanently bound to the surface.
2) Adsorption or binding of ions from solution: for example, the adsorption of $-OH^-$ groups to the water-air interfaces that charges it negatively.
3) Charge (usually protons or electrons) hopping between two dissimilar surfaces without a liquid medium.

In all three mechanisms of charging, the final surface charge of co-ions is balanced by an equal but oppositely charged region of so-called counterions as illustrated in Figure 2.1. Here, some of the counterions are bound to the surface within the so-called Stern or Helmholtz layer.[89] However, thermal fluctuations tend to drive some counterions away from the surface. This leads to the formation of an electric double-layer.[90-91]

To examine how these surface charges affect the properties of colloids, it is first necessary to invoke the famous Coulomb's law. It describes the inverse square law of force between two electric charges, q_1 and q_2, separated by a distance, x, in a medium in the form:

$$F(x) = \frac{q_1 q_2}{4\pi\varepsilon\varepsilon_0 x^2} \tag{2.7}$$

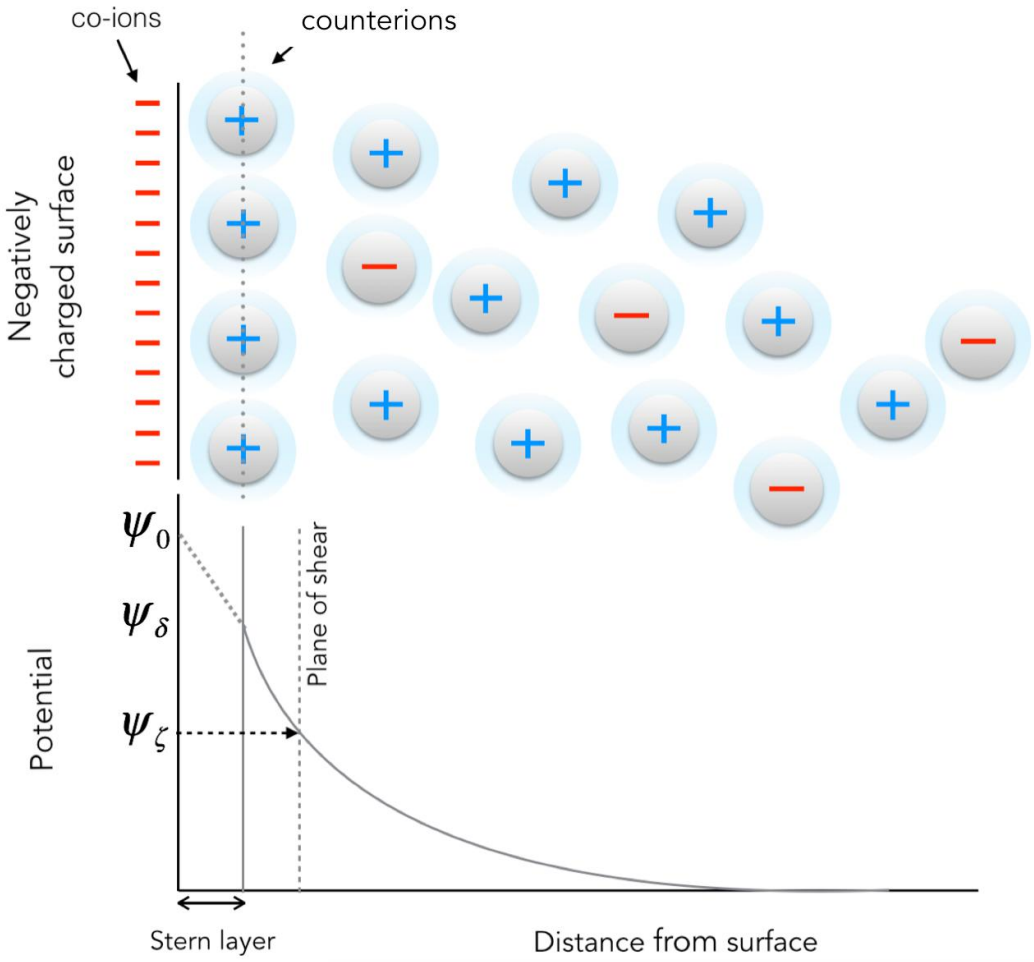

Figure 2.1: Schematic of an electric double layer at a charged surface. The surface charge generates a surface potential ψ_0. On the Stern layer, the adsorbed counterions change the potential to ψ_δ. The zeta potential, ψ_ζ, is where the electric double layer begins.

where ε_0 is the permittivity of a vacuum and ε is the dielectric permittivity or constant of the medium. The work done to bring two charges together from infinite separation to a distance x in a medium is therefore given by:

$$W(x) = \frac{q_1 q_2}{4\pi\varepsilon\varepsilon_0 x} \tag{2.8}$$

$W(x)$ will be positive for charges of the same sign, and negative for charges of opposite sign. If a charge q produces an electric field at a point x, then the work needed to bring a unit charge to this point is $q/(4\pi\varepsilon\varepsilon_0 x)$. This is called the electric potential at x due to the charge q and is denoted by ψ.

2.3.1 *The Poisson–Boltzmann equation*

Coulomb's law is applicable to simple systems. However, for more realistic situations, the presence of all ions in the system must be taken into consideration. Therefore, in order to apply Coulomb's law to solutions of electrolytes and colloids that contain dissolved ions, and charged surfaces, it is necessary to employ Boltzmann's distribution law. In the coming section (§2.3.1.1) a summary of the derivation of the electric potential ψ near a charged planar surface using the Poisson equation and Boltzmann's distribution law is given as explained by Butt and Kappl.[68]

2.3.1.1 *Linearized Poisson-Boltzmann equation for low potential*

The potential, ψ, near a charged planar surface depends on the distance normal to the surface x. Thus, we consider a planar solid surface with a homogeneously distributed electric surface charge density, σ, in contact with a liquid. The surface charge generates a surface potential ψ_0 at $x = 0$.

In general, charge density and electric potential are related by the Poisson equation:

$$\nabla^2\psi = -\frac{\varrho_e}{\varepsilon\varepsilon_0} \tag{2.9}$$

Here, ϱ_e is the local electric charge density. If the exact charge distribution is known, then the potential distribution can be calculated using the Poisson equation. However, because the ions in solution are free to move, their spatial distribution needs to be calculated using Boltzmann statistics. According to the Boltzmann equation, the local ion density c_i is given by:

$$c_i = {c_i}^0 \cdot \mathrm{e}^{-\frac{W_i}{k_B T}} \tag{2.10}$$

where W_i is the work required to bring an ion in solution from infinite distance to a certain position near the surface, and ${c_i}^0$ is the bulk concentration of the given ion. This shows that the local ion concentration c_i depends on the electric potential at a certain position.

Now, if we assume that only 1:1 salt is dissolved in the liquid, the electric work required to bring a charged cation to a place with potential ψ is $W^+ = e\psi$, where e is the unit charge. For an anion, it is $W^- = -e\psi$. The local anion and cation concentrations c^- and c^+ are related to the local potential, ψ, by the Boltzmann factor: $c^- = c_0 \cdot \mathrm{e}^{e\psi/k_B T}$ and $c^+ = c_0 \cdot \mathrm{e}^{-e\psi/k_B T}$. Here, c_0 is the bulk concentration of the salt. Then the net local charge density is

$$\varrho_e = e(c^+ - c^-) = c_0 e \cdot \left(\mathrm{e}^{-\frac{e\psi(x,y,z)}{k_B T}} - \mathrm{e}^{\frac{e\psi(x,y,z)}{k_B T}}\right) \tag{2.11}$$

Substituting Equation 2.11 into the Poisson equation 2.9 leads to

$$\nabla^2\psi = \frac{c_0 e}{\varepsilon\varepsilon_0} \cdot \left(\mathrm{e}^{-\frac{e\psi(x,y,z)}{k_B T}} - \mathrm{e}^{\frac{e\psi(x,y,z)}{k_B T}}\right) \tag{2.12}$$

Often, this equation is referred to as the Poisson-Boltzmann equation. It is a partial differential equation of second order, and in most cases, it has to be solved numerically. However, in the case of a planar surface, it can be solved analytically. For the simple case of an infinitely extended planar surface, we are left with the Poisson-Boltzmann equation in the x - direction only:

$$\nabla^2\psi = \frac{\partial^2\psi}{\partial x^2} = \frac{c_0 e}{\varepsilon\varepsilon_0}\cdot\left(\mathrm{e}^{-\frac{e\psi(x)}{k_B T}} - \mathrm{e}^{\frac{e\psi(x)}{k_B T}}\right) \tag{2.13}$$

For low potentials, we can expand the exponential functions into a series and neglect all but the first linear term:

$$\frac{\partial^2\psi}{\partial x^2} = \frac{c_0 e}{\varepsilon\varepsilon_0}\cdot\left(1 + \frac{e\psi}{k_B T} - 1 + \frac{e\psi}{k_B T} \pm \cdots\right) \approx \frac{2c_0 e^2}{\varepsilon\varepsilon_0 k_B T}\cdot\psi \tag{2.14}$$

Note that low potential means, $e|\psi| \ll k_B T$. At room temperature, this implies that $\psi \leq 25$ mV. Fortunately, in most applications, the result is valid even for higher potentials, up to 50 - 80 mV. The Equation 2.14 is sometimes called the "linearized Poisson-Boltzmann equation" or "Debye-Hückel approximation". The general solution of Equation 2.14, the linearized Poisson-Boltzmann equation, is

$$\psi(x) = A\cdot\mathrm{e}^{-\kappa x} + B\cdot\mathrm{e}^{\kappa x} \tag{2.15}$$

with

$$\kappa = \sqrt{\frac{2c_0 e^2}{\varepsilon\varepsilon_0 k_B T}} \tag{2.16}$$

Here, A and B are constants, which are defined by the boundary conditions. The boundary conditions require that, at the surface, the potential is equal to the surface potential, $\psi(x = 0) = \psi_0$, and that far away from the surface, the potential should disappear $\psi(x \to \infty) = 0$. This condition leads to $B = 0$. From the first boundary condition, we get $A = \psi_0$. Thus, the potential is given by

$$\psi = \psi_0 \cdot e^{-\kappa x} \tag{2.17}$$

The potential decreases exponentially with the decay length $\lambda = \kappa^{-1}$. This decay length is called the Debye length. It indicates how fast the surface potential decays. As seen in the Equation 2.16, the Debye length is inversely proportional to the salt concentration. This is easily understood as the greater concentration of ions in solution, the more effective the screening of the surface charge.

2.3.2 *Interacting double layers*

In the previous section, we dealt with the potential distribution around an isolated charged surface by considering a simple planar surface. Now if two charged surfaces approach each other, then the electric double layers overlap, and an electric double-layer force will arise. This electric double-layer force is essential for the stabilization of colloid systems.[92]

Several methods are available for calculating the interaction energy of two electric double layers. For example, Hogg, Healy, and Fuerstenau[93] formulated the change in Gibbs energy of the two double layers with constant, but different surface potentials. Parsegian and Gingell[94] calculated the osmotic pressure for two different surfaces.

To calculate the potential distribution in the gap between two double layers, we need the Poisson-Boltzmann equation. However, we need to alter the boundary conditions from our previous derivation. Two types of boundary conditions are of interest:[64, 68]

1) Constant potential: During approach, the surface potentials of two surfaces remain constant:
2) Constant charge: During approach, the surface charge densities of two surfaces remain constant.

The force per unit area can be written in a very simple form when the separations between two double layers are large enough ($\kappa x > 1$) : [95]

$$F(x) \approx f \cdot \mathrm{e}(-\kappa x) \tag{2.18}$$

Here the prefactor f is some function of the surface charge or potential and κ^{-1} is the Debye length, which depends on salt concentration and is an indication of the range of the double layer force. Note that at smaller separations, however, the calculation becomes very complicated and the assumptions of the model might become invalid.[95] In the case of real surfaces, neither the surface charge nor the surface potential remains constant. For instance, when two surfaces are forced into contact the counterions are forced to re-adsorb onto their original surface sites. Thus, the surface charge becomes a function of the distance between the two surfaces. This is known as charge regulation.[96-97] This regulation leads to forces that lie between the two theoretical limits set by the constant charge and constant potential boundary conditions.[64]

To analyze the electric double layer forces measured in this thesis, we used an algorithm developed by Chan, Pashley and White[98] that calculates the interaction energy of the repulsion between two flat surfaces of the same potential. The numerical procedure in this algorithm starts from the planar Poisson-Boltzmann equation for a 1:1 electrolyte solution presented earlier in Equation 2.13 which can be re-written as Equation 2.19 with a dimensionless potential $\Psi \equiv e\psi/k_B T$

$$\frac{\partial^2 \Psi}{\partial x^2} = \frac{c_0 e^2}{\varepsilon \varepsilon_0 k_B T} \cdot (\mathrm{e}^{-\Psi} - \mathrm{e}^{\Psi}) \tag{2.19}$$

Below is a summary of the algorithm developed by Chan, Pashley and White.[98] Equation 2.19 can be simplified as

$$\frac{\partial^2 \Psi}{\partial X^2} = \sinh \Psi \tag{2.20}$$

where $X\,(\kappa x)$ is the scaled distance measured from the midplane, and κ is the inverse of Debye length. A first integration of Equation 2.20 gives

$$\frac{d\Psi}{dX} = Q\ \mathrm{Sgn}\ (\Psi_m) \tag{2.21}$$

where Sgn is the sign function taking values of either -1 or +1, and the variable Q is defined as

$$Q = \sqrt{2(\cosh \Psi - \cosh \Psi_m)} \tag{2.22}$$

where Ψ_m is the scaled midplane potential, which emerges as an integration constant. Equation 2.21 satisfies the symmetric zero-derivative boundary condition at the midplane ($X = 0$). We calculate $\frac{dQ}{d\Psi}$ using the chain rule and remembering the hyperbolic identity ($(\cosh \Psi)^2 - (\sinh \Psi)^2 = 1$) we derive that

$$\frac{dQ}{d\Psi} = \frac{\sinh \Psi}{Q} = \frac{\mathrm{Sgn}\,(\Psi_m)}{Q}\sqrt{\left(\frac{Q^2}{2} + \cosh \Psi_m\right)^2 - 1} \tag{2.23}$$

By multiplying Equations 2.21 and 2.23 we derive the differential equation

$$\frac{dX}{dQ} = \sqrt{\left(\frac{Q^2}{2} + \cosh \Psi_m\right)^2 - 1}^{-1} \tag{2.24}$$

The midplane in terms of these variables is the point (Q = 0, X = 0). If we know what value of Q corresponded to the surface charge (Q_s), then for a given value of the reduced midplane potential Ψ_m, we can solve Equation 2.24 from Q = 0 to $Q = Q_s$ by a suitable numerical technique for solving differential equations. Thus we determine $X_s = \kappa L/2$, the scaled distance from the midplane to the surface of charge corresponding to the given value of Ψ_m, where $L/2$ is the distance from the midplane to each surface. Repeating this procedure for a set of suitably chosen values of Ψ_m will generate a set of corresponding $\kappa L/2$ values, which we can compare to the measured separations. The electrostatic pressure at each value of L is simply calculated from the corresponding Ψ_m value by[21, 64]

$$P(L) = 2nk_BT(\cosh \Psi_m - 1) \tag{2.25}$$

The interaction free energy per unit surface area $E_p(L)$ can be computed from

$$E_p(L) = \int_L^\infty P(L')dL' \tag{2.26}$$

In the case of constant surface potential, Q_s is calculated directly from Equation 2.22 with $\Psi = \Psi_s$,

$$Q_s = \sqrt{2(\cosh \Psi_s - \cosh \Psi_m)} \tag{2.27}$$

In the case of constant surface charge, we have Gauss' boundary condition with surface charge density, σ

$$\frac{d\Psi}{dX} = \frac{4\pi e}{\epsilon k_B T} \cdot \sigma \tag{2.28}$$

From Equation 2.21 we see immediately that

$$Q_s = \frac{4\pi e}{\epsilon k_B T} |\sigma| \tag{2.29}$$

Most surfaces will fall somewhere between these boundary conditions.

Note that when the measured force was suspected to be an attractive force between surfaces with two different potentials, we used the method of Parsegian and Gingell[94] (See § 4.2.7.1).

2.4 DLVO THEORY

The van der Waals force and the electric double layer force that were covered in previous sections are the two forces acting between charged surfaces according to the famous DLVO theory. This theory was developed independently by Deryaguin and Landau in 1941[20] and E. J. W. Verwey and J. T. G. Overbeek in 1948[21]. DLVO theory was developed to quantitatively explain the coagulation of dispersed particles in aqueous solution. The theory describes the interplay between the van der Waals attraction that causes aggregation while the double layer force promotes stabilization.

Figure 2.2 shows the interaction energy between two identical surfaces calculated with the DLVO theory. Depending on salt concentrations and surface potential, there can be three force regimes: a very weak attraction (secondary minimum) at large separations, a double-layer repulsion at intermediate separations, and a strong attraction at short separations (primary minimum).

At low salt concentrations or at high surface potentials, the repulsive double layer force will prevent the particles from aggregating. This repulsive energy barrier can be so high that the thermal energy of the particles cannot overcome it.[66] This will lead to a stable colloid dispersion.

As the salt concentration increases or the surface potential decreases, however, the repulsive energy barrier decreases. At high salt concentration or at low surface potential, this barrier becomes small and the van der Waals attraction dominates and aggregation of the particles in suspension will occur. Note that the van der Waals force between two identical surfaces is al-

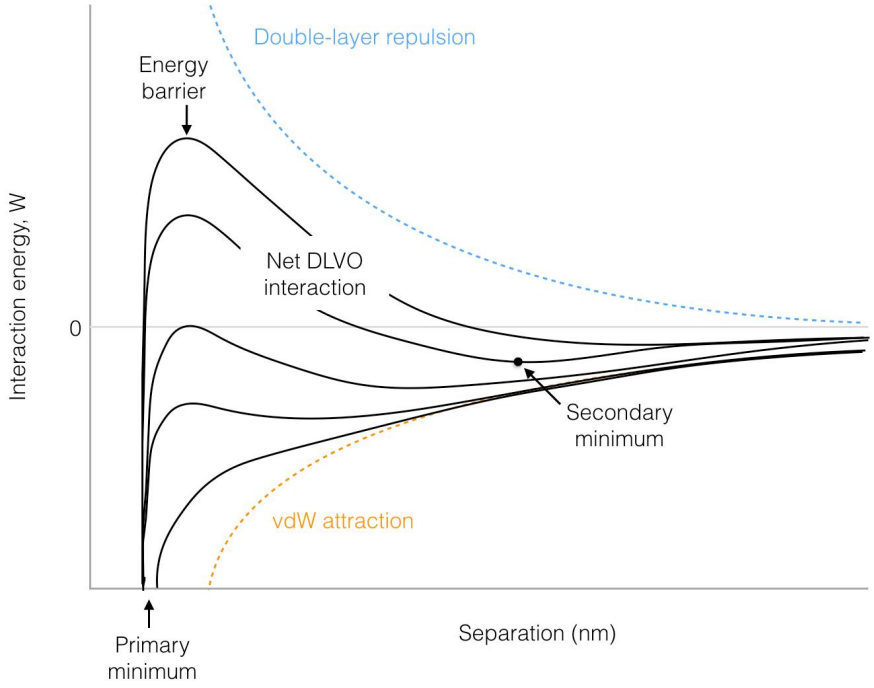

Figure 2.2: Schematic of the net DLVO interaction (black solid line) as well as the electric double layer (blue dotted line) and van der Waals (orange dotted line) components between two identical surfaces as a function of separation.

ways attractive regardless of the medium in the gap.[99] A very important feature to notice here is that when the separation becomes very small DLVO theory predicts that the van der Waals attraction *always* dominates.

The secondary minimum can exist at large separations.[100] It can lead to a weak, reversible coagulation.[101-102]

In describing colloid stability, DLVO theory makes several assumptions.[103] Worth noting here are:

1) The solid surfaces are smooth at the molecular level.
2) An intervening medium is described by dielectric properties, has no granularity and has bulk properties up to the interface.
3) The electric double layer and van der Waals forces are treated independently and assumed additive.
4) The double layer interaction potential is computed using the non-linear Poisson Boltzmann equation for point ions. The discrete nature of charge is ignored and the smeared out surface charge approximation is applied.

When DLVO theory deals with long-range forces that are essential to explain the lyophobic colloid stability which was the original intention of the theory, the above assumptions present few problems.[103] It has been, indeed, the dominating paradigm in colloid stability for almost 70 years.

2.5 THE DERJAGUIN APPROXIMATION

In the previous derivation, the interaction was expressed as interaction energies rather than the forces experienced by molecules and small particles. Theoretically, it is easier to calculate the interaction free energy per unit area, $W_a(x)$, between two parallel planar surfaces.[64] Experimentally, however, it is usually easier to measure the forces, $F(x)$, between two curved bodies as a function of their surface separation x, which is size and geometry dependent. Therefore, it is desirable to have a method to relate the interaction force to the interaction energy.

In 1934, Derjaguin[104] proposed that many kinds of interaction, between spheres or between a sphere and a plane or between any curved surfaces, could be derived from an expression for the interaction between two parallel planar surfaces. Below is the derivation that shows how to relate the energy per unit area for two flat surfaces to the force between two spheres.[105]

Assume that we have two spherical particles of radii R_1 and R_2 at a surface separation x apart, as illustrated in Figure 2.3. The total surface forces, $F(x)$, between these two particles can be obtained by integrating the forces

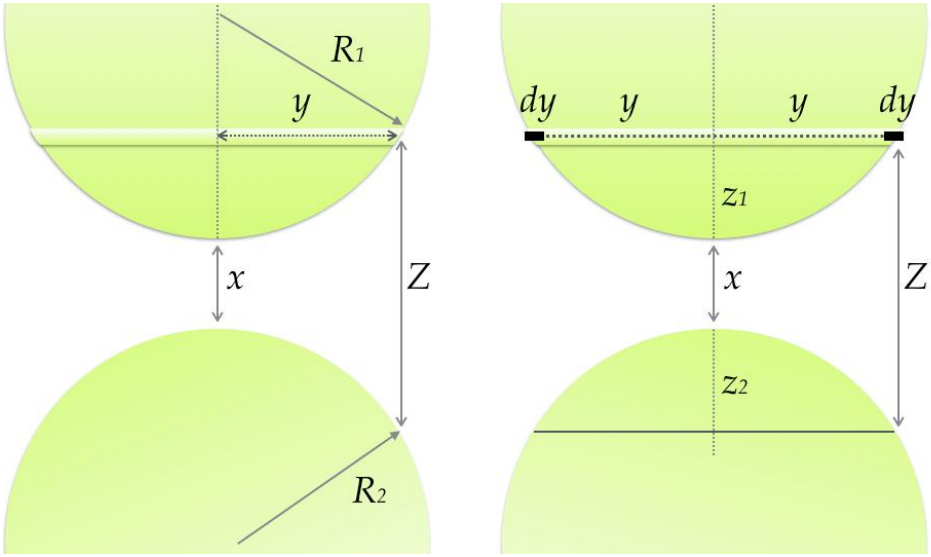

Figure 2.3: Schematic of two spherical particles of radii R_1 and R_2 at a surface separation x apart

between a circular element strip of area, $2\pi ydy$, on the upper surface and the lower surface,

$$F(x) = \int_{Z=x}^{Z=x+R_1} (2\pi ydy) f(Z) \tag{2.30}$$

where, $f(Z)$, is the force per unit area. Now we take several approximations in deriving the $F(x)$- $W_a(x)$ relation.

First, we divide the surface of the first sphere (R_1) into infinite number of rings, so that each circular strip becomes a flat ring of width dy. Replace the second sphere (R_2) with an infinite flat surface at the separation Z directly opposite to the flat rings, which is a reasonable approximation for R_1, $R_2 \gg x$. Now, we take the "Chord Theorem" approximation, in which the surface curvature is assumed to be parabolic. Then the following relation holds true for all separations,

$$R_1{}^2 = (R_1 - z_1)^2 + y^2 \tag{2.31}$$

and for $R_1 \gg x$ (and thus $R_1 \gg z_1 \gg z_1{}^2$), this gives,

$$z_1 \approx \frac{y^2}{2R_1} \tag{2.32}$$

and similarly,

$$z_2 \approx \frac{y^2}{2R_2} \tag{2.33}$$

Thus,

$$Z = x + z_1 + z_2 \approx x + \frac{y^2}{2R_1} + \frac{y^2}{2R_2} \tag{2.34}$$

Differentiating Z with respect to y gives,

$$dZ = \frac{y}{R} dy \tag{2.35}$$

where

$$R = \frac{R_1 R_2}{R_1 + R_2} \tag{2.36}$$

Substitution of Equations 2.35 and 2.36 into Equation 2.30 leads to

$$F(x) = 2\pi R \int_{Z=x}^{Z=x+R_1} f(Z)dZ \tag{2.37}$$

Now we assume that the range of surface force is small compared with the size of the two spheres, which is a reasonable assumption in practice. Then, we can replace the upper integration limit in Equation 2.37 with infinity. This gives:

$$F(x) = 2\pi R \int_{x}^{\infty} f(Z)dZ = 2\pi R W_A(x) \tag{2.38}$$

where $W_A(x)$ is the interaction free energy between a unit area and a semi-infinite surface x apart. Now, we can assume that the interaction free energy between two unit areas $W_a(x)$, is very similar to $W_A(x)$, which is a very good approximation for surfaces in close proximity. And, we finally arrive at the Derjaguin approximation, [104]

$$F(x) = 2\pi R W_a(x) \tag{2.39}$$

Although Equation 2.39 has been derived for two spheres, it can be easily adapted to other geometries. In case of a sphere of radius R_1 against a planar surface (as in the colloid probe AFM technique that this thesis employed), we set $R_2 \gg R_1$ in Equation 2.36, and it gives [64, 68, 105]

$$F(x) = 2\pi R_1 W_a(x) \tag{2.40}$$

The Derjaguin approximation is applicable to any type of force law as long as the range of the interaction and the separation x are much smaller than the radii of the spheres. It is useful for comparing experimental data with theory. It is also useful for comparing force data among different experiments, since all forces can be scaled by a simple geometric factor that depends only on the local radii of the interacting surfaces.[64]

2.6 NON-DLVO FORCES

The force between two solid surfaces can usually be described by DLVO theory based on continuum models for large separations. However, the continuum theory eventually breaks down at small surface separations,[68] at which point the molecular nature of the intervening liquid medium has to be taken into account. It is, therefore, not surprising to find some phenomena that cannot be explained by DLVO theory. We briefly discuss some of the phenomena that are caused by the discrete nature of liquid molecules in the following section.

2.6.1 *Hydration force*

When two hydrophilic surfaces are brought into contact, repulsive forces have been measured in aqueous solution. The short range repulsive force has been experimentally measured in aqueous electrolytes between a variety of surfaces both soft[106-110] and hard such as alumina[36], mica[72, 111], and silica[28, 112-113]. This force arises between two surfaces when water molecules bind strongly to molecules at the surfaces. The repulsive force has been described by the energy required to remove the water layer from the hydrated surfaces or from ions adsorbed to the surface. The hydration force could explain a range of natural phenomena, such as swelling of certain clays and repulsion between biological membranes.[105]

Measured hydration forces are found to decay exponentially with a decay length comparable to the size of water molecules, but with widely differing magnitudes.[71] As it decays quite rapidly, the force is observed at separations only up to a few nm.[64]

To date, despite extensive research in the field, a dominant theoretical description of the hydration force has not emerged although several theoretical models have been proposed.[114-116] In analysing the surface forces measured between hydrophilic hafnia surfaces in Chapter 4, I used the model developed by Marcelja and Radic[115] who explained the short-range repulsion by a modification of water structure near hydrophilic surfaces.

2.6.2 *Hydrophobic force*

The strong attraction between hydrophobic surfaces in water, which is now termed the hydrophobic interaction or force[69-70, 117] has been of significant interest to many theoretical and experimental scientists, since the first experimental result of the distance dependence of this force reported an exponentially decaying attractive force with a long-ranged decay length (~ 1 nm)[118]. Direct measurements of the interaction between hydrophobic surfaces were performed typically between mica surfaces that were rendered hydrophobic by adsorption of surfactants[118-119], Langmuir-Blodgett deposition[120-121], and by chemisorption[122-124]. Although the long-range exponentially decaying attractive force between hydrophobic surfaces in water is now well acknowledged, to date the reported range and magnitude of the hydrophobic force varies significantly depending on the physical system and the measurement methods.[69]

One of the major sources of disagreement in the experimental results is the dependence of the attractive force on the hydrophobic surface preparation technique. Forces measured between relatively smooth and stable hydrophobic surfaces produced by chemisorption have been reported to be in a range of < 10-20 nm[125-126] , whereas surfaces prepared by physisorbed surfactants resulted in longer ranged forces (> 20 nm) [70, 126]. Complexity often arises in measuring and interpreting the hydrophobic force due to other factors such as surface roughness and surface nanobubbles[127-131]. Preparing robust, smooth, and molecularly well-defined hydrophobic surfaces is therefore crucial.

I investigate the interaction between hafnia surfaces hydrophobised using palmitic acid vapor treatment in Chapter 6.

2.6.3 *Steric force*

A stabilized colloid can be observed when the particles are covered with a dense polymer layer,[73, 132, 74] either through adsorption or through chemical grafting. If two particles approach, the polymer layers will touch when the

separation between them becomes less than twice the polymer layer thickness. In a good solvent for the polymer[133], the local increase in polymer concentration gives rise to a repulsive steric interaction between the particles. This repulsion is called a steric force.[134-135] A short-range steric repulsion can also arise from the adsorption of small molecules.[136]

2.7 SURFACE FORCE MEASUREMENT TECHNIQUES

Direct measurement of surface forces is a challenging task because of their short-ranged nature. Not only is a sensitive detection technique for forces required, but also a precise control of separation on the sub-nanometer scale. Additionally, surface roughness and contaminations are usually serious issues in direct force measurement.[137]

Early attempts to measure the surface forces were indirect because what was measured was the force required to break adhesions between surfaces in contact.[138-140] One of the first direct measurements of the forces between surfaces as a function of separation was performed by Derjaguin and coworkers in 1954.[141] They tried to verify the Lifshitz' theory on the distance dependence of van der Waals forces. The force between a quartz sphere and a quartz plate for distances down to 100 nm was measured using a specially constructed microbalance with electromagnetic feedback system. The separation was measured by optical interference. Their results fell within 50% of the theoretical predictions for van der Waals forces by Lifshitz.[64] It was the first experimental result that verified the theories of molecular attraction between two solid surfaces.

Since then, more force measurement techniques have been developed and refined, and now sophisticated techniques are available. The advantages and limitations of these popular techniques, including atomic force microscope (AFM) which was used to make the force measurements presented in this thesis are discussed in the following sections.

2.7.1 *Surface Force Apparatus (SFA)*

In 1968, Tabor and Winterton[22] measured the forces between molecularly smooth muscovite mica surfaces in air using a technique later called SFA. The surface forces apparatus (SFA)[23] contains two crossed silica cylinders with a radius of curvature of about 1–2 cm onto which thin sheets of mica are glued. The separation between the two cylinders is changed using a piezoelectric translator, and the direct determination of the separation was measured by optical interferometry.

In SFA, an interferometry technique called fringes of equal chromatic order (FECO)[142] is used for determining the separation down to 0.1 nm. Among all the techniques available, it is the only one that can directly determine the true separation between surfaces. However, the FECO technique requires that both surfaces are transparent to visible light. As a result, mica has been used extensively in SFA force measurements with a few attempts to overcome this limitation by using alternative materials, including sapphire[143], silica[28], and polymer films[144]. This limited the variety of the surfaces which can be studied. Although the technique has been modified by Conner and Horn[145] so that only one surface is required to be transparent as long as the other surface is partially reflective and modified again later by Kawai et al.[146] so that the distance between two non-transparent substrates can be determined using two-beam interferometry. An alternative method has also been developed to employ opaque materials, replacing the FECO technique for measuring distances by a capacitance method[147-148, 149].

2.7.2 *Optical Trapping (OT)*

Optical trapping or optical tweezers[150] was first developed in 1986 by Ashkin et al., who demonstrated that the momentum of photons can capture and manipulate microscopic particles in three dimensions. In optical trapping, a tightly focused laser beam attracts transparent dielectric particles to its focal spot. The trapped particle can be displaced from its equilibrium position

when there are external forces. The optical trap can be used as a highly sensitive force measurement tool.[151] The trap stiffness (spring constant) can be calibrated and the displacement of the trapped particle from the equilibrium position can be measured.[152] Optical trapping has been extensively used in studying biological samples.[153] Optical trapping is also used in total internal reflection microscopy.

2.7.3 *Total Internal Reflection Microscopy (TIRM)*

Total internal reflection microscopy (TIRM), developed in 1987[154], measures the potential energy vs. separation between of a single microsphere and a transparent flat plate. In a TIRM experiment,[155] a microsphere is allowed to sediment toward the plate. When there is repulsive force between them due to, for example, electric repulsion or steric repulsion, the microsphere finds an equilibrium position. A laser beam is then directed at the particle from below through the transparent flat plate. An evanescent wave[156] is generated between the plate and the sphere, when total internal reflection of the laser beam occurs at critical angle. The evanescent wave will be scattered by the sphere. The distance between the sphere and the plate can be measured by monitoring the intensity of the scattered evanescent wave.[157] By recording the changes in vertical position of the sphere due to Brownian motion, one can determine the potential energy of interaction and the diffusion coefficient of the sphere.[158]

2.7.4 *Atomic Force Microscope (AFM)*

The atomic force microscope (AFM) was invented in 1986 by Binnig et al.[24] and it belongs to a series of scanning probe microscopes invented in the 1980s. Although, originally it was developed for imaging the topography of surfaces, it has become one of the most popular surface force measurement techniques.

In the AFM[25, 159-160] a sharp tip or a colloidal particle attached to the end of a cantilever is brought in contact with an approaching planar surface by

the use of the piezoelectric translator. The force between the probe and the surface is measured by monitoring a laser beam that is reflected from the backside of the cantilever. The radii of the probe is typically about 10 μm, the small radius results in a small contact area, reducing the impact of contamination and surface roughness.[68]

A critical part in analyzing AFM force data is the determination of zero separation, where the probe makes contact with the surface.[161] This is usually determined from the interaction forces as there is no direct measurement for absolute distance in the AFM. In contrast the FECO technique employed in the SFA offers clear information on the separation between the surfaces.

Among the surface force measurement techniques reviewed in the previous sections, the AFM appears to be the most suitable method for the experiments designed for this thesis. In the usual optical trapping setup, only transparent particles can be captured[162-163] and in the TIRM a transparent flat surface is required.[164-165] Also, TIRM is not suited to measuring strongly attractive forces. The SFA involves a relatively large contact area between surfaces, thus the technique requires a very high demand of clean handling and operation to avoid contamination.[68] Therefore, I used the AFM for surface force measurements presented in this thesis due to its relatively easy operation and flexibility in employing various types of surfaces. A more detailed description of the principles of the AFM are presented in Chapter 3 of this thesis.

CHAPTER 3

EXPERIMENTAL METHODOLOGY

This chapter describes the general experimental techniques that were used in the surface force measurements presented in chapters 4-6. Techniques that are exclusive to each chapter are described in the method section of the corresponding chapter.

The general experimental procedure in this work consisted of three main steps. Firstly, smooth hafnia surfaces were produced using atomic layer deposition (ALD). The roughness and thickness of the ALD prepared hafnia layer were then determined using an atomic force microscope (AFM) imaging and X-ray reflectivity (XRR). Zeta potentials of the surfaces were also measured to find the isoelectric point (iep). Lastly, the surface force was measured using an AFM and the force data were analysed.

3.1 ATOMIC LAYER DEPOSITION

3.1.1 *Substrates*

Atomic layer deposition (ALD) [46, 166] was used to produce smooth surfaces suitable for AFM force measurements. The AFM colloid probe technique[167] for force measurement requires one flat and one spherical surface. For the flat surface, boron-doped silicon wafers with a native oxide layer of thickness ~ 2 nm supplied by MEME, US, were used. Borosilicate spheres of monomodal size distribution and radius 10 ± 0.1 µm, supplied by Duke, (borosilicate glass 9020) were used as the spherical substrate.

Prior to ALD, the aforementioned substrates were cleaned using an in-house plasma chamber using radio frequency (RF) water plasma (30 W for 90 s, followed by 50 W for 30 s). The plasma treatment cleans organic contamination from the surface and creates hydroxyl chemical groups on the surface, which are the bonding sites for the ALD reaction.

3.1.2 *Fundamentals of Atomic Layer Deposition*

Since its development in 1977[168], atomic layer deposition (ALD) [46, 166] has become an important technique for depositing a variety of thin film materials in various applications such as thin film solar cell devices[169-171], high-k transistors[172-173], and solid oxide fuel cells[174-175]. In ALD, a sequential, self-limiting growth mechanism in the gas phase produces conformal thin films with control over the thickness and the chemical composition.[176]

ALD uses precursor vapors and reactant gases to produce layers of thin materials. Generally, ALD deposition consists of the following steps[45, 166]:

1) Reactions of first precursor with surface reactive sites
2) Inert gas purge to remove unreacted precursor or by-products
3) Reactions of co-reactant gas with surface reactive sites
4) Inert gas purge to remove unreacted precursor or by-products

These four steps are referred to as one ALD cycle which results in one layer of the material being deposited at the surface. This cycle is repeated until the desired film thickness is achieved. During steps 1 and 3, the precursor or the co-reactant gas is pulsed into a chamber under vacuum for an appropriate amount of time to facilitate the full reaction with the substrate surface. The ALD process requires an oxide surface as a starting surface to produce metal oxide film. The hydroxyl surface groups provide the surface reactive sites for the precursor. A precursor is typically a metal centre surrounded by chemical functional groups. Water vapor can be used as the co-reactant gas and nitrogen as the inert gas for purging. The surface is hydroxylated again after one full cycle, and the process is repeated. A schematic illustration of a typi

cal ALD cycle is shown in Figure 3.1.

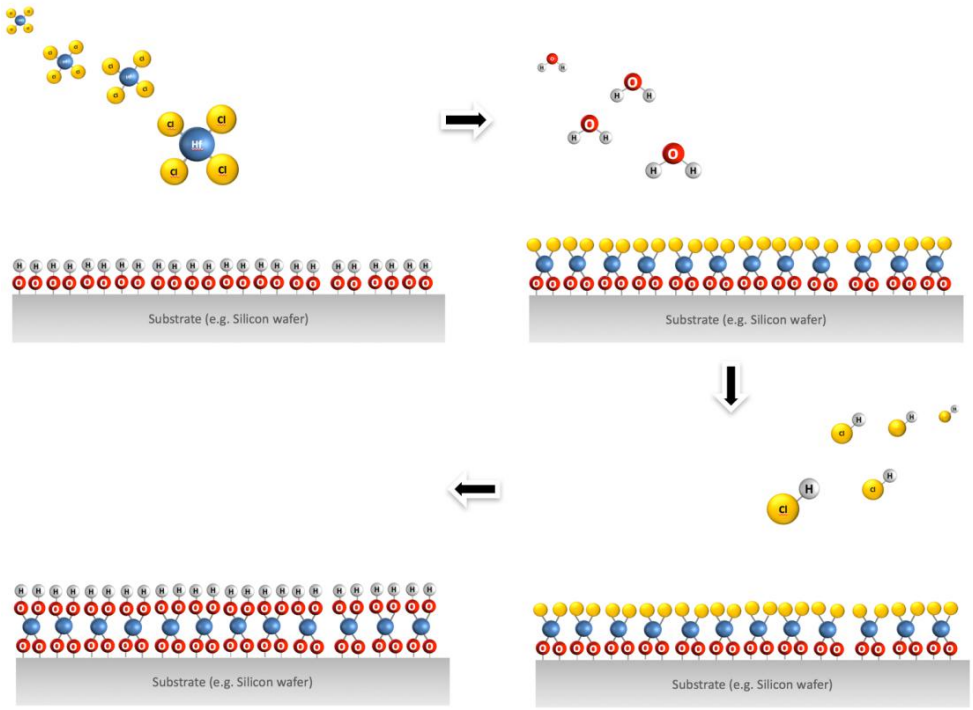

Figure 3.1: Schematic illustration of a typical ALD cycle of hafnia (HfO_2) based on a hafnium tetrachloride ($HfCl_4$) precursor and H_2O process. The cycle is based on the alternate exposure of a surface to the precursor and the co-reactant (H_2O) gas separated by purge steps.

The critical factor in choosing ALD for the work presented in this thesis over the alternative deposition techniques such as sputtering is the superior conformality of ALD-deposited films due to its self-limiting aspect. [46] Because of different precursor gas fluxes, some surface areas may react before others. However, once the reaction is reached completion in one area, the precursors will then proceed to react with other unreacted sites and produce a very conformal deposition.[46] With sufficient pulse times, the precursor can reach into deep trenches[177], and nano-pores[178], completing reaction with the entire three dimensional surface. Due to this self-limiting nature of the reaction, ALD films can be produced that are extremely smooth and pinhole-free through careful control of the deposition conditions.

3.1.3 *ALD methodology and equipment*

Smooth hafnia layers were grown on the aforementioned substrates using a Savannah 100 (Cambridge Nanotech) ALD system immediately after the plasma cleaning. It has been reported that the surface roughness of ALD produced films depend on the deposition conditions including layer thickness and reaction temperature.[43, 179]

The effects of deposition temperature and film thickness on ALD hafnia surfaces have been previously investigated.[48, 180] In the case of hafnia deposition using tetrakis (dimethylamido) hafnium as precursor, the roughness of the surface is reported to increase as the deposition temperature increases. However, when tetrakis (ethylmethylamido) hafnium was used as precursor, hafnia deposition at 175 °C led to the formation of crystallites, which led to a rougher surface, while deposition at 250 °C yielded smoother surfaces.[43] Therefore, in this work, the hafnia layer was grown at 250 °C using the tetrakis (ethylmethylamido) hafnium as precursor to minimize the roughness of the film.

In order to minimize the surface roughness, it was also necessary to limit the hafnia layer thickness to approximately 10 nm. At this layer thickness the measured dispersion forces are influenced by the substrate. Silica and silicon

typically give low dispersion forces as characterized by the Hamaker constant. To obtain a surface with a Hamaker constant similar to bulk hafnia, a titania layer was first deposited as an under-layer. At short range, the influence of the underlayers (titania and silicon) on the total interaction forces is negligible. It is the top layer that dominates the forces at short separations. As we are mostly interested in the abnormal forces observed at very short separations the relatively thin hafnia layer should be sufficient.

The titania and hafnia surfaces produced here used titanium isopropoxide and tetrakis (ethylmethylamino) hafnium as the Ti and Hf precursors, respectively, and water vapor as the co-reactant. The ALD deposition conditions for the experiments conducted in this thesis are presented in Table 3-1.

Once desired surfaces were produced using ALD, they were stored in plastic petri dishes in dry conditions until use. The surface force was measured using AFM within 6 months of the surface production. The flat surface and the colloid probe were cleaned using an RF water plasma system (at 10 W for 45 s) immediately prior to AFM force measurements.

Table 3-1: The ALD deposition condition for the hafnia layer and the titania underlayer. Nitrogen was used as the carrier gas at a flow rate of 20 sccm (standard cubic centimetre per minute).

	Precursor Temperature (°C)	ALD Reaction Temperature (°C)	Total number of cycles	Pulse duration (s)
Ti	100	80	800	Ti: 0.5 Nitrogen: 7 Water: 0.5 Nitrogen: 5
Hf	75	250	141	Hf: 0.5 Nitrogen: 20 Water: 0.5 Nitrogen: 20

3.2 ATOMIC FORCE MICROSCOPE (AFM) FORCE MEASUREMENT

3.2.1 *The principle of AFM*

A schematic of a typical AFM setup is shown in Figure 3.2. It consists of two major components. One is the piezoelectric scanner that manipulates the position of the sample in the x, y, and z directions. The other is the detection system that includes a laser source, a cantilever, a mirror, and a photodetector.[25, 161]

The cantilever tip scans the surface of the sample by the use of a piezoelectric scanner. The laser beam is aligned so that it is reflected off the back of the cantilever. In its simplest implementation, undulations in the surface cause deflection of the cantilever, which can be sensed by the reflected laser

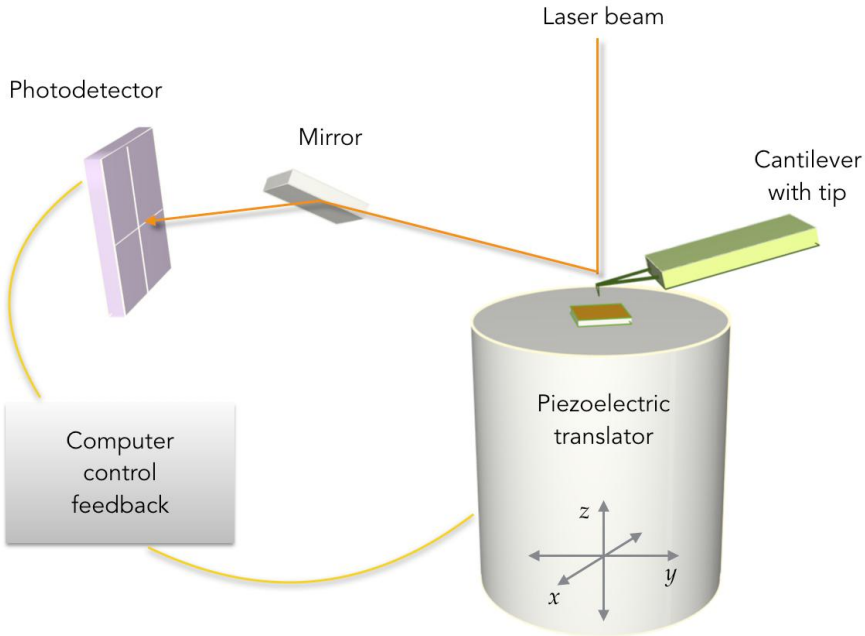

Figure 3.2: Schematic of an AFM setup. The sample is in contact with a sharp tip that sits at the end of cantilever and is scanned by a piezoelectric translator.

beam. The reflected beam is guided by a mirror onto the quadrant photodiode. The difference in the light intensities between the upper and lower parts of the photodiode is sent to the photodetector. This data is mapped in x and y to present a deflection image or alternatively the deflection data is sent to the computer control feedback loop. The feedback loop allows the cantilever defection to be held constant by maintaining a constant distance between the cantilever and the sample allowing a height image to be produced. [25, 68, 160]

3.2.1.1 *AFM imaging*

In AFM imaging modes[160], the cantilever is usually scanned over the surface to produce a topographical image of the surface. A feedback loop is employed to keep the cantilever deflection constant. This is done by adjusting the voltage applied to the scanner and hence by moving the scanner in the z -direction. From this calibrated movement of the piezoelectric scanner, the surface height profile can be generated. The surface height profiles from each single scan are then put together to generate a three-dimensional surface topography.

Several factors determine the imaging resolution. The piezoelectric scanner allows the movement of the sample possible with sub nanometre precision and the optical lever technique offers a sub-angstrom resolution in measuring the cantilever deflection.[68]

AFM imaging can employ two different AFM modes: Contact mode AFM and Tapping mode AFM.[181] In contact mode, a mechanical contact between the tip and sample is made and the deflection of the cantilever is kept constant. This mode is applicable to hard samples but is not recommended for soft samples as the forced contact damages the sample. In tapping mode, which is suitable for soft samples, the tip is oscillated near its resonance frequency. When the tip is brought close to the surface, the oscillation amplitude or the resonance frequency changes. The feedback can use either the amplitude or resonance frequency to produce a height image of the sample.

3.2.1.2 *AFM force measurement*

When AFM is used to measure the force between the probe and the sample, the piezoelectric scanner moves up and down in the direction normal to the surface.[25] This changes the distance between the probe and the sample. What is measured here is the cantilever deflection versus position of the piezo, normal to the sample surface.

In order to obtain a force-versus-separation curve, the cantilever deflection (volts) and the position of the piezo (nm) have to be converted to force and true probe-sample separation.[161] To calculate the force, firstly, the detector signal in volts is converted to cantilever deflection in nanometers, Δx, using the slope of the line of the constant compliance region measured on hard surface. The force between the probe and the sample can be found from the deflection using Hooke's law:

$$F = -k\,\Delta x \tag{3.1}$$

where k (N/m) is the spring constant of the cantilever. The calibration of the spring constant of cantilever is explained in § 3.2.2.

The true probe-sample separation x is different from the raw distance data which is the distance Z_p between sample surface and the rest position of the cantilever as illustrated in Figure 3.3. Thus, the true probe-sample separation x is:

$$x = Z_p + \Delta x \tag{3.2}$$

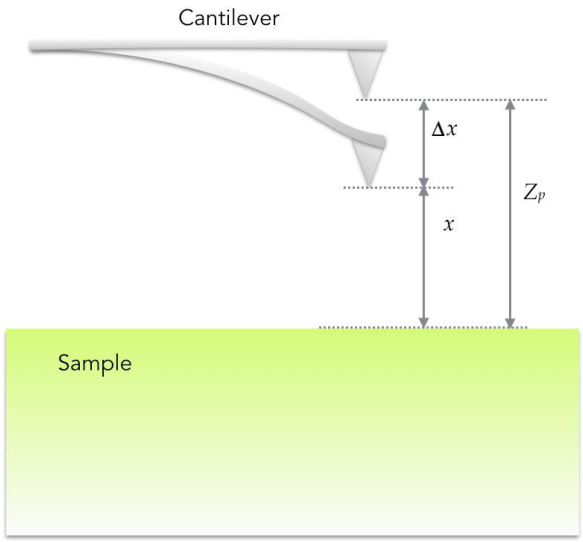

Figure 3.3: Schematic of the true probe-sample separation x

The final force versus separation curve will look similar to the force curve in Figure 3.4-b. Usually, a normalized force (the force divided by the radius of the probe F/R) is used in presenting force curve. This allows comparison between the experimentally measured force and theoretical calculation according to the Derjaguin approximation (§2.5).

As the AFM measures only the relative displacement of the cantilever not the absolute probe-sample separation, it is important to identify the point at which the AFM probe comes into contact with the sample, the so called 'zero contact point' or 'zero separation' by the method described below.[161] Usually an AFM force curve consists of several different regimes as indicated in Figure 3.4:[68]

1) At large separations, the probe and the surface do not experience any surface forces between them, and thus the cantilever deflection will be zero. The average value over an appropriately large

region is subtracted from the entire curve such that at large separations the force is zero.

2) At small separations, the probe and the surface experience surface forces between them, and the cantilever will start to deflect. When the force is attractive, the probe will jump in contact with the surface (dotted line), if the gradient of the attractive force exceeds the spring constant of the cantilever.
3) After contact, the probe and surface will move in concert for a hard surface. Here the cantilever is said to be compliant as the surface is very much stiffer than the cantilever. This is called the constant compliance region. The gradient of this compliance region is used to convert the photodiode detector signal (volts) to cantilever deflections in nanometres.
4) If the probe and the surface are both hard, then upon reversal of the direction, the cantilever will again move in concert with the sample until they separate. If adhesive forces between the probe and sample surface exist, the cantilever will bend such that the surfaces remain in contact whilst the cantilever is pulling on the probe with a restoring force. When the restoring force of the cantilever exceeds the adhesion force, the cantilever snaps back to its equilibrium position (dotted line).

At small separations, if the cantilever deflects towards the sample due to attractive forces, for example, then the probe-sample separation will be less than expected from the piezo position. This is corrected by subtracting the cantilever deflection from the piezo position. From this correction the compliance region becomes a vertical line which is then set to zero separation. A force curve of region 1) to 3) is called an "approaching" force curve as it is measured when the two surfaces are brought together and forced to make contact. It is sometimes referred to as "extension" curve because the piezo is extended during this measurement in order to reduce the separati-

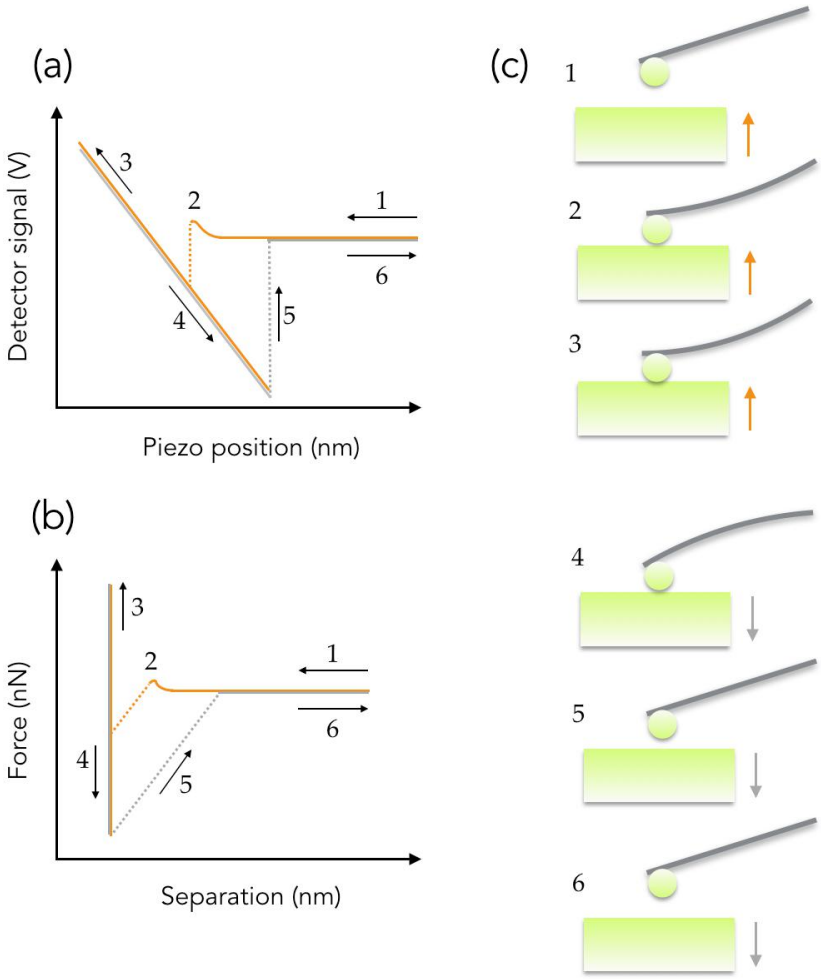

Figure 3.4: Schematic of a typical cantilever deflection (detector signal) vs piezo position curve and corresponding force vs separation plot

on between the two surfaces. On the other hand, the reversal region of 4) to 6) is called a "retraction" force curve.

3.2.2 *AFM cantilever calibration*

Accurate knowledge of the cantilever spring constant k is critical in AFM force measurement as indicated in Equation 3.1. Although cantilever manufacturers provide the values of spring constant, these values are not very reliable. Therefore, independent calibration of spring constants has to be done for each cantilever used in force measurement.

A number of methods for calibrating the spring constant are available. [182-185] We used the thermal noise method developed by Hutter and Bechhoefer[183] for spring constant calibration. This was done using the Thermal Tune of a Bruker multimode 8 AFM, in which the thermal noise method is implemented.

In the thermal noise method, the AFM cantilever is considered as a harmonic oscillator fluctuating in response to thermal noise. The total energy of such an oscillator with spring constant k and mass m, is the sum of its kinetic H_k and potential energy H_p: [25, 183]

$$H = H_k + H_p = \frac{p^2}{2m} + \frac{1}{2}k(\Delta x)^2 \tag{3.3}$$

where Δx is the displacement of the oscillator, and p is its momentum. According to the equipartition theorem, the average value of each quadratic term in Equation 3.3 is given by $\frac{k_B T}{2}$. Thus, the second term can be written as:

$$< \frac{1}{2}k(\Delta x)^2 > = \frac{k_B T}{2} \qquad \Longrightarrow \qquad k = \frac{k_B T}{<(\Delta x)^2>} \tag{3.4}$$

This implies that the spring constant k can be estimated by measuring the deflection of the freely moving cantilever in air far from the surface.

In practice, the deflection sensitivity (nm/V) is obtained from a cantilever deflection measurement on a clean hard surface. The cantilever is moved

away from the surface and the cantilever deflection is recorded for a period of time. The cantilever deflection versus time data is then Fourier transformed to obtain the power spectral density, which is a plot of Δx^2 versus frequency (kHz). The power spectral density will show a peak at the resonance frequency of the cantilever. This peak is fitted with a Lorentzian curve after subtracting background noise. The integral of the power spectrum approximately equals the total value of $< (\Delta x)^2 >$,[186] and thus, from the area under a fit to the Lorentzian curve the spring constant k can be estimated.

In this work, rectangular silicon nitride cantilevers (CSG 10 supplied by ND-MDT) were used for force measurement. Once the spring constant of the cantilever was measured by the thermal noise method, a colloid probe was attached to the tip of the cantilever. When a colloid probe is attached, the spring constant of the cantilever changes and thus a correction to the value is required. The details of colloid probe production and the spring constant correction are described in the next section.

3.2.3 *Colloid probe AFM*

The AFM force measurement performed in this work employed the colloid probe technique developed by Ducker et al.[167] and Butt [187]. In this method the force between a flat surface and a spherical surface is measured. Here, the spherical surface is prepared by attaching a 1- 10 μm sized sphere to the tip of a cantilever.

In this work, borosilicate spheres with radius 10 ± 0.1 μm that were coated with hafnia using ALD were attached to the rectangular cantilever (CSG 10 supplied by ND-MDT) whose spring constant had been determined.

The production setup consists of a microscope, a hot plate, and a three-way stage manipulator. The heat setting glue (Epikote 1004 resin, Shell) and the hafnia spheres were placed on a clean glass slide with a couple of centimeters separation. The glass slide was then placed on a hot plate to melt the glue. A cantilever was clamped on the three-way stage manipulator. The clamping was arranged so that the tip of the cantilever was facing toward the glass slide.

The attachment was done by firstly gently pressing the tip of the cantilever to a small amount of melted glue. Excess glue on the cantilever tip was removed by tapping the tip against the glass slide surface using the xyz stage. The glue on the tip is then used to pick up a hafnia sphere. The colloid probe was left to cool to room temperature before they were used for force measurement.

3.2.4 *Off-end loading correction*

The change in spring constant due to the colloid probe attachment was corrected using the off-end loading method developed by Sader and coworkers.[188] In the case of a rectangular cantilever, the spring constant of a colloid probe k is related to the end tip spring constant k_E by:

$$k = k_E \left(\frac{L}{L - \Delta L}\right)^3 \tag{3.5}$$

where L is the length of the cantilever and ΔL is the distance from the end of the cantilever to the center of the colloid probe. Note that k_E is the end tip spring constant measured using the thermal tune method as described earlier. L and ΔL were measured from an image of the colloid probe taken by SEM as described earlier. Once the spring constant of colloid probe k is estimated, it can be used in the Equation 3.1 to calculate the force.

3.2.5 *AFM force measurement between ALD prepared surfaces*

The interactions between the ALD prepared flat and the spherical hafnia surfaces were measured using a Digital Instruments Multimode Nanoscope III AFM, equipped with a low noise head.

Milli-Q water was used in the preparation of all solutions. All glassware was cleaned by soaking in 10 w/w % NaOH for 10 min and then rinsing with large amounts of Milli-Q water. In order to remove organic contaminants, NaCl was roasted at 400 °C for at least 12 h prior to use. The pH of aqueous

NaCl solutions was adjusted by the addition of either HCl or NaOH to the solution. To remove surface active contaminants,[189] NaCl solutions were bubbled with high purity nitrogen gas immediately before injection into the AFM fluid cell.

Forces were measured in 0.01 and 0.001 M NaCl solutions at a range of pH using an AFM fluid cell.

3.2.6 *AFM force data analysis*

The raw data of the cantilever deflection versus piezo movement was converted to the normalized force, F/radius (colloid probe), versus sample separation by the method described in the literature.[29] The data were then fitted using DLVO theory by solving the nonlinear Poisson-Boltzmann equation using in house software[49] in accordance with the algorithm described by Chan et al.[98]

In Chapter 4, Lifshitz theory was employed to calculate a non-retarded Hamaker constant for hafnia (hafnia-water-hafnia). We justified the use of the nonretarded Hamaker constant (See Appendix-A §A.2.1) by comparing against the distance-dependent retarded Hamaker coefficient of the multilayered structure (silicon/silica/titania/hafnia).[83] At the separations of interest, the retarded Hamaker coefficient loses less than 7% of the value of the non-retarded constant.

In Chapter 5 and 6, the retarded Hamaker coefficient was used for the hafnia surface with adsorbed citric acid (See Appendix-A §A.2.2) and the hafnia surface with a monolayer of palmitic acid (See Appendix-A §A.2.3).

3.3 SURFACE CHARACTERIZATION

3.3.1 *X-Ray Reflectivity (XRR)*

In order to calculate the van der Waals force of a multilayered structure, it is crucial to measure the thickness of the layers that compose the surface. In this thesis, X-ray reflectivity (XRR) was used to estimate the thickness of the ALD deposited films. X-ray reflectivity measurement is a powerful technique for characterizing surfaces, thin films and multilayers.[190-191] The thicknesses, density of individual layers, and surface roughness can be obtained by analyzing experimental reflectivity curves using the Fresnel formalism of optical reflection and refraction.[192]

In an X-ray reflectivity measurement, a well-collimated monochromatic beam of X-rays is directed at a surface at grazing angles (θ) as illustrated in Figure 3.5. The intensity of the reflectivity (R) is measured as a function of

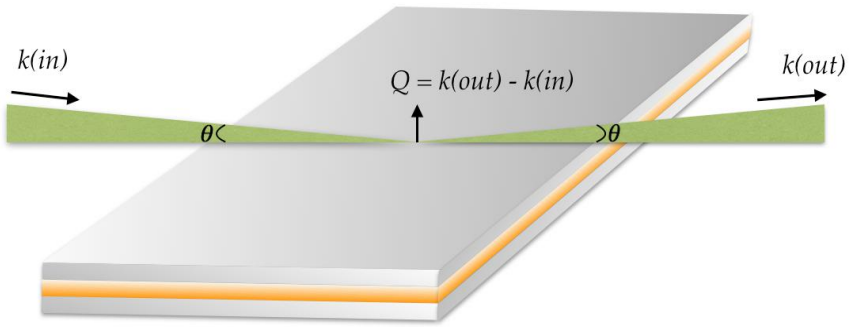

Figure 3.5: Schematic of the reflection of X-rays at from a surface with the grazing angle (θ) and the reflected angle (θ). *k(in)* and *k(out)* are the wave vector of the incoming and the outgoing X-rays, respectively. In a reflectometry experiment, the intensity of the outgoing (reflected) beam is presented as a function of the momentum change perpendicular to the surface, Q.

the angle of incident. The important variable, however, is the momentum change perpendicular to the surface, Q. It is related to the reflected angle (θ) and wavelength (λ) of the X-ray:[191]

$$Q = \frac{4\pi \sin(\theta)}{\lambda} \tag{3.6}$$

An important concept in small angle (i.e. low Q) experiment is scattering length density (SLD). It is a measure of the scattering power of a material. The SLD of a material for X-rays is:[105]

$$SLD = a_e \sum_j N_j z_j \tag{3.7}$$

where a_e is the scattering length of an electron for X-rays (a_e= 2.85 $\times 10^{-5}$ Å), N_j is the number density of each atom type, and z_j is the atomic number. As X-rays are scattered by electrons, the measured X-ray reflectivity depends on the variation in the SLD profile perpendicular to the interface.[193]

The measured reflectivity data are compared are fitted using the Fresnel formalism to determine the density profile of the surface, which can be then used to determine the thickness and SLD of each layer. Real interfaces are not perfectly sharp, therefore the data fitting also requires the inclusion of roughness of the interfaces which is usually assumed to be Gaussian[102].

Figure 3.6 shows a calculated X-ray reflectivity curve of a hafnia film deposited on a Si substrate. At grazing angles (low Q) below a critical angle, X-rays undergo total internal reflection. In other words, the incident X-rays do not penetrate into the material and the reflectivity remains at the maximum values. At high Q, where the grazing angle increases beyond the critical angle, X-ray reflectivity decreases as the X-rays penetrate into the material by refraction. Interference occurs due to the X-rays reflected from an interface within the sample, and thus the reflectivity profile shows oscillations as shown in Figure 3.6. The oscillation depends on the film thickness

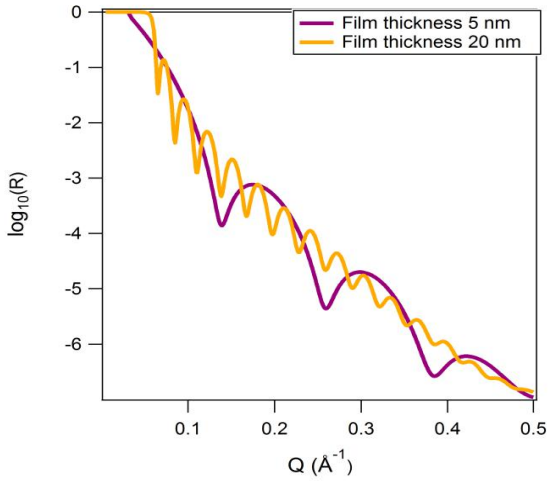

Figure 3.6: A calculated X-ray reflectivity curve showing the reflectivity as a function of the scattering vector (Q) for two Hafnia films of different thickness on a silicon substrate showing the oscillations caused by X-ray interference. The oscillation depends on the film thickness. The thicker the film, the shorter the period of the oscillations.

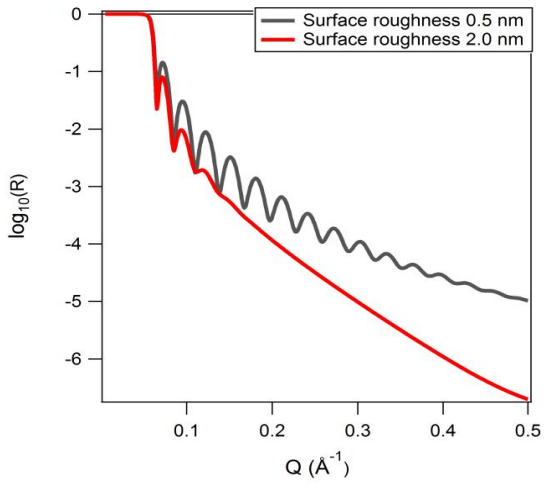

Figure 3.7: A calculated X-ray reflectivity curve showing the reflectivity of a Hafnia film on a silicon substrate with two different values of surface roughness. The X-ray reflectivity decreases more rapidly with larger surface roughness and the oscillations are less distinct. The hafnia film is modelled as 20 nm thick.

and the SLD. The period of the oscillations becomes shorter as the film thickness increases.[194]

An example of the effect of surface roughness on an X-ray reflectivity curve is shown in Figure 3.7. It indicates that when the surface roughness increases the X-ray reflectivity decreases more rapidly. Figure 3.7 also shows that the amplitude of the oscillation is less distinct with increasing surface roughness.

In this thesis, the thickness, SLD, and surface roughness of the hafnia layer and the titania sublayer were determined from the X-ray reflectivity obtained using a PANalytical X'Pert Pro diffractometer XRR and the data was analyzed using Motofit software[193].

3.3.2 *Zeta potential*

The magnitude of the electric potential at the surface of the colloidal particles, commonly known as the surface potential (ψ_0), is crucial in determining the stability of colloidal solutions. Therefore, in colloid science, it is very important to obtain an estimate of the surface potential (ψ_0) as a function of pH and electrolyte concentration.[4]

One of the most convenient methods for studying charged surfaces is zeta potential measurement. Zeta potential (ψ_ζ)[195] is the difference in electric potential between the dispersion medium and the stationary layer of fluid attached to the dispersed particle. The magnitude of zeta potential is slightly lower than that of the surface potential (ψ_0), as the plane on which the zeta potential is defined and measured is offset into solution from the surface of the charged particle (See Figure 2.1) Zeta potential is experimentally accessible and can be used as an indicator of stability of colloidal solutions as it is closely associated with the surface potential.[195] A high zeta potential indicates a highly stable colloidal system, whereas low zeta potentials are characteristics of less stable systems. At a particular pH, known as the isoelectric point (iep)[84-85], the net surface charge of the particles is zero, and the colloid system becomes very unstable leading to flocculation.

Zeta potential is often measured using the laser Doppler electrophoresis technique. In electrophoresis,[4, 196] an electric field is applied to the solution in which the charged, colloidal particles are immersed. The charged particles will move at some velocity under the influence of the applied electric field. The frequency of a laser beam changes when it is scattered by the sample particles undergoing electrophoresis. The frequency shift is related to the electromobility (μ) of a colloid[196], which is the particle velocity (u) divided by the applied electric field (E). By measuring the electromobility of a colloid, one can estimate the zeta potential (ψ_ζ) of the sample using the following equation:[4]

$$\psi_\zeta = \frac{\mu\eta}{\varepsilon_0 D} \tag{3.8}$$

Here the η is the viscosity of the medium, ε_0 is the permittivity of free space, and D is the static dielectric constant of the medium. Equation 3.8 is called the Smoluchowski equation and can be used for relatively large colloidal particles, where the particle radius is much larger than the Debye length.

In this thesis, the surface zeta potential and the isoelectric point (iep) of the ALD hafnia flat surfaces presented in Chapter 4 were determined using a Zetasizer Nano ZS (Malvern Instruments, U.K.) with the zeta potential planar cell along with zirconia particles as tracer particles[197]. In this method, the electromobility of the tracer particles is measured at varying distances from the flat surface. The magnitude of the particles mobility and the electro-osmosis generated by the planar surface can be used to calculate the zeta potential at the flat surface.[197]

The zeta potentials of hafnia powder (99.95% pure) supplied by Materion (H-1011) in the absence or in the presence of citric acid and palmitic acid were measured using a Zetasizer Nano ZS (Malvern Instruments, U.K.) with the folded capillary cell. The measurements were carried out in 0.001 M NaCl. The pH was adjusted using HCl and NaOH solutions.

3.3.3 *SEM imaging*

The radius of the colloid probe attached to the AFM cantilever was determined using a Zeiss UltraPlus analytical Field Emission Scanning Electron Microscope (FESEM)[198] at the ANU Centre for Advance Microscopy. The knowledge of the radius of the colloid probe is required as the forces are presented normalized by the radius and is important in applying the Derjaguin approximation when comparing measured forces to theory.

The average diameter of the sphere was determined from three measurements offset by ~ 60 degrees and average diameter used to determine the radius. One of the SEM images of the spheres that are attached to cantilevers used in this thesis is shown in Figure 3.8.

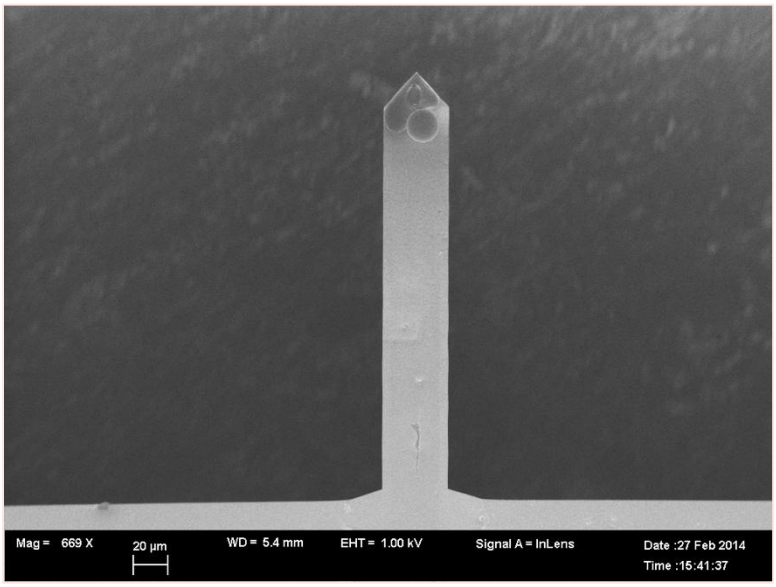

Figure 3.8: A FESEM image of a colloid attached to the tip of a rectangular cantilever using the glue (Epikote 1004 resin, Shell).

3.3.4 *AFM imaging*

The rms roughness of the hafnia surfaces was determined from an AFM image (1000 nm × 1000 nm), obtained using a Bruker multimode 8 AFM in ScanAsyst mode, using a Bruker SNL-10 or a Bruker ScanAsyst-Air cantilever. ScanAsyst mode uses PeakForce™ tapping mechanism[199] that the AFM manufacturer Bruker (CA, USA) developed. PeakForce™ mode was designed to have an oscillating system that combines the benefits of contact and tapping mode imaging: direct force control and avoidance of damaging lateral forces.

The roughness of the spherical surface was measured by employing the AFM reverse imaging technique,[200] whereby images of the colloid probe surface are obtained when it is used to image a surface consisting of sharp spikes (TGT01 from NT-MDT).

CHAPTER 4

ROUGHNESS EFFECT ON THE SURFACE FORCE BETWEEN HAFNIA SURFACES

This chapter is reproduced with minor changes and with permission from Ref. [201] *:*

Eom N, Parsons D. F., Craig V. S. J., "Roughness in Surface Force Measurements: Extension of DLVO Theory to Describe the Forces between Hafnia Surfaces", *J. Phys. Chem. B,* **2017,** *121,* 6442-6453. Copyright 2017 American Chemical Society.

4.1 INTRODUCTION

Measured interaction forces between solid surfaces often show deviations from the DLVO theory (See §2.4) at small separations. Although agreement between DLVO theory and experimental data at short range was found between mica surfaces, the theory has failed to describe the force measured between silica,[29] and zirconia[37]. A recent report by Walsh et al.[49] also revealed that the measured surface forces between the atomic layer deposition (ALD) prepared titania were repulsive at small separations at pH values remote from the isoelectric point (iep). In all three measurements, the absence of an attraction at small separations implied that an additional non-DLVO repulsive force was operating at small separations.

The additional repulsive force between silica surfaces has generally been attributed to a hydration force (See §2.6.1). Unlike silica, however, in the case of titania, hydration forces are of insufficient range to explain the experimental data.[49, 53] According to DLVO theory, the interaction at small separations should be dominated by the attractive van der Waals force, which is large due to the high dielectric constant of titania. In that sense, the interaction between titania surfaces reported by Walsh et al.[49, 53]contradicts DLVO theory.

In order to ascertain whether this unexplained phenomenon is peculiar to titania or occurs rather generally I aimed to investigate other mineral oxide surfaces. For this goal, I have chosen hafnium oxide, also known as hafnia. Hafnia has a high dielectric constant and therefore the dispersion forces should dominate at small separations, however, our preliminary work indicates this is not the case.[202]

This chapter reports the force measured between the hafnia surfaces prepared using atomic layer deposition (ALD). These surfaces are firstly characterized to determine roughness, thickness and the surface charging properties. The surface force was measured across a range of pH and at different electrolyte concentrations using atomic force microscope (AFM) and the force data were analyzed using DLVO theory incorporating new methods for accounting for the influence of roughness.[203]

4.2 RESULTS AND DISCUSSION

4.2.1 *Surface characterization*

The roughness of the ALD prepared hafnia surface was determined from AFM image over an area of 4000 nm × 4000 nm (Figure 4.1). It revealed that the roughness of the flat hafnia surface is 0.54 nm rms, which is 4% of the film thickness. The roughness of the spherical surface measured by employing the AFM reverse imaging method[200] is found to be 0.47 nm rms.

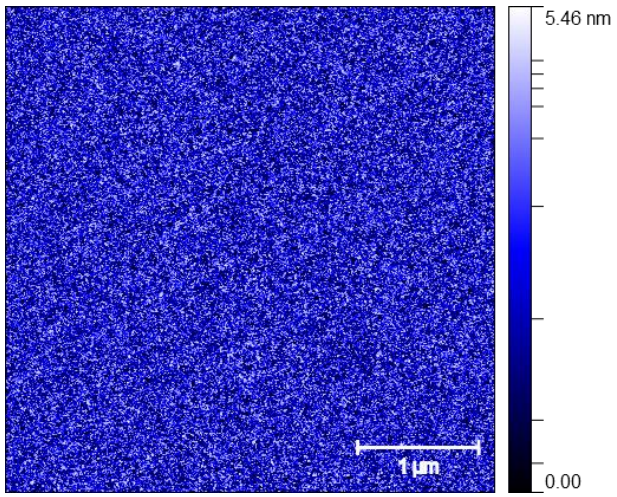

Figure 4.1: Atomic Force Microscope (AFM) image of a hafnia surface produced using atomic layer deposition (ALD). The substrate is a silicon wafer coated with a 38.0 nm thick film of titania followed by a 12.7 nm thick layer of hafnia. The rms surface roughness over an area of 4000 nm × 4000 nm was determined to be 0.54 nm rms with a peak to peak roughness of 5.46 nm.

In order for the interaction forces between the hafnia layers to be representative of bulk hafnia, the layer would ideally be > 40 nm in thickness, however depositing films this thick by ALD increases the surface roughness. On the other hand when the film is thin, the substrate influences the dispersion forces at small separations. In particular, using silicon substrates can lead to a large reduction in the magnitude of the dispersion forces. Therefore, titania was deposited as a sub-layer as described in Chapter 3. This layered film has dispersion forces similar to that of bulk hafnia with hafnia surface chemistry.

It is well known that ALD prepared surfaces can retain carbon impurities.[44, 204] The surface composition of ALD titania that was prepared under the deposition condition as the ones used in this work was previously analyzed.[53] Those X-ray photoelectron spectroscopy (XPS) results revealed that the amount of impurities such as carbon and OH^- were negligible. Due to the similarity in deposition methods we assume the influence of carbon impurity on the hafnia surfaces would be negligible as well.

The thickness of the hafnia and titania underlayer was determined to be 12.70 ± 0.05 nm and 38.0 ± 0.05 nm respectively by analysing the X-ray reflectivity versus the scattering vector (Figure 4.2). This revealed that the growth rate of the hafnia film was 0.09 nm/ cycle at 250 °C. Note that the growth rate is affected by the deposition temperature, being higher at lower temperatures.[179] A scattering length density of 5.79 ± 0.02 × 10^{-5} $Å^{-2}$ was used for hafnia.

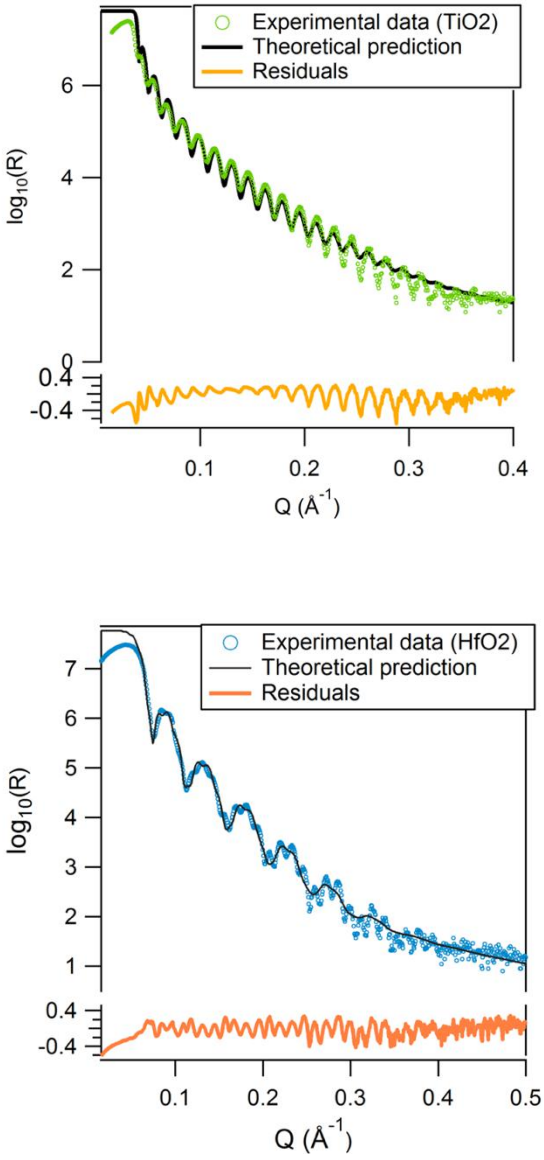

Figure 4.2: X-ray reflectivity (XRR) plot for a flat surface (Silicon wafer/titania/hafnia) equivalent to those used in the force measurements showing the log of intensity versus the scattering vector, $Q = 4\pi \sin\theta/\lambda$. Titania underlayer without the hafnia film was first analysed by XRR (top), and then using the XRR fitting parameters for titania the hafnia layer was analysed (bottom). The thickness of the titania layer and hafnia film was 38.0 ± 0.05 nm and 12.70 ± 0.05 nm, respectively. The data were fitted using a roughness of 0.72 ± 0.01 nm and a scattering length density of 5.79 ± 0.02 × 10^{-5} Å^{-2} for the hafnia and a scattering length density of 2.87 ± 0.03 × 10^{-5} Å^{-2} for the titania underlayer.

The density of the ALD hafnia was determined to be 8.76 g/cm^3 which is 91 % of that of bulk hafnia[205]. The rms roughness of the hafnia surface was determined to be 0.72 nm from the X-ray reflectivity analysis, which is higher than the roughness obtained from AFM imaging. This can be explained by underestimation of the roughness obtained by AFM due to convolution of the image with the finite tip radius of the cantilevers used.[206]

The charging behavior of the ALD hafnia surface as a function of pH can be determined from the zeta potential. The zeta potential was determined on a flat hafnia surface, as shown in Figure 4.3, by measurement of the surface zeta potential. The hafnia surface was positively charged at pH lower than 4.1 and negatively charged at pH greater than 5.2. Thus the isoelectric point (iep) was found to be approximately at pH 4.5. The iep of hafnia particles supplied by Materion (H-1011) was also investigated and found to be at pH 5.1, in agreement with the ALD hafnia surface.

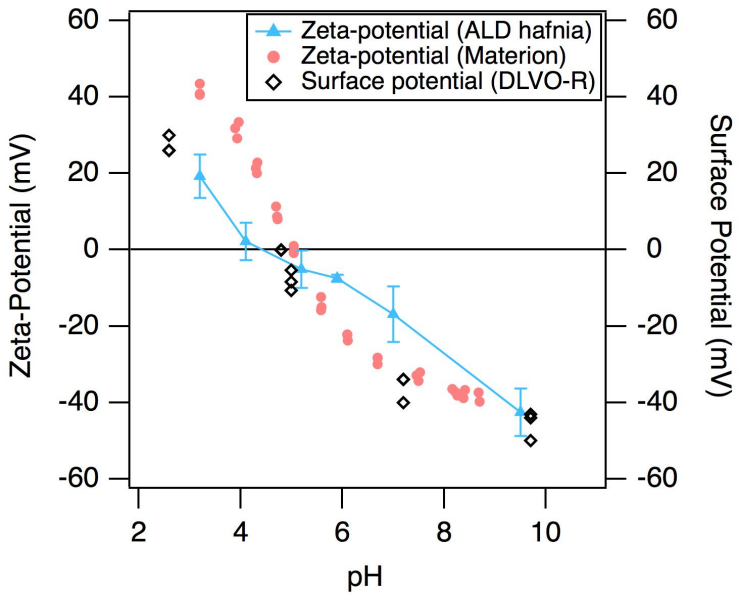

Figure 4.3: Zeta potential as a function of pH in 0.001 M NaCl for a flat ALD hafnia surface and for hafnia particles supplied by Materion (H-1011) compared to the surface potential determined by analysing the surface force measured between ALD hafnia

The surface potential determined by analysing the surface force measurements, which is reported in a coming section (§4.2.5), is also shown in Figure 4.3 for comparison. It indicates that the isoelectric point occurs at approximately pH 5. The magnitude of the zeta potential is less than the actual surface potential as the zeta potential is measured at the slip plane.

4.2.2 *Surface force measurement between ALD hafnia surfaces*

Surface forces between ALD hafnia surfaces were measured in 0.001 M and 0.01 M of NaCl solution using an atomic force microscope (AFM) and are shown in Figure 4.4 and Figure 4.5, respectively. Measured forces are strongly pH dependent. At pH 9.7, the force is repulsive both during approach and upon separation. The magnitude of the repulsive force decreases slightly when the pH is reduced to 7.2. As the pH is further decreased to 5.0 and 4.8, the force becomes attractive. However, when the pH is reduced to 2.6, the force becomes repulsive again. This strong pH dependency of the force curve is attributed to the pH dependency of the surface potential. The isoelectric point (iep) of hafnia was determined to be approximately pH 5 by zeta potential measurement in the previous section. At the iep of hafnia, the surfaces are neutrally charged and hence the electric double-layer force is minimized leaving the attractive van der Waals force as the dominant force. At pH 4.8 and pH 5.0 which are close to the iep, attractive forces are observed.

At pH remote from the iep, significant surface potentials are expected to give rise to the electric double-layer repulsive force. This explains the repulsive force measured at pH 9.7, 7.2, and 2.6. The zeta potential results also showed that the surface potential is more negative at pH 9.7 than pH 7.2. This is evident in the measured force, in that the force is more repulsive at pH 9.7 than at pH 7.2. The same trend of the force dependency on the solution pH observed in 0.001M of NaCl is seen in 0.01 M of NaCl (Figure 4.5). What is significant in all these measurements is that at pH values remote from the iep, the dispersion forces do not dominate the electric repulsive double layer force at small separations as expected within the DLVO paradigm.

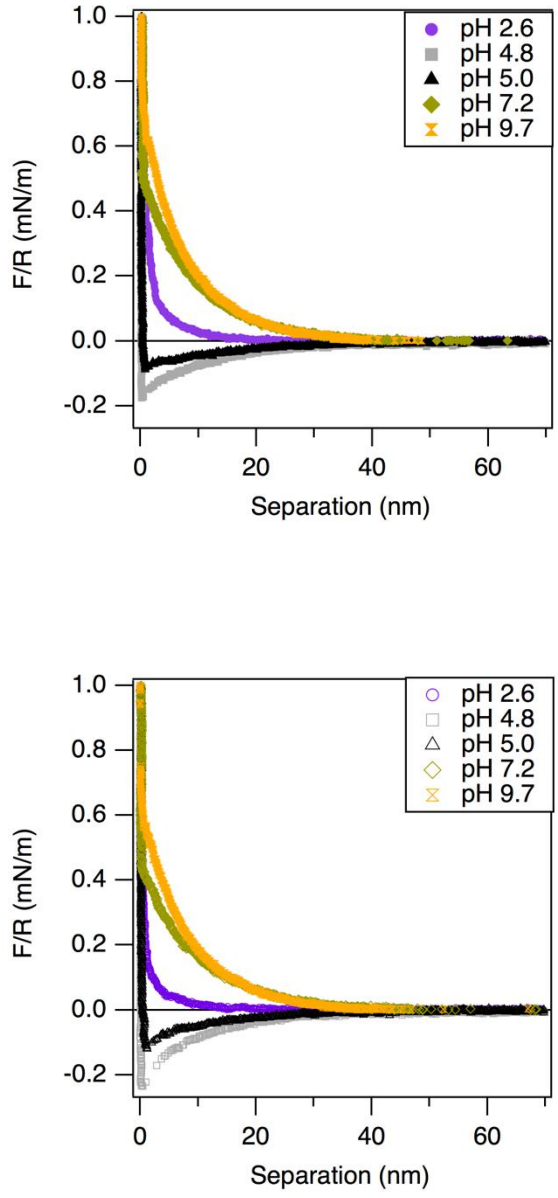

Figure 4.4: Surface force normalised by probe radius versus separation distance on approach (top) and retraction (bottom) between ALD hafnia surfaces in the presence of 0.001 M NaCl in a range of pH.

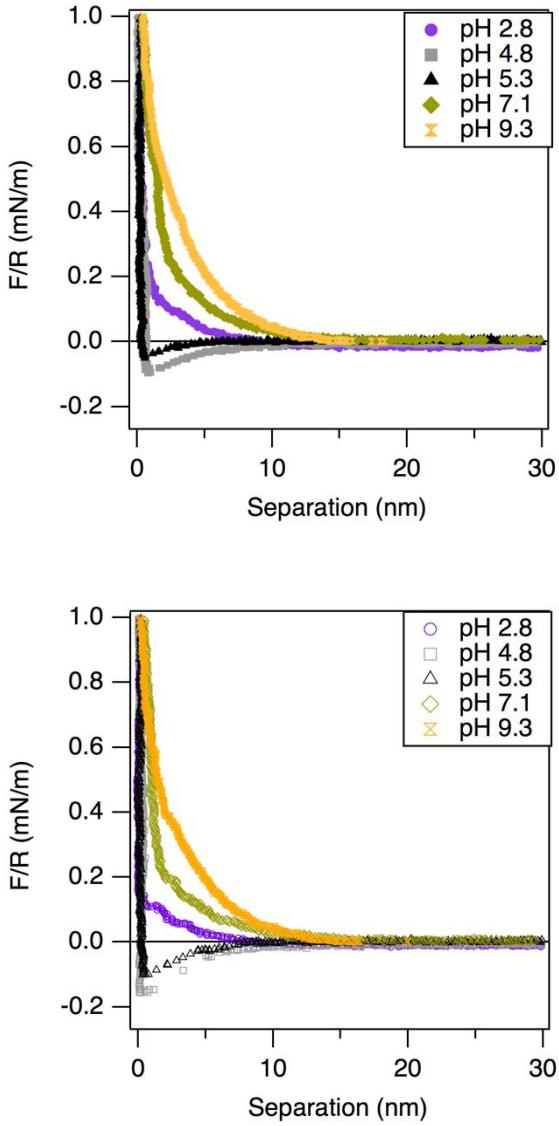

Figure 4.5: Normalized surface force versus separation distance on approach (top) and retraction (bottom) between ALD hafnia surfaces in the presence of 0.01 M NaCl in a range of pH.

4.2.3 *DLVO fitting*

When the solution pH is adjusted close to the isoelectric point (iep), the electric repulsion between the surfaces is minimized, revealing an attractive force (see Figure 4.6). The nature of this attractive force is analyzed and discussed in the later section (§4.2.7). Here it is presented merely to highlight the presence of a strong attraction around the iep, in order to highlight its absence at pH values remote from the iep.

The measured force in 0.01 M and 0.001 M NaCl at approximately pH 7 which is higher than the iep, is shown in Figure 4.7. The interaction agrees with the DLVO theory at larger separations but this is not the case at small separations, as the interaction remains repulsive up until contact. This does not agree with the DLVO theory, which predicts that at small separations, the attractive van der Waals force overcomes the electric repulsion. Interaction forces of a similar nature have previously been seen between silica surfaces.[28-29] In both cases it appears as though the short-range van der Waals attraction is absent. For silica it was argued that the attractive van der Waals force is overcome by short-range repulsive forces due to surface hydration.[29] However, the same argument cannot be applied to hafnia, as the van der Waals attraction is approximately 8 times larger between hafnia surfaces and therefore the dispersion force should be evident at separations far beyond the range of the hydration force which has a decay length of approximately 0.3 nm. The same monotonically repulsive force has been reported between titania surfaces[49, 53, 202-203]. Hence, the measured forces differ from DLVO theory in that the dispersion forces do not dominate the electric repulsion at small separations, at pH values remote from the iep in a number of systems.

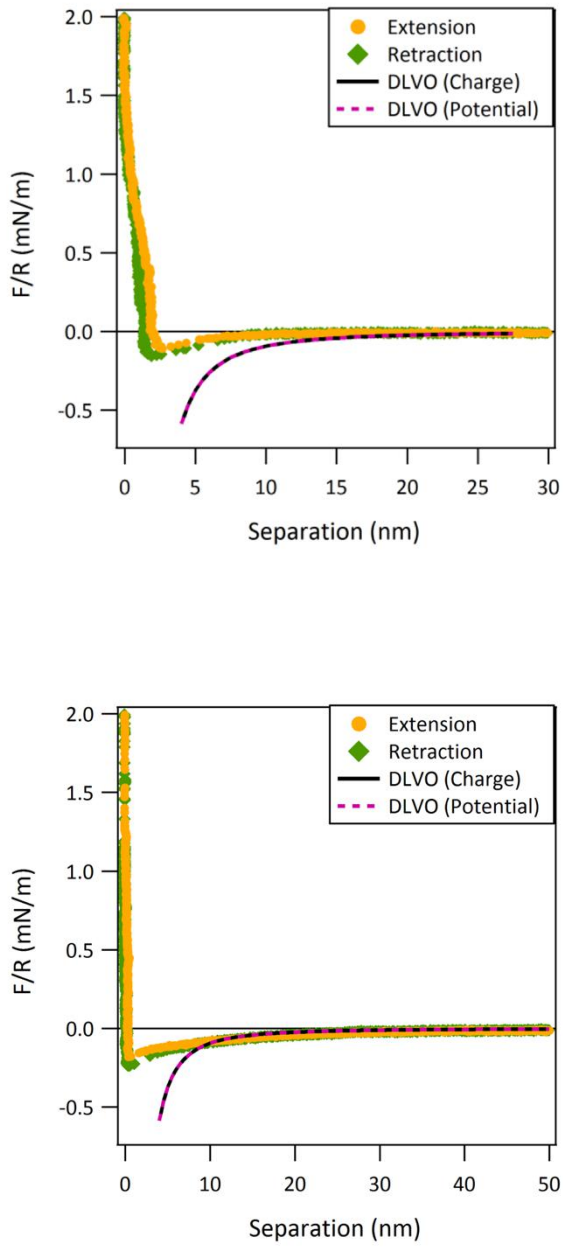

Figure 4.6: The measured force at pH 4.8 in the presence of 0.01M (top) and 0.001 M NaCl (bottom) compared to the calculated dispersion forces using a Hamaker constant of 56 zJ. The measured forces were significantly less attractive than the calculated dispersion force at separations smaller than 10 nm.

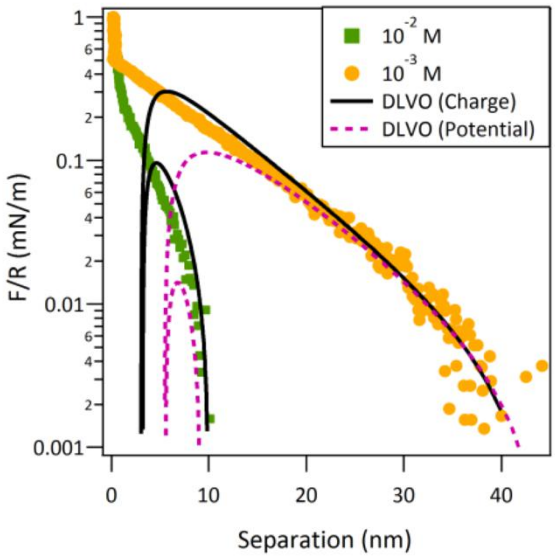

Figure 4.7: Normalised surface forces measured between ALD prepared hafnia surfaces in the presence of 0.01 M and 0.001 M NaCl at pH ~ 7. Only the approach data are shown, as the retraction force curves were identical. The data were fitted using conventional DLVO theory by solving the nonlinear Poisson-Boltzmann equation using in house software in accordance with the algorithm described by Chan et al.[98] A non-retarded Hamaker constant 56 zJ was used. The two theoretical fits represent the boundary conditions of constant charge (solid line) and constant potential (dotted line). The fitting parameters were as follows. 0.01 M: Debye length 3.3 nm, surface potential -27.7 mV; 0.001M: Debye length 9.1 nm, surface potential -30.1 mV.

4.2.4 *DLVO fitting, including the hydration force*

The absence of a short-range attraction in measurements between hydrophilic silica surfaces has been justified as being due to the presence of an exponentially decaying repulsive hydration force that dominates the van der Waals attraction at short range.[71] The ALD hafnia surfaces used here were water plasma cleaned immediately before force measurements were made. The contact angle decreased to less than 10° following this cleaning procedure. As the surfaces were very hydrophilic, we would also expect a hydration force to be present. Therefore, the DLVO theory was extended to include a hydration force. The fitting using DLVO theory extended by including hydration repulsion is shown in Figure 4.8. An exponentially decaying hydration force[115] with amplitude of 20 N/m and decay length 0.3 nm was used as shown in Equation 4.1.

$$\frac{F}{R} = \left(20 \cdot e^{-x/0.3\,nm}\right) \text{ N/m} \tag{4.1}$$

The extended DLVO interaction for the attractive force measured at pH 4.8 becomes less attractive when the hydration force is added. However, the addition of the hydration force is insufficient to bring the calculated theoretical force into agreement with the experimental data at separations between 3~8 nm. In order to achieve reasonable fits the hydration prefactor had to be increased to values greater than 1000 N/m (See Appendix-D). This is far greater than expected for any known hydration force. We also note that the possibility that the hydration force could be enhanced between water plasma treated surfaces has been ruled out as the same non-DLVO repulsive force was seen between argon plasma treated surfaces.[53]

It is evident that in all cases the forces measured were more repulsive than the calculated DLVO interaction at small separations, even after the hydration force is included. DLVO theory treats the surfaces as perfectly smooth, when in practice our surfaces have a small amount of roughness.

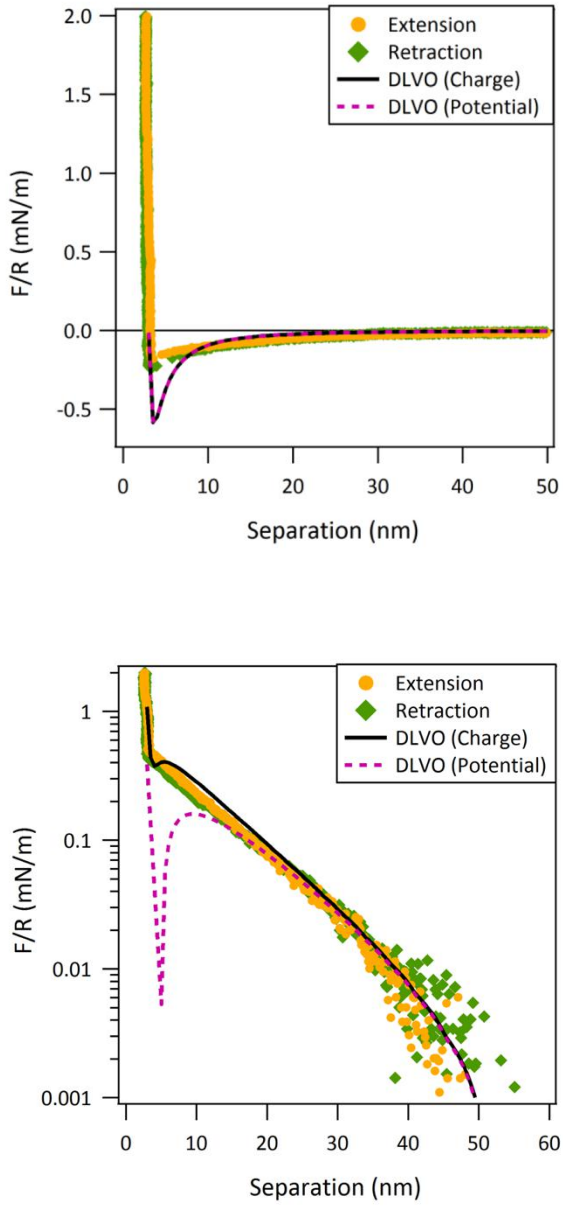

Figure 4.8: Normalised surface forces measured on approach between ALD prepared hafnia surfaces in the presence of 0.001 M NaCl. The Hydration force with amplitude of 20 N/m was added to the DLVO fitting for the forces measured at pH 4.8 (top) and at pH 7.2 (bottom) in the presence of 0.001 M NaCl. Both data were fitted with Hamaker constant of 56 zJ and the parameters were as follows. pH 4.8: Debye length 9.6 nm, zero surface potential, pH 7.2: Debye length 9.4 nm, surface potential -33.0 mV.

Therefore, I have investigated whether the disagreement between the experimental data and the theory can be attributed to the non-zero surface roughness of our ALD hafnia surfaces. A method of incorporating surface roughness into theories of surface forces that takes into account the rough-end noncontact force and the elastic contact of asperities has been developed.[203] This model was used to fit our surface force data on hafnia. This is presented in the next section.

4.2.5 *DLVO fitting, including the influence of surface roughness*

The effect of surface roughness on the DLVO forces has been investigated in several theoretical and experimental studies.[207] One approach is to redefine the surface plane as the point where asperities make contact, reducing the values of an apparent Hamaker constant and surface potential to match.[208] A more natural model can be obtained by taking the surface position to be the average position of surface heights, with asperity contact added as an explicit repulsive contribution to the total force. The surface separation is hence defined as the distance between the average height of two interacting surfaces. The DLVO theory with roughness (DLVO-R)[203] that we have employed consists of two chief elements. Firstly, using the probability distribution of surface heights, the noncontact (DLVO type) surface force is averaged over all the surface elements between all the statistically possible surface separations. Roughness can be included in the model in two different ways, either by incorporation of a histogram of the heights of the surface features or by assuming a Gaussian roughness distribution with the magnitude described by the rms roughness. The latter is employed here.

The DLVO-R theory was used to fit the same experimental data presented in the previous sections. This is shown in Figure 4.9 (0.01M NaCl) and Figure 4.10 (0.001M NaCl). The presence of asperities on the surface leads to a shift in the surface contact outwards, so that the surfaces remain separated relative to the average positions of the interfaces, even at the highest contact forces employed. This is because after the highest asperities make contact

they only deform a little under the loads applied in a typical AFM experiment. The magnitude of this effect increases as the surface roughness increases.

The first column in Figure 4.9 shows the experimental force data measured in 0.01 M NaCl at a range of pH fitted with extended DLVO-R theory with rms roughness of 0.54 nm (flat surface) and 0.47 nm (spherical surface). These roughness values were obtained from AFM images. All the data were fitted with a hydration force with amplitude of 20 N/m and decay length 0.3 nm, a surface stiffness described by a Young's Modulus of 57 GPa for hafnia,[209] and asperity tip curvature R = 4 nm. It is noteworthy that although it is not taken into account here, the hydration force would be attenuated by the surface roughness as the structure of water ordering is disrupted by roughness.[203] The effect of including roughness in the extended DLVO theory at all pH is to make the interaction more repulsive at small separations. At pH values remote from the iep, that is, at pH 2.8, pH 7.1, and pH 9.3, the extended DLVO-R theory fits the data reasonably well at all separations. The decrease in the repulsion at separations of 3~8 nm that was still evident when only the hydration force was added to the DLVO theory has been smoothed out here. This effect of surface roughness agrees with the result previously reported on the force between mica and electrochemically roughened gold surfaces measured by Surface Forces Apparatus (SFA).[210] At pH values close to the iep, that is, at pH 4.8 and pH 5.3, the extended DLVO-R theory is also less attractive at small separations and therefore fits the data better, but the agreement is limited.

As mentioned in the previous section, X-Ray Reflectivity measurements reported an rms roughness value greater than that obtained by AFM of 0.72 nm. This roughness value was also used to fit the same data and is shown in the middle column of Figure 4.9 and Figure 4.10. It is evident that this higher roughness value fits the data better, especially for the attractive force measured around the iep. As mentioned earlier, the roughness (0.54 nm and 0.47 nm) measured by AFM is underestimated due to the finite tip radius of the cantilever used in the AFM imaging. Whilst using the XRR roughness value improves the agreement between DLVO-R and the experimental data the fit

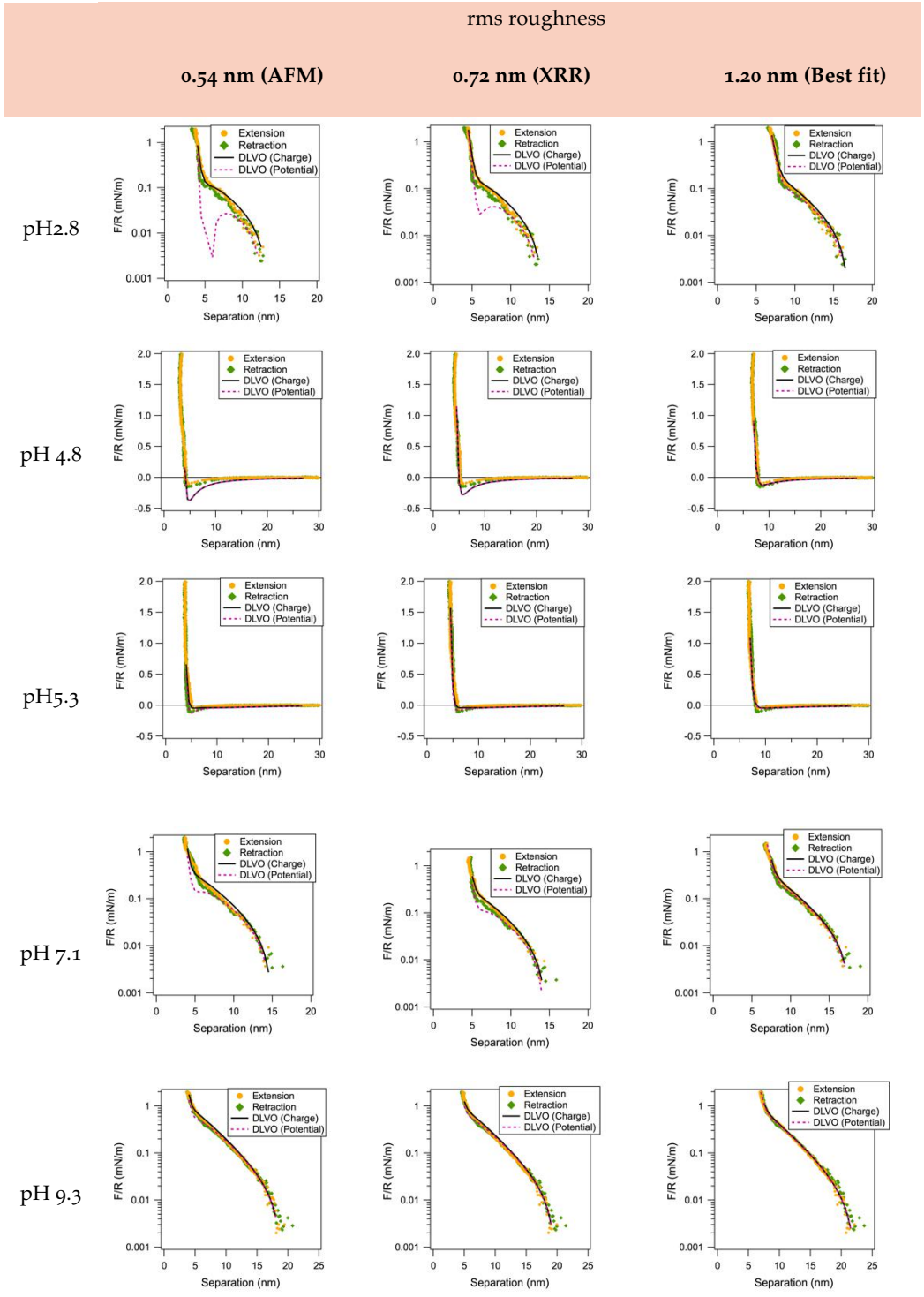

Figure 4.9: The DLVO theory extended to include hydration and roughness fitted against experimental force data between two hafnia surfaces in 0.01 M NaCl at a range of pH. Three roughness values of 0.54 nm and 0.47 nm (left), 0.72 nm (middle), and 1.2 nm (right) for the flat surface were used. All the data were fitted with a hydration force with amplitude of 20 N/m and decay length of 0.3 nm, Young's Modulus of 57 GPa, and asperity tip curvature R = 4 nm. See Appendix-B for enlarged figures.

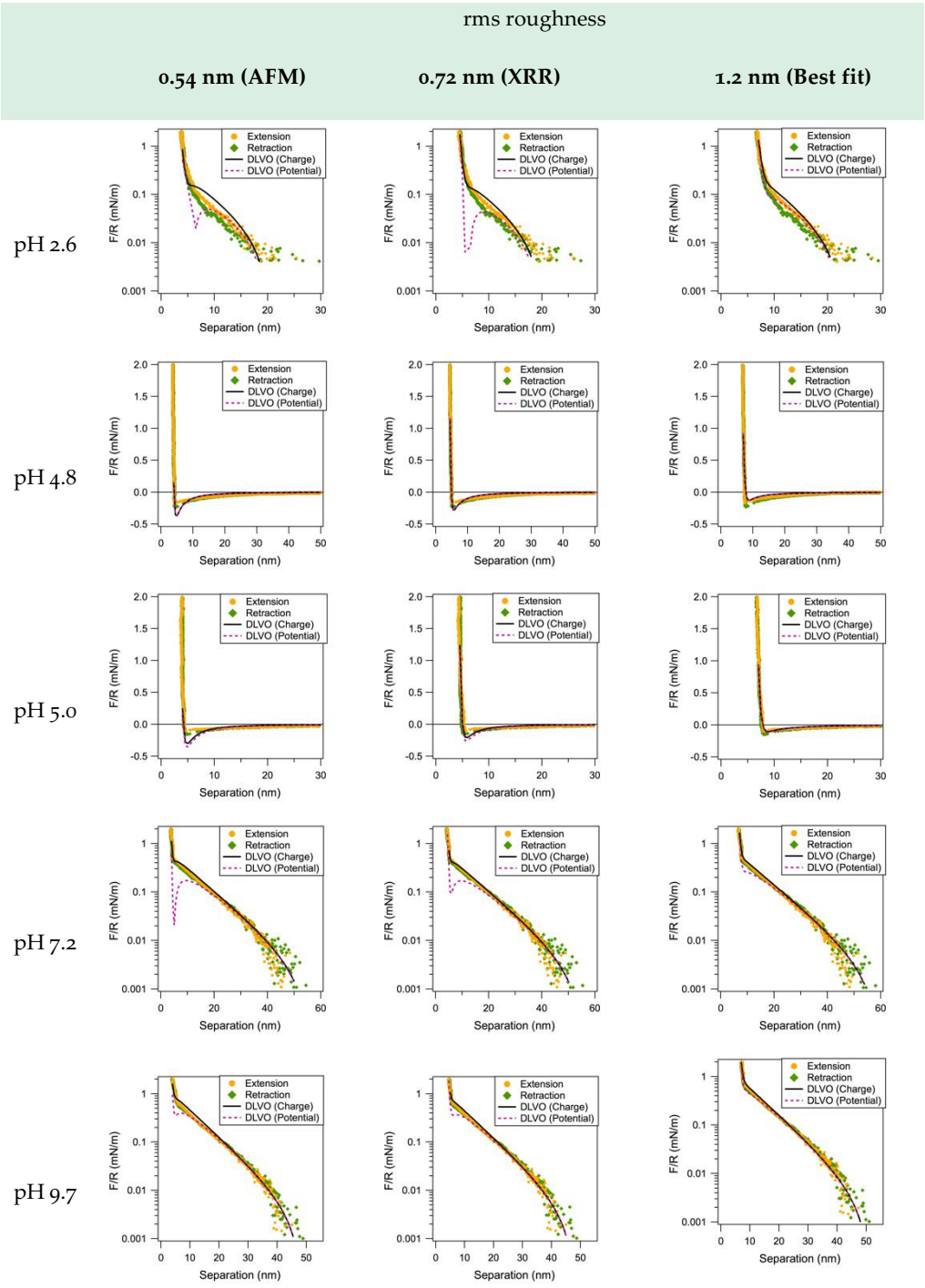

Figure 4.10: The DLVO theory extended to include hydration and roughness fitted against experimental force data between two hafnia surfaces in 0.001 M NaCl at a range of pH. Three roughness values of 0.54 nm and 0.47 nm(left), 0.72 nm (middle), and 1.2 nm (right) for the flat surface were used. All the data were fitted with a hydration force with amplitude of 20 N/m and decay length of 0.3 nm, Young's Modulus of 57 GPa, and asperity tip curvature R = 4 nm. See Appendix-B for enlarged figures.

Table 4-1: Fitting parameters used in the force curve fitting using DLVO-R. Surface potential and Debye length used for three different surface roughness are shown.

NaCl Concentration (M)	pH	Surface roughness (nm)	Surface potential (mV)	Debye Length (nm)
0.01	2.8	0.54	+ 27.0	4.0
		0.72	+ 28.0	
		1.20	+ 33.0	
	4.8	0.54	0	3.0
		0.72	0	
		1.20	0	
	5.3	0.54	- 23.2	3.0
		0.72	- 23.2	
		1.20	- 22.1	
	7.1	0.54	- 33.0	3.7
		0.72	- 32.0	
		1.20	- 41.0	
	9.3	0.54	- 46.0	3.7
		0.72	- 50.0	
		1.20	- 62.0	
0.001	2.6	0.54	+ 26.0	5.2
		0.72	+ 26.0	
		1.20	+ 30.0	
	4.8	0.54	0	9.6
		0.72	0	
		1.20	0	
	5.0	0.54	- 10.7	9.6
		0.72	- 8.38	
		1.20	- 5.33	
	7.2	0.54	- 34.0	9.6
		0.72	- 34.0	
		1.20	- 40.0	
	9.7	0.54	- 44.0	8.0
		0.72	- 43.0	
		1.20	- 50.0	

is not ideal around the iep. We therefore investigated if a higher value for the rms surface roughness could give an improved fit to the data.

Using a roughness value of 1.20 nm, both the constant charge and constant potential DLVO-R theory fit the data very well at all pH values investigated both in 0.01 M NaCl and 0.001 M NaCl as shown in the third column of Figure 4.9 and Figure 4.10. It is notable that all the data measured in this study can be fit with this one single value of surface roughness. The roughness value used in the theory is greater than that measured experimentally, this is most likely due to the surface features not following a Gaussian distribution. In that case, a histogram of the surface roughness could be used in the DLVO-R theory instead of rms roughness. This approach incorporates more information on the roughness and therefore promises to be more accurate.

The fitting parameters including surface potential and Debye length for all the force curves presented in Figure 4.9 and Figure 4.10 are shown in Table 4-1. The Debye length was set at a fixed value for three different values of the surface roughness in the extended DLVO-R theory whilst the surface potential was adjusted to find the best fit. It was found that for the repulsive force data the surface potential was determined to be higher when greater roughness was used. Figure 4.11 shows the difference between the surface potential from the extended DLVO-R theory and that from extended DLVO theory. This result shows that the extended DLVO theory without considering surface roughness generally leads to an underestimation of the surface potential.

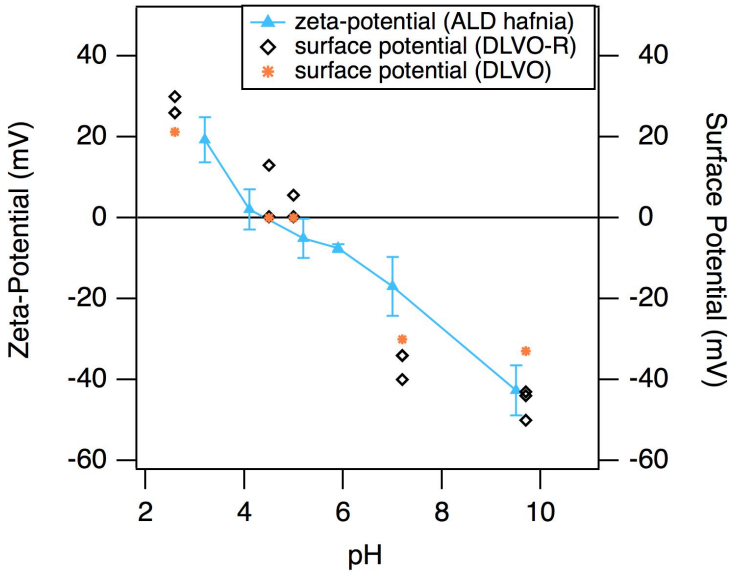

Figure 4.11: Experimentally measured zeta-potential, surface potential determined from DLVO theory, and surface potential determined from DLVO-R theory (with three different surface roughness) in 0.001 M NaCl.

4.2.6 *The effect of surface roughness on the surface forces*

To date, the agreement between the experimental result and the DLVO theory at short separations has been found only between mica surfaces. The double layer repulsive force measured between silica,[28-29] gold,[211] zirconia,[37] and titania[49] showed that the force was not overtaken by the van der Waals attraction at small separations. The force measured between smooth hafnia surfaces in this study also showed no van der Waals attraction predicted by the conventional DLVO theory. However, we demonstrated that the force curves were well described by the DLVO-R theory. The effect of surface roughness successfully explained the unexpected forces observed in the measured data at small separations, which both the DLVO theory and the

theoretical calculation of forces between asymmetrically charged surfaces failed to predict.

The force data at pH values far from the iep at first glance appears to be just an electric repulsion without any van der Waals attraction. Therefore, one might hypothesize that the van der Waals force is either absent or diminished. To counter such an argument, we have direct evidence for the presence of a significant van der Waals force at larger separations. In order to confirm the magnitude of the dispersion force, one of our repulsive force data sets was fitted with zero Hamaker constant as shown in Figure 4.12. This study shows that the disagreement between experimental measures of surface forces and the DLVO theory seen between a range of surfaces[27-28, 37, 49, 211-212] are due to roughness even for very smooth surfaces. We have shown that surface roughness fundamentally changes the nature of the interaction at pH values remote from the iep. The effect of roughness is to reduce or remove the primary minimum in the interaction forces between particles as the influence of roughness suppresses the influence of the dispersion forces at pH values remote from the iep due to repulsive forces arising from asperity contact.

4.2.7 *Analysis of the attractive forces between surfaces at pH near the iep*

If the repulsive force observed had been purely electric the curve should have been a straight line on this log-linear plot. However, the repulsive force is reduced due to the influence of the dispersion forces, described by a Hamaker constant of 56 zJ. This verifies that the measured attractive forces also contain the van der Waals force component.

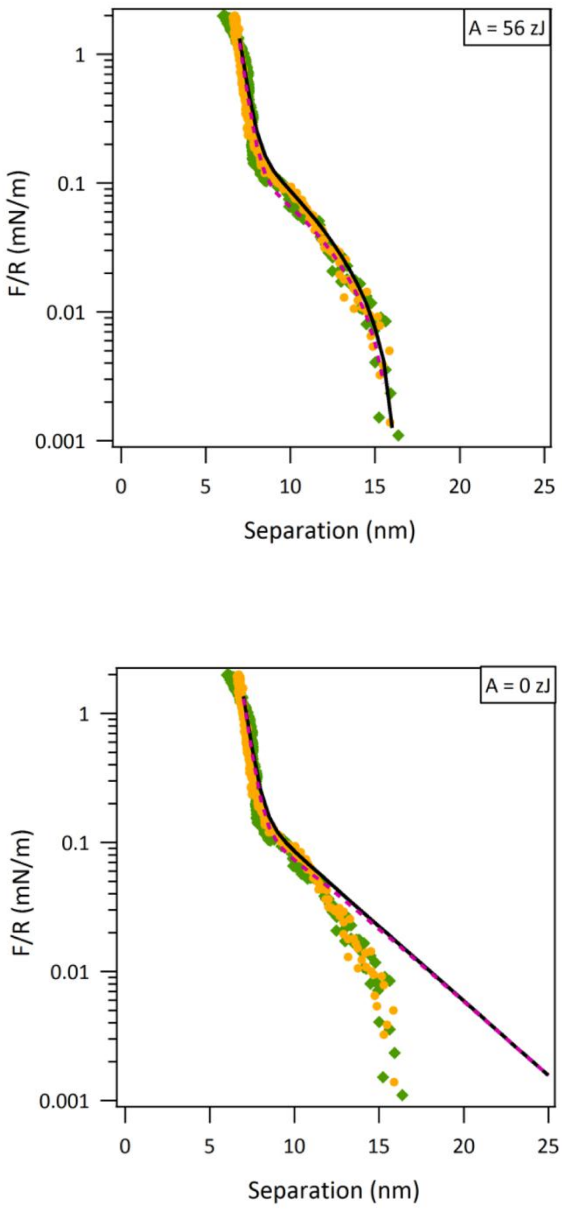

Figure 4.12: Repulsive force measured at pH 2.8 in the presence of 0.01 M NaCl compared to the roughened DLVO theory (rms roughness 1.2 nm) with Hamaker constant of 56 zJ (top) and zero dispersion force (bottom).

Interestingly, the attractive forces measured around the iep were found to depend on the electrolyte concentration as shown in Figure 4.13. The range of the force increased as the electrolyte concentration decreased, suggesting that an electric interaction is also present.

DLVO theory predicts that pure van der Waals force is largely independent of the electrolyte concentration and the force curve is approximately described with a power law. The theoretical van der Waals curve is shown as a solid line in Figure 4.13. The Hamaker constant for the van der Waals forces (non-retarded Casimir-Lifshitz force) of the hafnia surfaces investigated in this study was calculated to be 56 zJ taking into account the thickness of the titania underlayer (See Appendix-A §A.2). A Non-retarded Hamaker constant was used for simplicity in the calculation. Note that the difference between the non-retarded and retarded Hamaker constant at small separations is small for the hafnia surfaces employed in this study (See Appendix-A §A.2.1). For example, at separation of 20 nm the retarded Hamaker constant is 54 zJ differing from the non-retarded one by 3.7 %. As the pH is close to

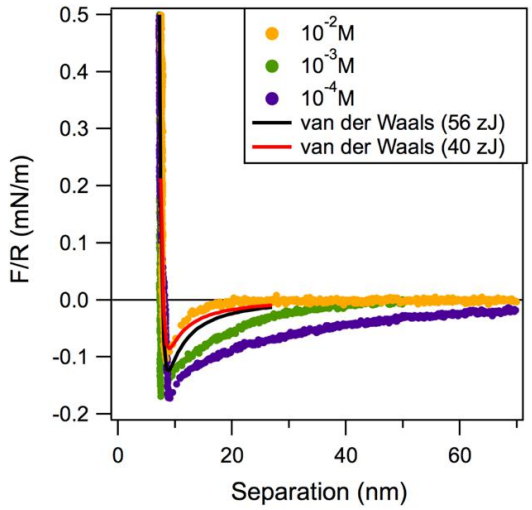

Figure 4.13: Attractive force measured at around pH 5 in 0.01M, 0.001M, and 0.0001 M of NaCl. The range of the attractive force was dependent on the concentration of the electrolyte solution, indicating an electric component in the interaction. The pure van der Waals force curve with Hamaker constant of 56 zJ is shown (black solid line). The Hamaker constant was reduced to 40 zJ to fit the force curve obtained in the 0.01M NaCl (red solid line).

the iep the data were fitted using a surface potential of 0 mV. Therefore, the DLVO calculation becomes just an expression of the van der Waals forces.

It is possible that our ALD hafnia surface has a smaller Hamaker constant than the calculated value of 56 zJ because its mass density that was estimated from the X-Ray Reflectivity (XRR) data is 9 % less than that of bulk hafnia. If this is the case, then it should reduce the van der Waals force by the same amount. However, in order to fit the attractive force data obtained in 0.01 M NaCl the Hamaker constant had to be decreased to 40 zJ, which is a 29 % reduction from the theoretical value of 56 zJ. Also, it was not possible to fit all the attractive forces measured in different electrolyte concentrations with a single Hamaker constant, even if the surface potential was varied. In addition, the attractive forces measured in this study were better described by an exponential function than a power function.

4.2.7.1 *Attractive electric force*

As there is evidence that there is an electric component to the attraction we consider the possibility that the surfaces have oppositely signed charges. This may arise near the iep if surface charge densities are slightly different for the two surfaces. This would lead to an exponentially decaying electric attractive force that would depend on the salt concentration. The attractive double layer forces between oppositely charged surfaces have been directly measured previously [213-215].

Parsegian and Gingell[94] calculated the pressure between two parallel planar surfaces that are asymmetrically charged. When the surface potentials are assumed fixed, the electric pressure is written as

$$P_{\psi}(x) = \frac{4e^2 n}{k_B T} \frac{-(\psi_1{}^2+\psi_2{}^2)+\psi_1\psi_2(e^{\kappa x}+e^{-\kappa x})}{(e^{\kappa x}-e^{-\kappa x})^2} \qquad (4.2)$$

where ψ_1 and ψ_2 are the surface potentials of the two surfaces, e is the elementary charge, n is the ionic strength of the electrolyte, k_B is the Boltzmann

constant, T is the temperature, and κ is the inverse of the Debye length. Equation 4.2 was integrated to obtain the interaction energy between two planar surfaces, and then the Derjaguin approximation[104] was applied to calculate the force between a spherical and a flat surface (Figure 4.13). The constant potential expression of Equation 4.2 is used here to illustrate the point of an asymmetric electric contribution at the isoelectric point. A more detailed analysis of the low concentration behaviour at the iep would invoke asymmetric constant charge (or charge regulated) conditions.

The attractive forces measured in 0.001 M and 0.0001 M NaCl were fitted using the van der Waals attraction with the addition of the electric double layer attraction between surfaces of opposite charge but the same magnitude in Figure 4.14. Figure 4.14-a shows the fitting without taking into account the roughness effect. The potentials of the two surfaces were varied so that they were equal in magnitude but opposite signs. All the data were fitted with Hamaker constant of 56 zJ, additional hydration force with amplitude of 20 N/m and decay length of 0.3 nm, and Young's Modulus of 57 GPa. The theoretical force curve seems to explain the electrolyte concentration dependence of the measured force curves. The theory agrees with the measured forces in that the range of the attractive force increases as the electrolyte concentration decreases. Also, it explains the attractive forces measured in 0.001M and 0.0001M, which were larger than the pure van der Waals attraction.

Although, at small separations the theory of electric double layer force between asymmetrically charged surfaces predicts much stronger attraction than the measured forces. When the effect of surface roughness was taken into account, however, the fit improved significantly as shown in Figure 4.14-b. The roughness effect seems to explain the unexpectedly smaller electric double layer attraction at small separations.

The surfaces are produced in the same manner so it would be surprising to find that the surface charge varies by the magnitude required. An alternative explanation is that the charges are not distributed evenly across the surface. However theoretical models for such "patchy charge" interactions suggest that the decay length for such interactions should be half of the usual Debye length[216] and this does not accord with our observations. Furthermore

any net charge diminishes this effect[217] ruling out the possibility that a combination of these effects is operating. The nature of this attractive force is further discussed in Chapter 6 (§ 6.3.6).

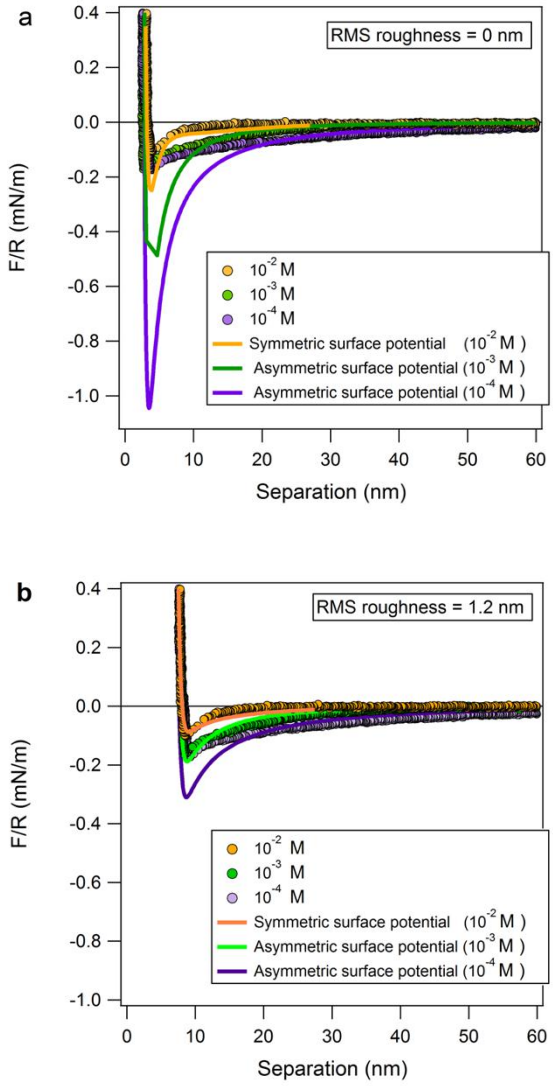

Figure 4.14: Attractive force measured at around pH 5 in 0.01M, 0.001M, and 0.0001 M of NaCl. The measured data were fitted using the van der Waals attraction with the addition of the electric double layer attraction with(b) and without(a) taking into account the roughness effect. All the data were fitted with a Hamaker constant of 56 zJ, additional hydration force with amplitude of 20 N/m and decay length of 0.3 nm, and Young's Modulus of 57 GPa. rms roughness of 1.2 nm with asperity tip curvature R = 4 nm was used for the calculation of the roughness effect in (b). Asymmetric surface potential and Debye length for each NaCl concentration were as follows (for both a and b). 0.001M: Surface potential 1 = + 10.2 mV, Surface potential 2 = - 10.2 mV, Debye length = 9.5 nm. 0.0001M: Surface potential 1 = + 14.5 mV, Surface potential 2 = - 14.5 mV, Debye length = 30.0 nm. Measured data in 0.01 M NaCl was fitted using the van der Waals attraction with electric double layer repulsion with surface potential of +22.9 mV (zero roughness), and +14.0 mV (1.2 nm rms).

4.3 SUMMARY

The interaction forces between hafnia surfaces has been measured at a range of pH and salt concentrations. DLVO theory predicts strong primary minima that are not observed in experiments. However, the data is well described, using DLVO-R theory where the effect of the surface roughness is taken into account, using a reasonable value for the rms roughness of 1.2 nm to describe all the experimental data. Notably even surfaces that are extremely smooth with a minute level of surface roughness exhibit interaction forces that are fundamentally different at small separations when roughness is taken into account.

Importantly this study has demonstrated that roughness needs to be considered and accounted for in all measurements of surface forces with the exception of molecularly smooth surfaces such as mica. The difference is significant as applying DLVO theory infers a very strong primary adhesion at pH values remote from the iep, when in fact no adhesion is observed. Thus application of the DLVO theory to real surfaces can lead to false conclusions on the stability of colloidal dispersions. The observation that near the iep attraction is observed in DLVO-R theory indicates that flocculation of dispersions is likely to be more effective by adjusting the pH to the iep than a moderate increase in electrolyte concentration at pH values remote from the iep.

CHAPTER 5

EFFECT OF CITRIC ACID ON THE SURFACE FORCES BETWEEN HAFNIA SURFACES

The work presented in this chapter was done in collaboration with Shuhei Shinohara of the Institute for Materials Chemistry and Engineering at the Kyushu University of Japan. The optical reflectometry and the atomic force microscope force measurements were carried out by him. My role was to train him to do these measurements and analyse and interpret the data.

5.1 INTRODUCTION

Stabilization of colloidal particulate systems is required in many industrial products and manufacturing technologies.[218-220] Electric stabilization[221-222] and steric stabilization[74, 223] are the two traditional mechanisms for colloidal stability. Adding molecules that adsorb to a surface is often an efficient way of controlling the stability and rheology of colloidal dispersions and nanoparticles. Surface adsorbing molecules will change how particles interact not just by altering the electric charge on the surface, but also by adopting different conformations at the solid-solution interface.[224] The impact of the configuration of adsorbed molecules on the inter-particle interaction between colloid particles is widely recognized.[224-226] For example,

at low molecular weight, polyacrylic acid (PAA) gives rise to a steric repulsive interaction whereas at high molecular weight, an attractive mechanism is observed due to bridging.[227-228]

Low molecular weight (LMW) carboxylic acids are commonly used as particle interaction modifiers as they adsorb readily to metal oxide-aqueous and metal-aqueous interfaces. LMW carboxylic acids can be categorized by the number of carboxylate groups. This categorization is convenient as the affinity for surfaces also follows the number of carboxylate groups, such that generally the adsorption follows the trend, monocarboxylate < dicarboxylate < tricarboxylate.

One of the tricarboxylic acids, citric acid ($C_6H_8O_7$), which occurs naturally in citrus fruits[229], has been routinely investigated as a potential stabilizer for both minerals processing and ceramics production[226, 230-239]. Citric acid is often used in the production of gold and silver nanoparticles where it can perform the roles of reducing agent, size controller and steric stabilizer[240-241]. The citrate ion also plays a significant role in biology and the environment. Citrate controls the crystal habit and is responsible for stabilizing apatite nanocrystallites in bone.[242] The citrate anion occurs naturally in blood and has been used as an anticoagulant to stabilize blood and blood products for over 100 years.[243] Citrate ions are also present in soil[244-245] and in the rhizosphere[244-246] at significant concentrations. Furthermore, in fundamental studies, citrate can be used as a simple model for humic and fulvic acids which are important natural chelating agents that influence the stability and dissolution of colloids and nanoparticles and thereby influence the transport and breakdown of inorganic materials in the environment.[247-248] Importantly adsorption of citric, fulvic and humic acids changes the pH range over which particles are stabilized by shifting the isoelectric point to low pH values. Thus particles that may be unstable at near neutral pH values may be stabilized by adsorption of citric, humic and fulvic acids.

The influence on the surface properties of the adsorption of citric acid to titanium nanoparticles and the implications for the bioavailability and transport of nanoparticles has been investigated by Mudunkotuwa and Grassian.[239] In their study, the interaction forces were not directly measured

but modeled between spherical, perfectly smooth, particles using a modified DLVO theory. Leong [136], Biggs and co-workers[249] have experimentally measured the influence of citrate on surface forces via atomic force microscopy (AFM) between zirconia surfaces. They reported an additional repulsive force at close separation (~ 2 nm) and high pH (pH > 7) but this was not apparent under acidic conditions. At all pHs studied, they measured a consistent "step" when the surfaces were brought into contact. Although Biggs and co-workers conceded that surface roughness may have obscured their measured force interactions especially at close separations, they surmised that the consistent "step" must be due to the presence of a steric layer on the zirconia surfaces due to the absorbed citrate. They concluded that adsorbed citrate provided an electrosteric barrier between the zirconia surfaces leading to a much reduced maximum yield stress as measured in the aforementioned rheology study.[136]

Smoothness of the interacting surfaces is a central issue in studying forces on a nanoscopic scale, as surface roughness can cloud the interpretation of surface forces, especially if the surface roughness is of the same order as the surface forces. Ultra-smooth silica surfaces are often employed in AFM surface force studies[250], but as silica is negatively charged even at low pH, citrate does not adsorb in significant amounts to silica. A smooth well-characterized stable surface with an isoelectric point sufficiently high to promote citrate adsorption is required. The hafnium oxide (hafnia) surfaces[201] produced by atomic layer deposition (ALD) that I investigated in chapter 4 are a good model substrate, because hafnia has an isoelectric point at ~pH 5, and the surfaces have very low roughness and have been extensively characterized[43, 251].

In this chapter, I aim to elucidate how adsorbed citrate influences particle interactions by directly measuring the surface forces using the colloid probe AFM technique[167, 187]. In analyzing the surface forces, the effect of the surface roughness[203] was taken into account. From the surface forces the stability of the particles in solution as well as the type of particles formed upon flocculation can be inferred. This is important in understanding the transport of nanoparticles and colloidal materials in the environment[239]. The general

features observed for the hafnia-citrate system are expected to be followed by a wide range of mineral oxide surfaces with isoelectric points at near-neutral pH[84] such as titania (iep ~6), zirconia (iep ~5-8), magnetite (iep ~5-8), and haematite (iep ~5-9).

5.2 EXPERIMENTAL METHODS

5.2.1 *Optical Reflectometry*

Optical reflectometry (OR) was utilized to measure the amount of citric acid adsorbed onto the hafnia surface over a range of pH values, following the method of Dijt et al[252] using a custom built optical reflectometry (OR).[253-254] A schematic of the optical reflectometer used is presented in Figure 5.1. In

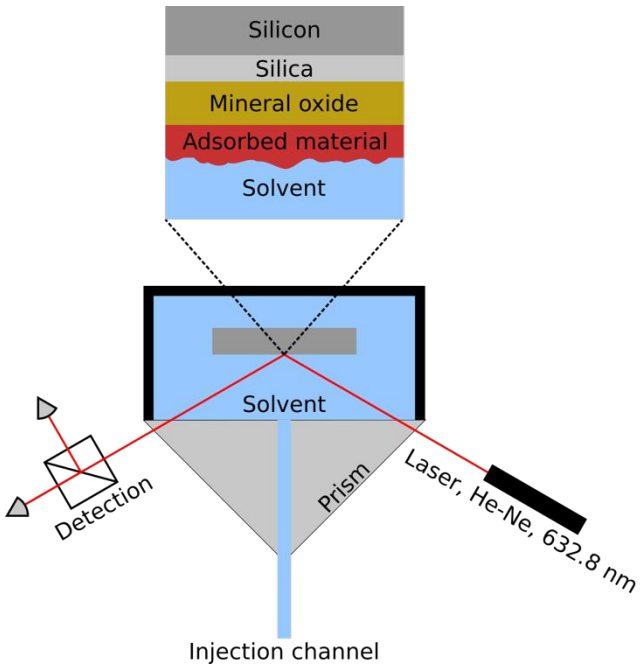

Figure 5.1: Schematic of an optical reflectometer. A polarized HaNe laser is reflected from the surface of interest and the p and s components of the reflected light are measured by a detector. When material is adsorbed on the surface, the intensity of the reflected p and s components changes. Using Equation 5.1, this change in the signal can be converted to adsorbed surface excess.

the optical reflectometry (OR), a polarized HeNe laser is reflected from the hafnia surface that is immersed in solvent in a fluid cell and the p and s components of the reflected light are measured by a detector. A stable baseline is recorded when the sample cell contains only solvent (in this case 0.001 M NaCl). Then the citric acid solutions are introduced into the cell. When citric acid is adsorbed to the hafnia surface, the intensity of the *p* and the *s* polarized reflected light changes. The measured change in the ratio of the p and s polarization is related to the surface excess according to: [252]

$$\Gamma = \frac{\Delta S}{S_0 A_s} \tag{5.1}$$

where Γ is the adsorbed surface excess, S_0 is the baseline ratio of the reflectivities of the p and s components, i.e. $S_0 = R_p/R_s$ (usually ~ 1), ΔS is the change in polarization and A_s is the sensitivity parameter obtained from the optical model. Note that the OR measures the amount of adsorbed material at the surface and is insensitive to the conformation of material at the interface.[252] The customized OR was constructed to maximize temperature stability, minimize electronic noise and optimize data acquisition rates.[253-254] An example of typical OR data showing adsorption and desorption of citric acid to hafnia is shown in Figure 5.2 .

In order to calculate the surface excess from optical properties of the surface, a sensitivity parameter, A_s, was used to convert changes in the polarization of reflected light to a measure of surface excess as indicated in Equation 5.1. The sensitivity parameter was determined as -0.041 m^2mg^{-1}, by using the matrix method of Abeles[255] applied to a five-layered Fresnel model of the surface. We took the refractive index value of water, silica, silicon and hafnia as 1.333, 1.46, 3.87 and 2.11, respectively for a 632.8 nm HeNe laser used for the measurement. The incident angle of light was fixed at 71 degrees. The refractive index increment (*dn/dc)* value of citric acid in the presence 10^{-3} M NaCl was measured to be 0.118 $cm^3\ g^{-1}$ using an Optilab rEX (Wyatt technology). The water and silicon layer were treated as semi-infinite and the thickness of the SiO_2 and hafnia layer were 107 nm and 12.7 nm, respectively.

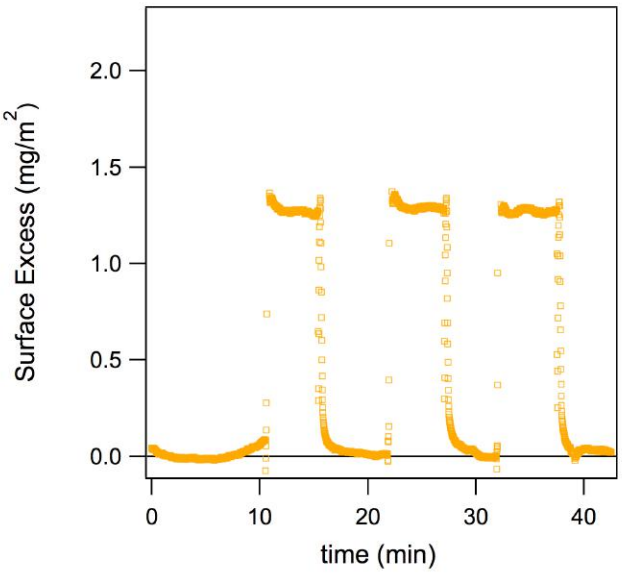

Figure 5.2: An example of typical OR data showing adsorption and desorption of citric acid to hafnia surface. 10^{-1} M of citric acid solution is injected into the cell after recording the baseline using 10^{-3} M of NaCl for 10 min. The equilibrium surface excess is obtained before rinsing the cell with the solvent (10^{-3} M of NaCl) at approximately 17 min. The cycle is repeated to obtain the average value of the surface excess. (Data captured by S. Shinohara)

Note that the silicon substrate used for optical reflectometry (OR) measurement was terminated with a 107 nm thick oxide layer to increase the sensitivity of OR measurements. The temperature of the instrument and solutions were kept at 23 ± 0.1 ℃.

5.2.2 *Solution preparation*

All glassware was cleaned with 10 wt% NaOH for 10 minutes and rinsed with purified water. NaCl was purified by heating at 400 ℃ for 8 hours. Citric acid was purchased from Sigma-Aldrich and used without further purification. All solutions were prepared using MilliQ water. For all the experiments, the solutions were stored in the same room as the instrument for more than

a day prior to the measurement, to ensure that the temperature of the solutions was the same as the instrument.

5.3 RESULTS AND DISCUSSION

5.3.1 *Surface potential*

As an approximate measure of the surface potential the zeta-potential of the hafnium oxide surface with and without citric acid in 0.001 M NaCl solution is presented in Figure 5.3. The isoelectric point (iep) of the hafnia surface was found to be around pH 5. Note that this zeta potential for the hafnia particles supplied by Materion (H-1011) is generally in agreement with the surface potential reported in Chapter 4 for the ALD hafnia surfaces (See Figure 4.3).

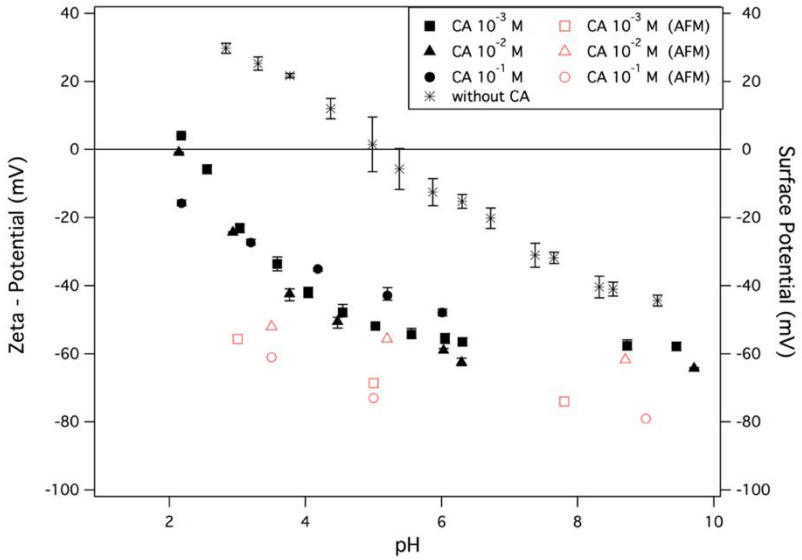

Figure 5.3: Zeta-potential as a function of pH for hafnia particles in 10^{-3} M NaCl solution and in the presence of 10^{-3} M, 10^{-2} M, and 10^{-1} M citric acid in 10^{-3} M NaCl solution. The surface potentials (open symbols) estimated from the AFM force measurements are also presented for comparison. The magnitude of the surface potential is slightly greater than the zeta potential as expected, due to the reduction in potential between the surface and the slipping plane.

When citric acid at concentrations of 10^{-1} M, 10^{-2} M, or 10^{-3}M was added to the hafnia suspension, the iep was shifted to pH 2. This shift of iep to a lower pH implies that the citric acid adsorbed onto the hafnia surface. It is well known that the degree of deprotonation of citric acid (pK_{a1}=3.13, pK_{a2}=4.76, pK_{a3}=6.39) depends on the pH of the solution. The relative fraction of citric acid species in solution as a function of pH is shown in Figure 5.4. At the iep of hafnia (pH 5), the dominating species of citric acid in solution is the singly deprotonated HX^{2-}. These anions adsorb to the hafnia surface because even though the overall surface charge is neutral, there are still positive sites for the anions to bind to. The zeta potential of hafnia changed from 0 mV to approximately -50 mV when citric acid was added at this pH. It is important to note that surface speciation of carboxylic acids differs from that in the bulk[256] and deprotonation of the adsorbed citrate ion is greater than the solution pK_a's indicate.[239]

Below the iep when the hafnia surface is positively charged, citric acid exists mainly in the form of H_2X^- and H_3X in bulk solution. The H_2X^- species

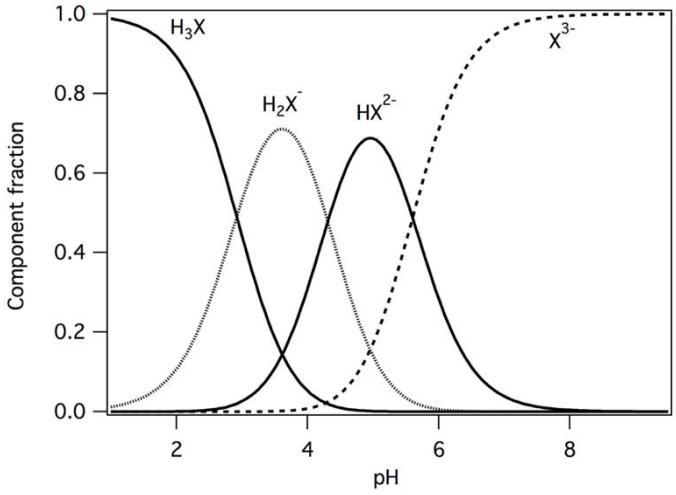

Figure 5.4: Relative fraction of citric acid species, where citrate is represented as X, calculated using dissociation constants: K1= 8.1 × 10^{-4}, K2= 1.77 × 10^{-5}, K3= 3.9 × 10^{-7} which correspond to pK_{a1}=3.09, pK_{a2}=4.75, pK_{a3}=6.41.

is electrically attracted to the hafnia surface. At around pH 3, the zeta potential was approximately +30 mV without citric acid. However, adsorption of citrate led to charge reversal and dropped the surface potential to -30 mV when citric acid was added. Above the iep, the hafnia surface is negatively charged which limits the adsorption of the dominating X_3^- species due to electric repulsion. The zeta potential change was relatively small at this high pH (8 ~ 9). It changed from around -40 mV to -60 mV when the citric acid was added. This implies that citric acid adsorption to the hafnia surface is comparatively small at high pH. A similar trend was observed by Hidber and coworkers.[238] They found that the iep of alumina shifts to lower pH with increasing amount of citric acid. The surface potential determined from the AFM force measurements (discussed in §5.3.4) is presented as open symbols in Figure 5.3 for comparison. The zeta potentials are lower than the surface potentials, as the measurement position of the former is not at the hafnia surface but at the shear plane and is therefore reduced by ions in the Stern layer and electric screening. The zeta potential highlights an important property of citric acid adsorption, which confers stability on colloids in natural waters. Adsorption of citric acids shifts the isoelectric point to low pH values that are not commonly accessed in the biosphere. Therefore, at near neutral pH the colloids with adsorbed citric acid have a significant negative charge, which leads to electric stabilization of nanoparticles and colloidal particles, preventing flocculation and aiding transportation by flow and diffusion.

5.3.2 *Adsorption of citric acid*

The amount of citric acid adsorbed per unit area of hafnia surface as a function of pH measured using Optical Reflectometry (OR) is shown in Figure 5.5. In each case, upon rinsing, the surface excess returned to the baseline, this indicates that the citric acid adsorption to hafnia surfaces is reversible on the timescale of these measurements. The observed general trend is that the adsorbed amount increases with decreasing pH, this is consistent with the charging of the surface and the citrate molecule. Above the iep (pH 5) the negatively charged hafnia surface repels the negatively charged citrate ions.

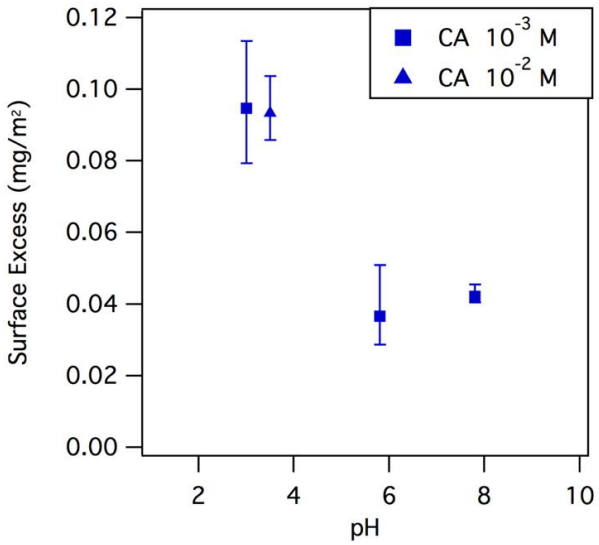

Figure 5.5: The surface excess of citric acid on hafnia surface over a range of pH in 10^{-3} M NaCl solution measured using optical reflectometry (OR). The Sensitivity parameter calculated using the dn/dc value of citric acid in NaCl 10^{-3}M solution was -0.041 m^2 mg^{-1}. The concentrations of citric acid were 10^{-2} and 10^{-3} M. The measurement of the surface excess for 10^{-1} M citric acid was not reproducible as at high concentrations mixing processes interfere with the performance of the OR instrument.

This results in a decreased surface excess of approximately 0.04 mg/m^2 at pH 6 and pH 8 at a citric acid concentration of 10^{-3} M. The presence of some adsorption at high pH agrees with the previous observations that addition of citric acid shifts the zeta potential of hafnia to more negative values even at high pH (Figure 5.3). The surface excess is greater at pH 3 and pH 3.5, (~ 0.09 mg m^{-2}). As this is below the iep the hafnia surface is positively charged which favors the adsorption of negatively charged citrate ions. This increased level of adsorption, results in a change in sign of the zeta potential of hafnia from positive to negative and a shift in the iep to lower pH.

5.3.3 *Forces between surfaces in the presence of citric acid*

The zeta potentials of hafnia surfaces between pH 3 and pH 9 in the presence of citric acid range from -30 mV to -60 mV (see Figure 5.3) indicating that a significant double layer repulsion should be evident between hafnia surfaces with adsorbed citric acid over this pH range. The measured forces between hafnia surfaces in the presence of 10^{-1} M, 10^{-2} M, and 10^{-3} M citric acid are presented in Figure 5.6 and show that the surface forces exhibit a strong repulsion at all pH values, both when the surfaces were approaching and upon separation. That is, no primary minimum is observed and hence no strong adhesion in contact was observed upon separation. The absence of a primary minimum which might be expected within the DLVO framework due to dispersion forces, is attributed to the surface roughness[203] and steric repulsion due to the adsorbed citrate[249]. As the salt concentration is increased there is evidence of a small attraction or secondary minimum at a surface separation greater than 5 nm that is sufficient to cause particle flocculation. This secondary minimum, which arises due to the different form of interaction potentials associated with the van der Waals attraction and the electrolytic repulsion, is discussed further in §5.3.5. In a previous investigation of citric acid adsorption onto zirconia surfaces, Biggs et al. reported small steps (8~12 Å) immediately before the hard contact between zirconia surfaces in the presence of citric acid.[249] However, our results show no such steps at any of the citric acid concentrations or pH values examined. The rougher surfaces in the previous study may have enabled the citric acid to be displaced at high contact pressures.

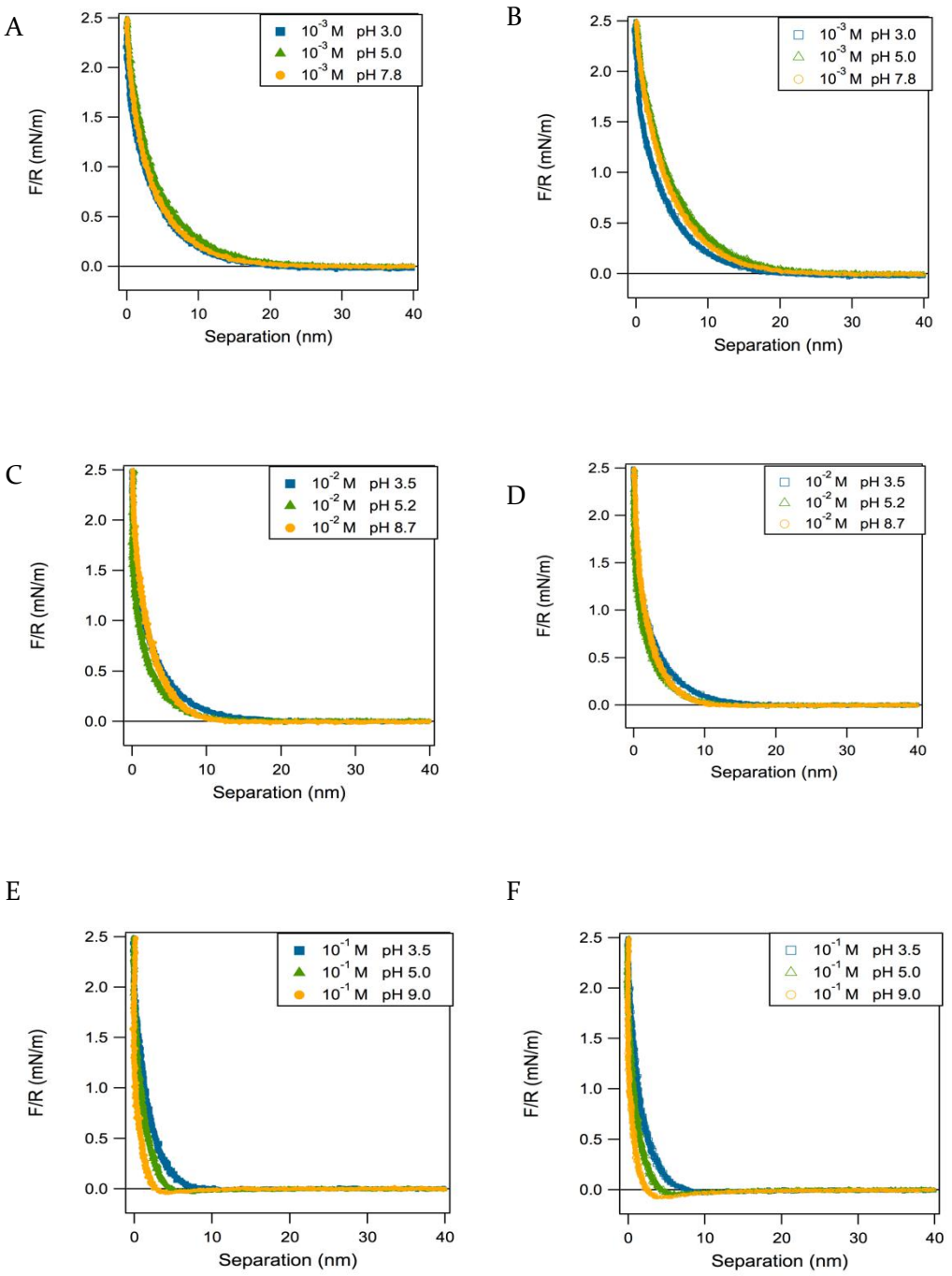

Figure 5.6: Force normalized by radius (F/R) versus separation measured on approach (left, Panels A, C, E) and separation (right Panels B, D, F) between hafnia surfaces in the presence of 10^{-3} M (Panels A & B), 10^{-2} M (Panels C & D), and 10^{-1} M (Panels E & F) of citric acid in NaCl 10^{-3}M solution, highlighting the pH effect across different concentrations. The range of the force decreases with increasing concentration of citric acid due to a decrease in the Debye length. (Data captured by S. Shinohara)

5.3.4 *DLVO fitting, including the effect of roughness*

The force curves shown in Figure 5.6 were further examined by fitting the data using DLVO theory by solving the nonlinear Poisson-Boltzmann equation in accordance with the algorithm described by Chan et al. (See §2.3.2).[98] The influence of surface roughness, [201 , 203] that was investigated extensively in chapter 4, was also included. The hafnia-citrate surface roughness was modeled with a gaussian rms roughness of 0.54 nm which was determined from tapping mode AFM images of the hafnia surface. The Young's modulus of hafnia used was 57 GPa[257]. A retarded Hamaker coefficient calculated by assuming 0.25 mg/m^2 of citric acid using the 'thin-Rayleigh' multilayer Model[83] was used for the fitting (See Appendix-A §A.2.2). Note that when the surface roughness is taken into account the surfaces never reach a hard contact at zero separation. This is due to the asperities on one surface making contact with the asperities on the other surface preventing the surfaces coming into zero separation, where the position of each surface is defined at the average position of the surface roughness.

5.3.4.1 *Surface forces at high pH*

At pH values above the iep of hafnia, the zeta-potential and OR results indicated that the amount of citric acid adsorbed onto the hafnia surface was relatively small. The surface forces measured between hafnia surfaces in the presence of varying concentrations of citric acid at high pH are shown in Figure 5.7. The measured forces exhibited a strong repulsion at all concentrations of citric acid due to electric repulsion. This is in good agreement with the zeta potential of hafnia in citric acid solution, which was around -60 mV (Figure 5.3). The range of the repulsive force decreased with increasing citric acid concentration due to the decreasing Debye length.

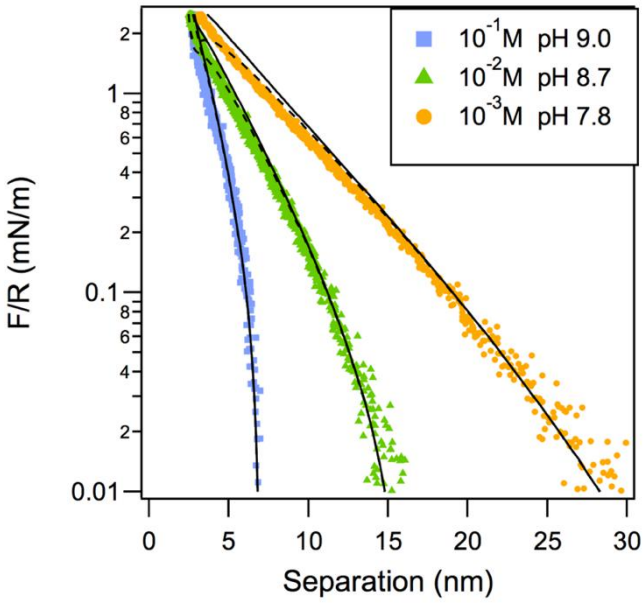

Figure 5.7: F/R versus separation measured on approach between hafnia surfaces in the presence of citric acid at high pH. The citric acid concentrations were 10^{-3}M (circle), 10^{-2}M (triangle) and 10^{-1}M (square). The two theoretical fits represent the boundary conditions of constant charge (solid line) and constant potential (dotted line). The fitting parameters used were: (10^{-1} M) κ^{-1} = 1.3 nm, Ψ_o= -79.0 mV; (10^{-2} M) κ^{-1} = 2.8 nm, Ψ_o= -61.7 mV; (10^{-3} M) κ^{-1} = 4.8 nm, Ψ_o= -69.3 mV

5.3.4.2 *Surfaces forces at circumneutral pH*

At pH 5.0, which is near the iep of the substrate, the surface charge of hafnia is neutral and HX^{2-} is the dominating citric acid species in bulk solution (Figure 5.4). Adsorption led to a change in the zeta potential of hafnia from 0 mV to -50 mV when citric acid was added at pH 5 (Figure 5.3). There are relatively more positive sites for citrate binding on the hafnia surface at this pH than at higher pH, therefore, slightly more adsorption of citric acid was observed. The surface forces measured between hafnia surfaces in the presence of varying concentrations of citric acid at pH ~5 are shown in Figure 5.8. The measured forces exhibited a strong repulsion at all concentrations of citric acid due to electric repulsion as expected by the large magnitude of the zeta

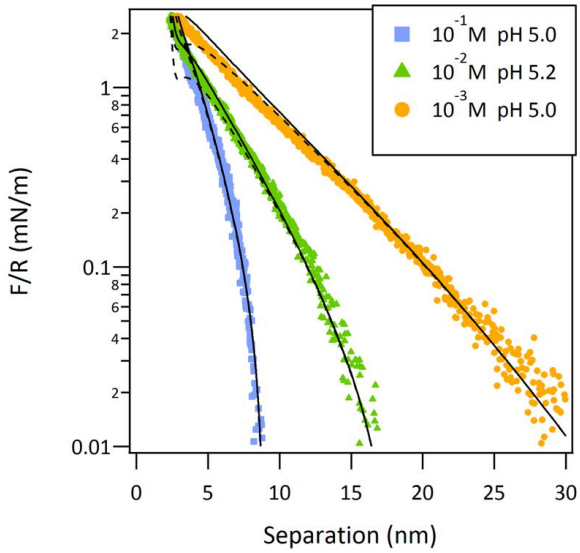

Figure 5.8: F/R versus separation measured on approach between hafnia surfaces in the presence of citric acid at pH 5. The citric acid concentrations were 10^{-3}M (circle), 10^{-2}M (triangle) and 10^{-1}M (square). The two theoretical fits represent the boundary conditions of constant charge (solid line) and constant potential (dotted line). The fitting parameters used were: (10^{-1} M) κ^{-1} = 1.7 nm, Ψ_0= -73.0 mV; (10^{-2} M) κ^{-1} = 3.1 nm, Ψ_0= -55.6 mV; (10^{-3} M) κ^{-1} = 5.2 nm, Ψ_0= -68.6 mV

potential. Notably in the absence of citric acid, as presented in chapter 4 (Figure 4.10 and Table 4-1), the surface potential is near zero and the electric interaction is negligible ensuring that the attractive van der Waals forces dominate.[201] Thus particles in the absence of citric would flocculate readily, whereas in the presence of citric acid they are stable in solutions of low to moderate salt concentration. The influence of electrolyte concentration on the secondary minima is discussed in the later section (§5.3.5.2).

5.3.4.3 *Surface forces at low pH*

Optical Reflectometry (OR) showed that the amount of citric acid adsorbed onto hafnia was approximately 0.09 mg/m^2 when the citric acid concentration was 10^{-3} M at pH ~3. At the same pH, the zeta potential of hafnia in the presence of citric acid was around -30 mV. The surface forces measured at this pH is consistent with the optical reflectometry (OR) and zeta potential data, in that a strong electric repulsion is observed at all concentrations of citric acid (Figure 5.9). In chapter 4, the surface forces between hafnia surfaces in the absence of citric acid was also repulsive (see figure 4.4), [201] however the repulsive force in that case was due to the electric double layer between positively charged hafnia surfaces. Whereas, the repulsion observed when citric acid is present arises from the negatively charged surfaces due to the charge reversal that accompanies adsorption of citric acid. The electric repulsion will ensure that dispersions of particles even at pH~ 3 will be stable at salt concentrations up to > 1 mM.

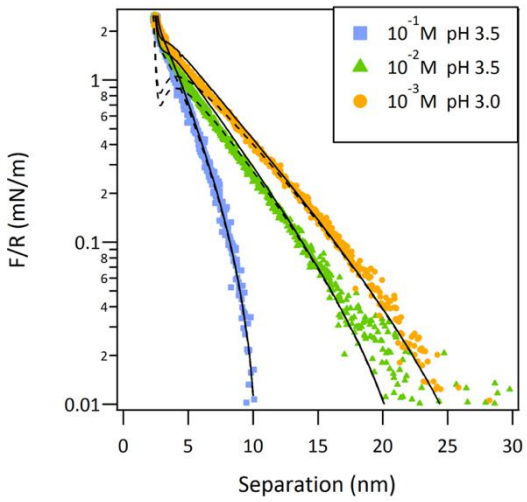

Figure 5.9: F/R versus separation measured on approach between hafnia surfaces in the presence of citric acid around pH 3. The citric acid concentrations were 10^{-3}M (circle), 10^{-2}M (triangle) and 10^{-1}M (square). The two theoretical fits represent the boundary conditions of constant charge (solid line) and constant potential (dotted line). The fitting parameters used were: (10^{-1} M) κ^{-1} = 2.0 nm, Ψ_0= -61.0 mV; (10^{-2} M) κ^{-1} = 3.8 nm, Ψ_0= -52.0 mV; (10^{-3} M) κ^{-1} = 4.5 nm, Ψ_0= -55.6 mV

The surface potential determined from fitting the surface forces using the DLVO theory with roughness is presented in Table 5-1. The surface potential increases with pH but is largely unaffected by increasing citric acid concentration. This is consistent with the zeta potential and optical reflectometry (OR) measurements.

Table 5-1: Surface potential determined from DLVO fitting to the AFM force profile. A surface roughness of 0.54 nm rms was used. The surface potential increases with the pH of the solution.

	Citric acid concentration		
	0.1 M	0.01 M	0.001 M
pH 3	-61.0 mV	-52.0 mV	-55.6 mV
pH 5	-73.0 mV	-55.6 mV	-68.6 mV
pH 9	-79.0 mV	-61.7 mV	-69.3 mV

The decay length which is used as a measure of the thickness of the electric double layer is determined from the best fit to the AFM force profile and compared to the theoretical Debye length calculated from the concentration of citric acid (accounting for speciation) and the NaCl background electrolyte used in the measurement are shown in Table 5-2. Note that the calculated Debye length takes into account the change in the ionic valence of citric acid depending on the pH. Both experimentally measured decay length and calculated Debye length were shorter at high pH because of the domination of the X^{3-} citric acid species in solution contributing to the higher ionic strength. When the experimental and the theoretical values are compared, a significant disparity was observed.

Table 5-2: Debye length for each citric acid concentration and pH studied. κ^{-1} exp. (nm) and κ^{-1} cal. (nm) are the decay length determined from the best fit to the AFM force profile and the theoretical Debye length, respectively.

	Citric acid concentration								
	0.1 M			0.01 M			0.001 M		
	pH 3.5	pH 5	pH 9	pH 3.5	pH 5.2	pH 8.7	pH 3	pH 5	pH 7.8
κ^{-1} exp. (nm)	2.0	1.7	1.3	3.8	3.1	2.8	4.5	5.2	4.8
κ^{-1} cal. (nm)	0.94	0.53	0.39	2.9	1.6	1.2	7.1	4.7	3.6

The experimentally measured decay length was longer than the calculated Debye length. Such a disparity is not observed in solutions containing only 1:1 electrolytes. This disparity can be explained by the asymmetry of the electrolyte. For an asymmetric electrolyte the Debye length and the decay length should not coincide, as the decay length depends on which ion is abundant near the surface and also the type of the electrolyte, for example whether it is 1:2 ($CaCl_2$) or 2:1 (Na_2SO_4).[258] Furthermore, we expect that the depletion of the multivalent species from the double layer due to like charge repulsion would extend the decay length.

In the investigation of the surface forces between the same hafnia surfaces in the absence of citric acid, presented in chapter 4 (Figure 4.10), the best fit to the experimental data was achieved with a surface roughness parameter of 1.2 nm rms. However, in this chapter where citric acid was adsorbed onto the hafnia surfaces, this value was found to be too high, rather an rms roughness of 0.54 nm gave the best fit. This implies that the citric acid adsorbs in a manner that reduces the effective surface roughness. That is, the citric acid may preferentially adsorb in surface hollows.

5.3.5 *Secondary minima and flocculation*

Flocculation is commonly observed at high salt concentrations regardless of the solution pH in rheology. To understand this, we need to look for evidence of a secondary minimum. I have calculated the secondary minima in the interaction energy from the DLVO-R fit to the experimental interaction forces between hafnia surfaces in the absence of citric acid presented in the chapter 4 (Figure 4.9 and Figure 4.1) and in the presence of citric acid (Figure 5.7, Figure 5.8, and Figure 5.9) presented in this chapter. Note that the data from the theoretical fit is used to remove the effect of experimental noise.

The force is divided by two, to account for the interaction between two identically sized spheres rather than a sphere-flat interaction, and then integrated as per the Derjaguin approximation[104] to give the interaction energy between two spheres;

$$U(x) = \int_h^\infty F(x')dx' \tag{5.2}$$

where *U(x)* is the separation dependent interaction energy and *F(x')* is the separation dependent force. The interaction energy has been shown in units of k_BT versus separation in nm as it allows the importance of the depth of the minima to be evaluated. A minima with a depth of 50 k_BT or more will give rise to very rapid flocculation, whereas a minima with a depth of > 10 k_BT is stable or lead to very slow flocculation.

5.3.5.1 *Secondary minima between hafnia particles*

Here I am presenting the secondary minima for the surface forces obtained between hafnia surfaces in the absence of citric acid. The DLVO-R curve fit (1.2 nm rms roughness assumed) for the repulsive force data obtained between hafnia surfaces presented in the chapter 4 (Figure 4.9 and Figure 4.10) were analyzed to verify the existence of a strong secondary minima that would indicate flocculation at pH values remote from the iep in salt solutions.

This is presented in Figure 5.10. This reveals that significant secondary minima (> 10 k_BT) are present and that these would cause flocculation at pH values remote from the iep if the ionic strength is sufficient. Thus, adjustment of the pH to the iep will result in flocculation in a primary minimum, causing particles to strongly adhere when they collide, which would infer open flocs (low fractal dimension) that are difficult to dewater, whereas flocculation by increasing the ionic strength at pH values remote from the iep will result in flocculation in a secondary minima allowing particles to move relative to each other and thereby form denser flocs (higher fractal dimension) that are more easily dewatered.

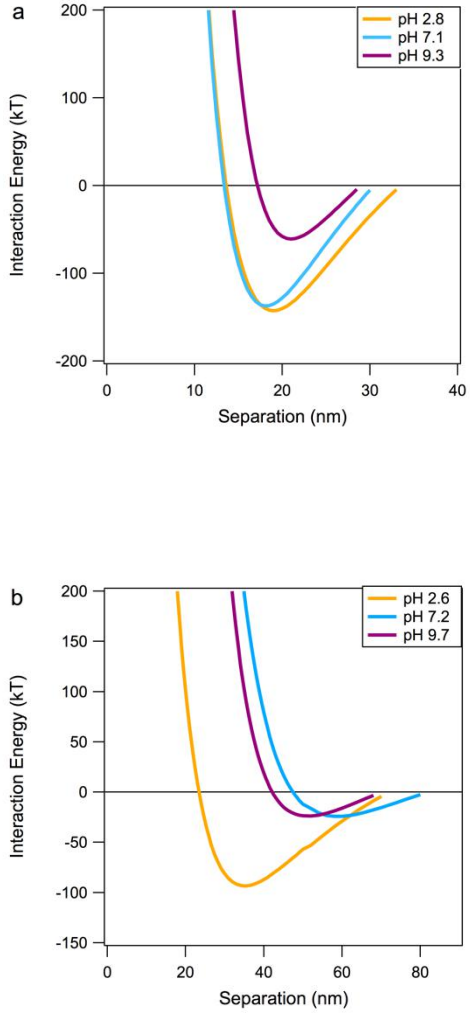

Figure 5.10: Interaction energy (k_BT) calculated from the DLVO-R theoretical fit (constant charge) to the repulsive force measured in 10 mM (a) and 1 mM (b) NaCl at pH away from iep (Chapter 4, Figure 4.9 and Figure 4.10) for the hafnia particles with radius 10 μm in the absence of citric acid. The predicted secondary minima are 143 k_BT , 137 k_BT , and 61 k_BT for pH 2.8, pH 7.1, and pH 9.3, respectively in 10 mM NaCl and 93 k_BT , 24 k_BT and 24 k_BT for pH 2.6, pH 7.2, and pH 9.7, respectively in 1 mM NaCl

5.3.5.2 *Secondary minima between hafnia particles in the presence of citric acid*

Returning to the interaction in the presence of citric acid, the interaction energy (k_BT) calculated for the hafnia colloidal particles with radius 10 μm and for the nanoparticles with radius 50 nm at a range of citric acid concentration is presented in Figure 5.11. As the forces scale with the radius it is possible to determine the forces for 50 nm particles from measurements between larger particles. We note that presently it is not possible to directly measure the interactions between particles with a radius of 50 nm. The zeta potential measurements and the surface force data demonstrate that citric acid stabilizes particles at a wide range of pH due to electric repulsion. In contrast, many metal oxides have isoelectric points at near neutral pH, thus in the absence of citric acid these systems would be unstable within this pH range. Thus, nanoparticles and colloidal particles of these materials will remain dispersed in the presence of citric acid under pH conditions under which they might normally flocculate and sediment. This is significant as the citrate ion is present in the biosphere in the blood,[243] in bones[242] and in soils[259] and the rhizosphere[246, 260-261] at significant concentrations.

Further, citric acid is a model system for humic and fulvic acids, which are also present in soils and natural waters.[259] Therefore, nanoparticles and colloidal particles of a wide range of materials are stabilized by the adsorption of citric acid or humic/fulvic acids in our environment.[220] As dispersed particles they will be readily transported by flow and by diffusion.

However, the stability of particles can also be adversely influenced by increases in ionic strength. This is seen in the surface forces measurements where at higher concentration of electrolytes there exists a range of separations over which the interaction is attractive (see Figure 5.6-F). In this region of secondary minima, particles are attracted to each other, but are not in physical contact, as such the particles flocculate and sediment. As the particles are not in physical contact the particle-particle friction is minimized and the arrangement of the particles within a floc are free to reorder. The low friction is evidenced by the lack of hysteresis between the approach and retraction force data. This generally results in dense flocs (as opposed to open

flocs which occur when particles strongly adhere with high rolling friction). Also because the particles are not strongly adhered they are readily redispersed if the ionic strength of the solution is reduced.

The interaction energy (k_BT) versus separation (Figure 5.11- top) shows that in 1 mM electrolyte the colloidal particulate systems will be stable. Whereas, upon increasing the citric acid concentration to 10 mM and higher the colloidal particles are no longer stable in solution. Similarly, the colloidal systems are unstable at the higher electrolyte concentrations of 0.01 M and 0.1 M (Figure 5.12 - top). Note that the minima occur at substantial particle-particle separations indicating that the particles are not in physical contact and therefore the structure of the colloidal flocs can easily deform and rearrange and the particles can easily be redispersed if the concentration of electrolyte is reduced.

In contrast, the secondary minima for nanoparticles 50 nm in radius is very much shallower as shown in Figure 5.11 (bottom) and Figure 5.12 (bottom), ensuring that the nanoparticles are stable even at high salt concentrations. Note this calculation does not include the reduction in the dispersion forces that takes place for particles less than 100 nm in radius[202]. If this effect were included the secondary minima would be even shallower. This shows that nanoparticles with citrate adsorbed are stable at high ionic strengths where colloidal particles are unstable and highlights the extreme stability conferred on nanoparticles by the adsorption of citrate. That is nanoparticles in the presence of citrate are stable across a wide range of pH and ionic strengths and are only unstable at pH ~2, which is the iep of the citrate-particle system.

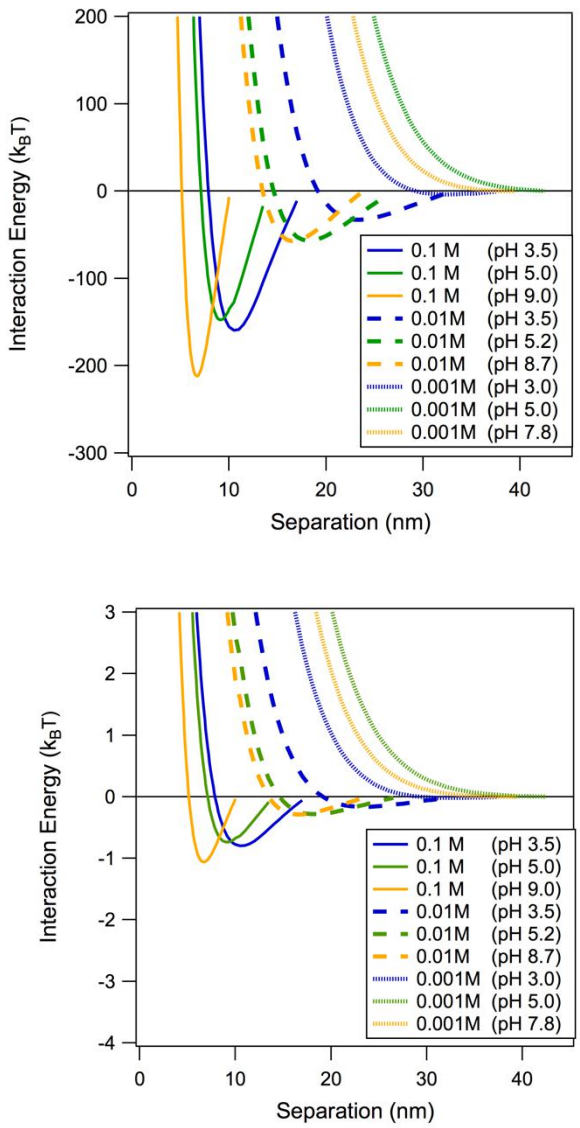

Figure 5.11: Interaction energy (k_BT) calculated by integrating the force data from the DLVO-R theoretical fit (constant charge) to the experimental data presented in Figure 5.7, Figure 5.8, and Figure 5.9 for the colloidal particles with radius 10 μm (top) and for the nanoparticles with radius 50 nm (bottom). The data from the theoretical fit is used to remove the effect of experimental noise. Note that the concentration in the legend indicates the citric acid concentration. Here the background electrolyte is 0.001 M NaCl. The secondary minima values are tabulated in Table 5-3.

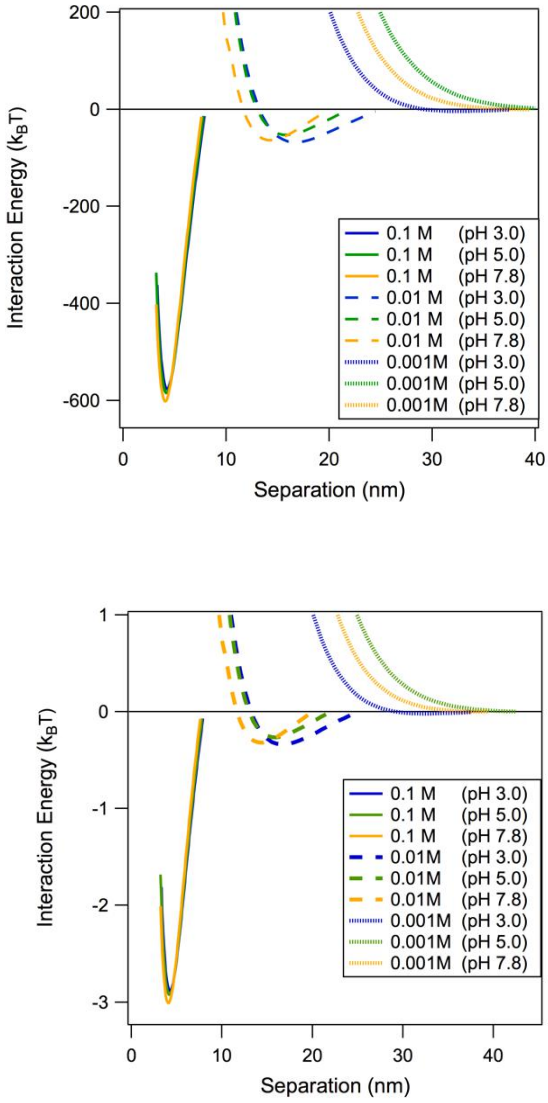

Figure 5.12: The effect of concentration of the background electrolyte (NaCl) on the interaction energy (k_BT) calculated for the 0.001 M citric acid (see Figure 5.11). Theoretical secondary minima are obtained for both particle sizes 10 μm (top) and 50 nm(bottom) at a range of salt (0.001, 0.01, and 0.1 M NaCl) concentrations in the presence of 0.001 M citric acid. Note that the concentration in the legend indicates the NaCl concentration. The secondary minima values are presented in Table 5-4.

Table 5-3: Secondary minima in the interaction energy between two spherical 10 micron hafnia particles and between 50 nm hafnia nanoparticles in the presence of citrate

		Citric acid concentration		
		0.1 M	0.01 M	0.001 M
10 µm	pH 3	159 k_BT	33 k_BT	4 k_BT
	pH 5	148 k_BT	56 k_BT	Not Applicable
	pH 9	212 k_BT	57 k_BT	Not Applicable
50 nm	pH 3	0.8 k_BT	0.2 k_BT	0.02 k_BT
	pH 5	0.7 k_BT	0.3 k_BT	Not Applicable
	pH 9	1.1 k_BT	0.3 k_BT	Not Applicable

Table 5-4: Secondary minima in the interaction energy between two spherical 10 micron hafnia particles and between 50 nm hafnia nanoparticles in the presence of 0.001 M citrate at a range of NaCl concentration

		NaCl concentration		
		0.1 M	0.01 M	0.001 M
10 µm	pH 3	576 k_BT	68 k_BT	4 k_BT
	pH 5	585 k_BT	53 k_BT	Not Applicable
	pH 8	602 k_BT	64 k_BT	Not Applicable
50 nm	pH 3	2.9 k_BT	0.3 k_BT	0.02 k_BT
	pH 5	2.9 k_BT	0.3 k_BT	Not Applicable
	pH 8	3.0 k_BT	0.3 k_BT	Not Applicable

5.3.5.3 *Stability and distribution of nanoparticles and colloidal particles in the environment*

Increased production of nanoparticles is leading to an accumulation of anthropogenic nanoparticles in the environment and growing concerns over possible health implications[262-265]. The fate, transport and interactions of these nanoparticles in the environment are determined by the surface properties and the stability, which is influenced by the pH, ionic species, naturally occurring organic matter and clay materials[264]. The size of particles and particle aggregation is not only important in soils and waterways but also affects exposure sites and pathways and ultimately the toxicity in biological systems[266-268]. Moreover aggregation decreases the dissolution rate of particles[269]. The surface forces demonstrate that adsorption of citrate to colloidal particles and nanoparticles confers solution stability over a wide range of pH, moreover, for nanoparticles this stability remains even at high ionic strength. This demonstrates that exposure of nanoparticles, such as titania nanoparticles, in the environment to naturally occurring organic materials such as humic acids, fulvic acids or citric acid leads to nanoparticles that are stable in solution across a very wide range of pH and ionic strength. The result is that nanoparticles are prevented from aggregating and are present as primary particles, which are readily dispersed and available for uptake, whereas bare particles would readily flocculate which would reduce their dispersion and largely prevent biological uptake.

5.4 SUMMARY

The influence of the adsorption of citric acid to hafnia surfaces on the interaction forces has been investigated. Ultrasmooth hafnia has been used as a model metal oxide surface and the trends observed are applicable to a wide range of metal oxide surfaces. Citrate adsorption increases with decreasing solution pH. Upon adsorption, the citric acid layer shifts the surface potential of the metal oxide to more negative values such that the surface potential

becomes significantly negative at all pH values of 3 and above in the presence of citric acid. The substantial magnitude of the surface potential gives rise to a significant electric repulsion between particles, which prevents aggregation. The surface force measurements confirm that citric acid is a very effective stabilizer for metal oxide particles as the surface forces were always repulsive and no primary adhesion was observed, even at low citric acid concentrations. At high electrolyte concentrations the electric repulsion is screened and a secondary minima is evident for colloidal sized particles. This will cause aggregation and flocculation. As the aggregation is due to a secondary minima, the flocs will be dense and easily re-suspended if the ionic strength is reduced or shear forces are exerted. In contrast nanoparticles are stabilized by citrate even at high ionic strengths. The stability of nanoparticles in the presence of citrate ions will favour the transport of nanoparticles *in vivo*, in soils and in the aquatic environment as citric acid (or humic and fulvic acids) is often present at significant concentrations. The implications for the distribution of nanoparticles in our environment are significant given the widespread distribution of man-made nanoparticles in air [263] and concerns over their impact on human health.

CHAPTER 6

EFFECT OF A PALMITIC ACID MONOLAYER ON THE SURFACE FORCES BETWEEN HAFNIA SURFACES

6.1 INTRODUCTION

It is desirable in many circumstances to functionalise hydrophilic surfaces to render them hydrophobic. This can be achieved by surface modification involving the formation of covalent bonds to produce robust hydrophobic surfaces, such as the silanisation of glass surfaces[270]. Alternatively amphiphilic molecules can be physisorbed to surfaces to render them hydrophobic by the Langmuir-Blodgett technique for insoluble amphiphiles or by adsorption from solution for soluble amphiphiles.

In this chapter, I investigate the surface forces between surfaces made hydrophobic by deposition of a water insoluble amphiphile via the vapour phase. The surface hydrophobicity is characterised by the contact angle. The surface forces measured between hydrophobic surfaces are known to give rise to an attraction not present between hydrophilic surfaces. A long-ranged attractive force between macroscopic hydrophobic surfaces was first reported by Israelachvili and Pashley in 1982[118]. Measurements using the surface forces apparatus (SFA) between mica surfaces rendered hydrophobic by the physisorption of the cationic surfactant cetyltrimethylammonium bro-

mide (CTAB) exhibited an unexpected attraction which far exceeded the calculated van der Waals attraction, and therefore could not be described within the framework of the Derjaguin Landau Verwey and Overbeek (DLVO) theory[20-21]. The observation of an additional interaction observed between hydrophobic surfaces came to be known as the hydrophobic force or the long-range hydrophobic attraction. The first experimental report of this force sought a relationship between the long-range hydrophobic attraction with the hydrophobic effect[271], which is responsible for the aggregation and self assembly of hydrophobic molecules in aqueous solution, but the relationship is yet to be resolved.

Measurements of the surface forces between hydrophobic surfaces have revealed interaction forces that vary widely in range and in magnitude. Papers reporting the largest and longest-range interactions can now be attributed to the interaction of surface nanobubbles[127-129] – which are in themselves somewhat mysterious[130-131]. Whilst this is interesting and relevant in many situations, here we put measurements between surfaces decorated with nanobubbles aside, as others do[272], as we wish to concentrate on the interaction between macroscopic hydrophobic surfaces in the absence of surface nanobubbles.

Once the results that are likely due to nanobubbles are excluded there still remains an attraction not described by the DLVO theory between hydrophobic surfaces that extends up to separations of ~30 nm.[122-123, 126] Amongst these measurements the interaction force is variable. This variability is attributed to the nature of the hydrophobic surface. Forces measured between relatively smooth and stable hydrophobic surfaces produced by chemisorption have been reported to be in the range of < 10-20 nm,[125, 273-274] whereas surfaces prepared by physisorbed surfactants have resulted in longer ranged forces (> 20 nm)[275-276].

Here I use vapor phase adsorption to physically adsorb a monolayer of amphiphile to a hydrophilic surface. This results in a significant increase in hydrophobicity. Whilst the method of preparation is different, the system is related to previous investigations in which insoluble monolayers were deposited onto hydrophilic surfaces using the Langmuir-Blodgett technique[277-

[278] The non-DLVO attraction between LB deposited films has long been attributed to the mobility of the amphiphiles.[126] Initially, the mobility was thought to lead to rearrangements in the amphiphile distribution within the monolayer. More recently the interaction has been attributed to the formation of patches of bilayer and patches of bare surface, resulting in regions of different surface charge[70, 279]. When surfaces interact it is favourable for amphiphiles to migrate such that positively charged patches align with negatively charged patches, resulting in an electrostatic attraction. Theoretical analysis reveals that for a mosaic of patches this interaction is exponential, with a decay length of $\kappa^{-1}/2$[280] and is strongest when the overall surface charge is neutral.[216-217]

Attempts have been made to measure the interaction forces between inherently hydrophobic surfaces[32], but it is difficult to prepare these surfaces with the extremely low level of roughness that is desired for accurate, precise and easily interpretable surface force measurements. The interactions between solid polymer surfaces have been investigated but these surfaces were not as smooth as desired[32, 281]. A successful approach for eliminating the influence of surface roughness so that the hydrophobic interaction can be evaluated is to employ liquid droplets[282].

In this chapter, I used atomic layer deposition (ALD) prepared smooth hafnia surfaces as the substrate for exposure to palmitic acid vapour which readily results in the self-assembly of a monolayer of palmitic acid rendering the surface hydrophobic. The surface hydrophobicity is characterised by the contact angle and via surface force measurements.

6.2 EXPERIMENTAL METHOD

6.2.1 *Vapour deposition of palmitic acid*

Surfaces were water vapor plasma cleaned for 90s at 30 W, followed by 30 s at 50 W immediately before the palmitic acid vapor treatment. Surfaces were

then placed in a clean glass petri dish, along with palmitic acid (Sigma, Hexadecanoic acid, Sigma Grade Approx. 99%). To expose the surface to palmitic acid vapour, the petri dish containing the surfaces and palmitic acid powder was placed into an oven. The surfaces were arranged such that when the palmitic acid powder melted no direct contact with the surfaces was made. Various treatment temperatures (75 °C, 110 °C, 135 °C) and durations (5 min, 30 min, 60 min) were examined to determine the optimal conditions for forming a hydrophobic monolayer as determined by the highest advancing and receding contact angles. Once the vapor treatment was completed, the flat surfaces were rinsed with distilled ethanol for 2 s and rinsed under purified water for 5 s and then dried under a stream of pure N_2 gas. Colloid probes were rinsed by dipping in clean distilled ethanol multiple times. The roughness of the ALD hafnia surface with palmitic acid monolayer was determined from an AFM image (1000 nm x 1000 nm) using a Bruker multimode 8 AFM in ScanAsyst mode in air, using a Bruker ScanAsyst-Air cantilever.

Ellipsometry (M2000D, JA Woollam) was used to determine the thickness of the palmitic acid layer formed after the vapor treatment. It is easier to fit the ellipsometric data with fewer surface layers. Hence, for ellipsometry, the hafnia was deposited directly onto a Si substrate. A 33.0 nm thick hafnia layer was produced from a total of 400 cycles, in which each deposition cycle consisted of a 0.5 s pulse of Hf precursor, followed by a 20 s nitrogen purge, then a 0.015 s pulse of water, followed by a 20 s nitrogen purge. Nitrogen was used as the carrier gas at a flow rate of 20 sccm.

6.2.2 *Contact angle measurement*

The contact angles of a range of hydrophobised oxide surfaces were investigated. ALD prepared titania (TiO_2), ALD prepared zirconia (ZrO_2), ALD prepared hafnia (HfO_2), and Si wafer (the native surface is oxidized to SiO_2) were used as substrates and hydrophobised via the palmitic acid vapour treatment. The ALD deposition conditions employed for the surfaces are shown in Table 6-1. The thicknesses of the ALD produced layers were determined to be 38.0 nm for titania, 13.1 nm for zirconia, and 12.7 nm for hafnia.

Table 6-1: The ALD deposition condition for the titania, zirconia, and hafnia surfaces used for the contact angle measurements. Nitrogen was used as the carrier gas at a flow rate of 20 sccm (standard cubic centimetre per minute).

	Precursor Temperature (°C)	ALD Reaction Temperature (°C)	Total number of cycles	Pulse duration (s)
Titania	100	80	800	Ti: 0.5 Nitrogen: 7 Water: 0.5 Nitrogen: 5
Zirconia	75	200	180	Zr: 0.25 Nitrogen: 15 Water: 0.02 Nitrogen: 15
Hafnia	75	250	141	Hf: 0.5 Nitrogen: 20 Water: 0.5 Nitrogen: 20

Advancing and receding contact angles of aqueous solutions on the various surfaces (SiO_2, HfO_2, TiO_2, ZrO_2) were measured using a contact angle goniometer (CAM200, KSV, Helsinki, Finland), with a reported accuracy of ±1°. A micro syringe (GASTIGHT #1001, 0–1 ml, Hamilton Co., Reno. Nevada, USA) with a blunt dispensing needle (victor-g.com., 27G x 26 mm) was used to create the droplet on the surface. Measurements were performed at ambient temperature (22 ± 2 °C). Liquid was continuously added to measure the advancing contact angle and continuously removed to measure the receding contact angle. Profiles of the liquid drop on the surface were captured

at a rate of 20 frames/s. The advancing and receding contact angles were measured using the instrument software and identified respectively as the maximum and minimum value before the contact line moved. To investigate the contact angle dependence on the pH of the solution, solutions of 0.001 M NaCl ranging from pH 3 to pH 9 were prepared by adding an appropriate amount of sodium hydroxide or hydrochloric acid. At least 3 surfaces were immersed in each pH adjusted NaCl solution then blown-dry with high purity nitrogen gas before each contact angle measurement.

6.3 RESULTS AND DISCUSSION

6.3.1 *Contact angle measurement*

Contact angles were measured on the ALD prepared surfaces described in section §6.2.2. and the results are reported in Table 6-2. Palmitic acid (PA) treatment in all cases led to a large increase in both the advancing and receding contact angles of water droplets. Treatment of the silicon wafer led to an advancing angle of 78° and a receding angle of 43°. The measured advancing and receding contact angles for both the PA-titania and PA-zirconia surfaces were greater, whilst the PA-hafnia surfaces showed the highest advancing (105 °) and receding contact angles (60 °). For this reason, subsequent measurements focused on the hafnia surfaces. We note that the contact angle may be influenced by the removal of surfactant at the three phase line. It is known that adsorbate can transfer to the liquid air interface, reducing the density on the solid surface, reducing the surface tension of the liquid air interface and reducing the contact angle. However, if this is the case, it supports our decision of choosing hafnia over other surfaces. The contact angle results below show that there is a stronger affinity of palmitic acid for the hafnia surface.

Table 6-2: Advancing and receding contact angles measured on various oxide surfaces after exposure to palmitic acid vapor at 135 °C for 60 min. Both the advancing and receding contact angle were highest on the hafnia surface.

Surface	Advancing contact angle (°)	Receding contact angle (°)
SiO_2	78 ± 2	43 ± 5
TiO_2	96 ± 3	48 ± 5
ZrO_2	97 ± 2	48 ± 6
HfO_2	105 ± 2	60 ± 8

In order to explore the influence of the treatment conditions on the hydrophobicity of the surface, both the advancing and receding contact angles of aqueous 0.001 M NaCl on the palmitic acid treated hafnia surfaces (PA-hafnia) prepared at three different temperatures and durations were measured and are shown in Figure 6.1. The general trend is that the contact angle increased with increasing treatment temperature and duration. Treatment at 75 °C did not result in hydrophobic surfaces even after 60 mins. The maximum advancing contact angle was only ~ 30°. Also, the receding angle on the surfaces treated at 75 °C (5 min and 30 min) were too small to be measured. The advancing contact angle on the surfaces treated at 110 °C increased from approximately 20° to 101° when the treatment duration was increased from 5 min to 30 min. When the duration was increased further to 60 min, the advancing contact angle did not increase significantly, however the receding contact angle increased by a further 9°. Surfaces treated at 135 °C did not show great dependency on the treatment duration. Palmitic acid treatment at this high temperature yielded advancing contact angles of 100 °C and 105 °C when the duration was 5 min and 60 min, respectively. The comparison between the lowest and highest contact angle measured is presented in Figure 6.2 showing the effectiveness of the palmitic acid vapour treatment in hydrophobising the hafnia surfaces.

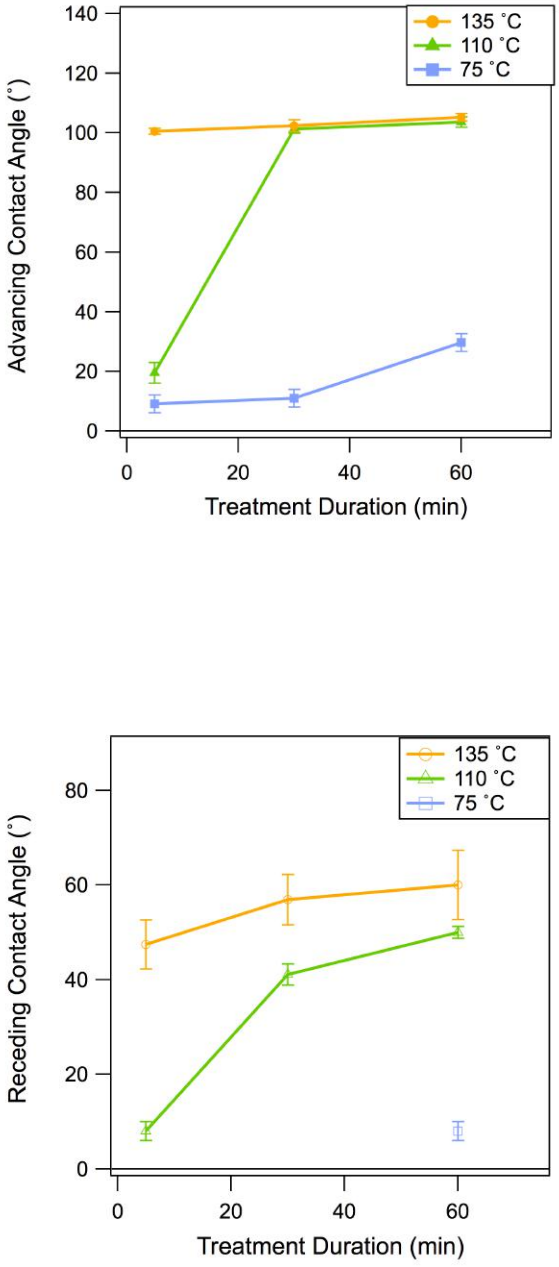

Figure 6.1: The advancing (top) and receding (bottom) contact angle of 0.001 M NaCl on PA-Hafnia surfaces. The error bars reflect the highest and lowest of the 10 measured contact angles for each sample under each condition.

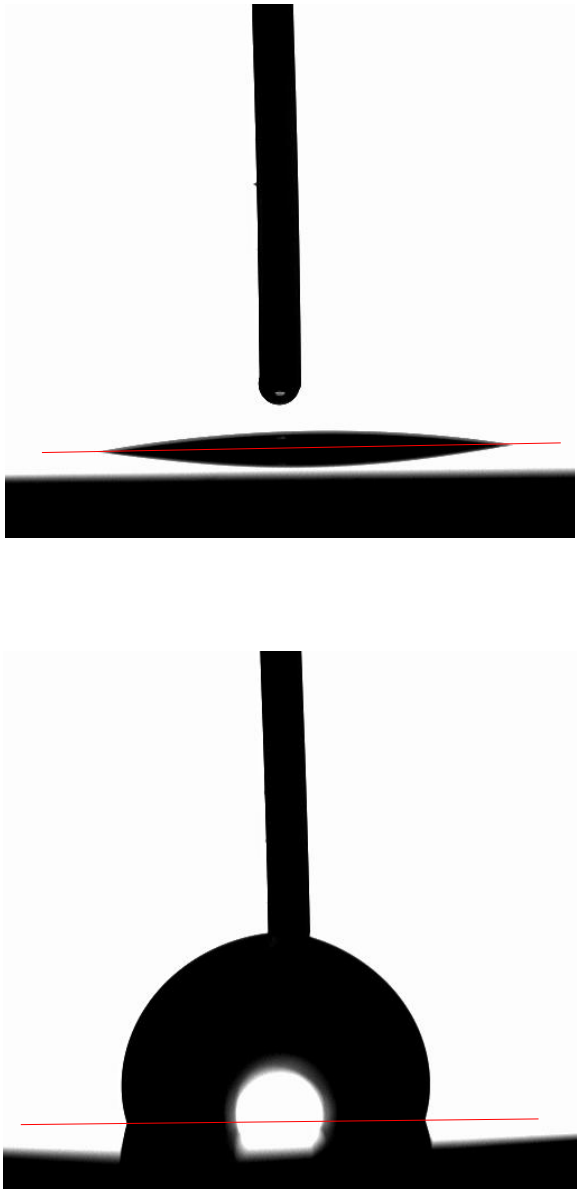

Figure 6.2: The advancing contact angle of 0.001 M NaCl on the hafnia surface treated with palmitic acid at 75 °C for 5 min (top), and the hafnia surface treated at 135 °C for 60 min (bottom). The red solid line indicates the location of the surface. Palmitic acid vapour treatment is found to be a very effective way of hydrophobising the initially hydrophilic hafnia surface. Note that the freshly cleaned hafnia surface using the radio frequency water plasma was extremely hydrophilic (completely wetting) before any palmitic acid vapour treatment.

6.3.1.1 *Contact angle change over time*

Hydrophobic surfaces immersed in water are known to become progressively more hydrophilic (as measured by the contact angle with water) over time. This may be attributed to loss of the hydrophobising agent for physisorbed films, but this is also observed for chemisorbed films, where it has been shown that the hydrophobising layer is still intact[270]. In order to investigate the influence of immersion on the hydrophobicity, the contact angle on the surfaces was measured after immersion in aqueous NaCl 0.001 M for 24 hours (Figure 6.3). It is evident that longer treatment times and higher treatment temperatures generally produce surfaces with the highest post-immersion contact angles. The advancing and receding angle on the surfaces treated at 75 °C were too small to be measured after 24 hours of immersion. Advancing contact angles on the PA-hafnia surface treated at 135 °C and 110 °C for 60 min decreased to nearly the same value of approximately 92 degrees. However, the receding contact angle of the PA-hafnia surface treated at 135 °C was 8 ° higher than the one treated at 110 °C. This shows that the hydrophobicity after immersion was highest when the surface was treated at 135 °C for 60 min. This treatment temperature and duration were used to study the effect of pH on the stability of the contact angle on PA-hafnia surfaces.

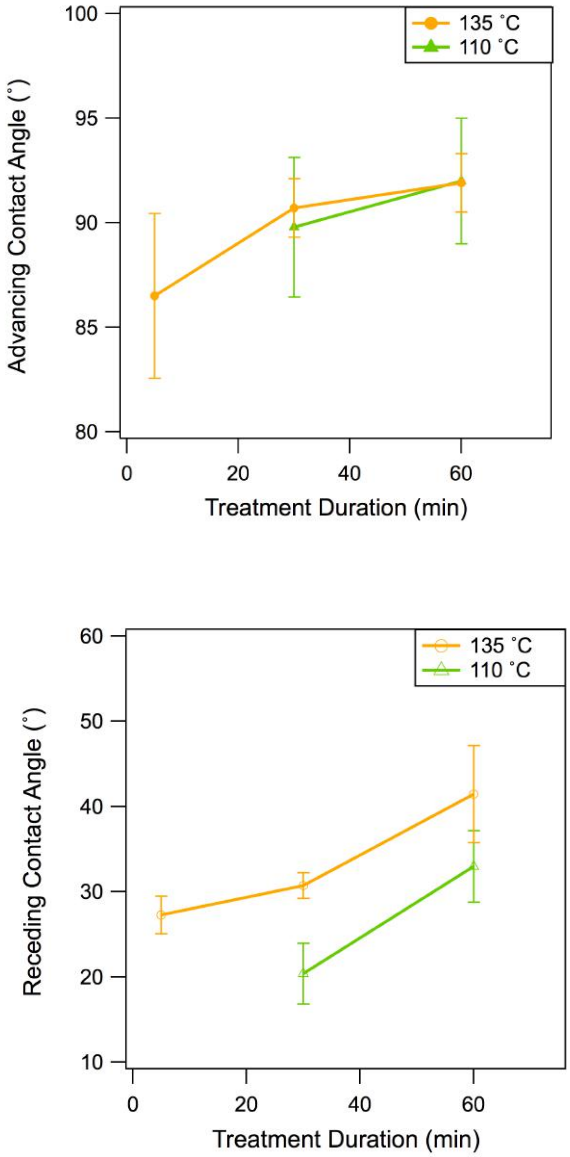

Figure 6.3: The measured advancing (top) and receding (bottom) contact angle of 0.001 M NaCl on PA-Hafnia surfaces after immersion in 0.001 M NaCl for 24 hours.

6.3.1.2 *The effect of pH on the contact angle*

The effect of pH on the contact angle of aqueous droplets on the PA-hafnia surfaces over time were measured both initially and after immersion in 0.001 M NaCl at the same pH for different time periods (Figure 6.4). Once removed from solution the surfaces were briefly blown dry under a stream of purified nitrogen gas before the contact angle was measured. The general trend observed is that the contact angle decreased with increasing pH, and with immersion time. Results show that the contact angle at the lowest pH (3.2) is highest and remained so over time. The advancing contact angle remained above 90 ° even after 12 hours of immersion at pH 3.2. On the contrary, at pH 9.6, the advancing contact angle on the PA-hafnia surface was initially only 82 ° and this dropped further to 37 ° after only 1 hour of immersion. The relatively poor stability at high pH and the high stability of the palmitic acid treatment at low pH is attributed to the low water solubility of fatty acids at low pH.[283-284] The hysteresis in the contact angle is also presented in Figure 6.4. The large contact angle hysteresis observed is characteristic of a surface that is either heterogeneous or mobile[126].

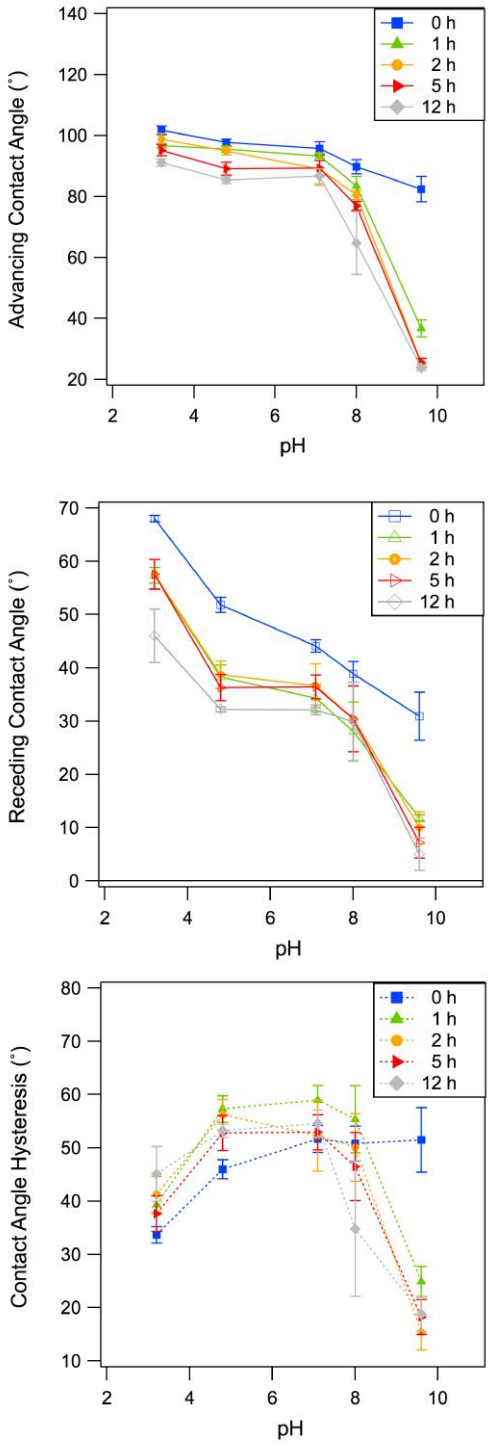

Figure 6.4: Advancing and receding contact angle of droplets of pH adjusted 0.001 M NaCl solutions on PA-hafnia surfaces formed at 135 °C for 60 min as a function of immersion time in pH adjusted 0.001 M NaCl aqueous solutions. The hysteresis between the advancing and receding contact angles is presented in the lower panel.

6.3.2 *Characterisation of the palmitic acid layer*

The thickness of the palmitic acid layer formed on the hafnia surface after vapor treatment at 135 °C for 60 min was determined by comparing ellipsometric data from the hafnia surface both before and after palmitic acid treatment (Figure 6.5). The thickness and the refractive index of the palmitic acid layer estimated using a Cauchy model were 1.0 ± 0.3 nm and 1.5 ± 0.1 (at 630 nm), respectively. The measured thickness is smaller than the length of the palmitic acid molecule which is 1.89 nm[285]. Assuming the layer is a complete monolayer the measured thickness indicates that the molecules within the monolayer are tilted approximately 32 ° ± 11 ° from the normal to the surface.

Atomic Force Microscope images of the bare hafnia and PA-hafnia surfaces in air are shown in Figure 6.6. The images were used to measure the rms roughness of the surfaces, which was found to be 0.6 ± 0.2 nm across all scales on both images, indicating that the adsorption of the palmitic acid did not increase the surface roughness or change the texture of the images. This indicates that in air the palmitic acid is evenly distributed across the surface in a monolayer film.

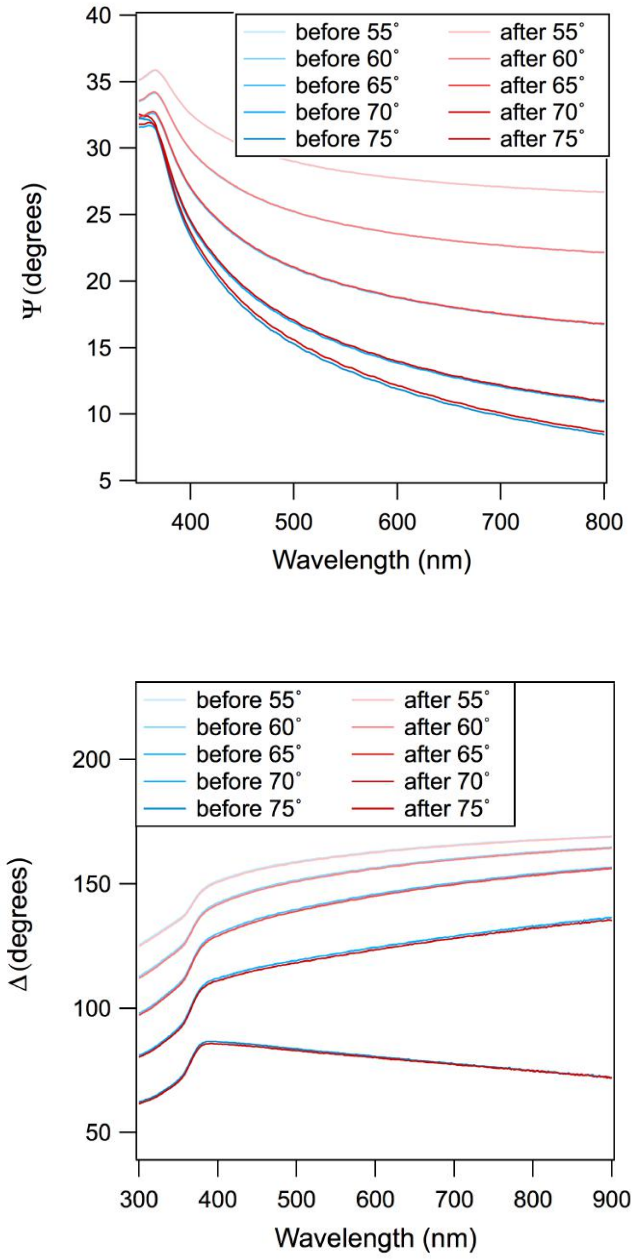

Figure 6.5: Measured spectra (Ψ, Δ) of ALD hafnia surface before and after treatment with palmitic acid. The data measured before and after the PA treatment do not show much difference as the thickness of the monolayer is only approximately 1 nm.

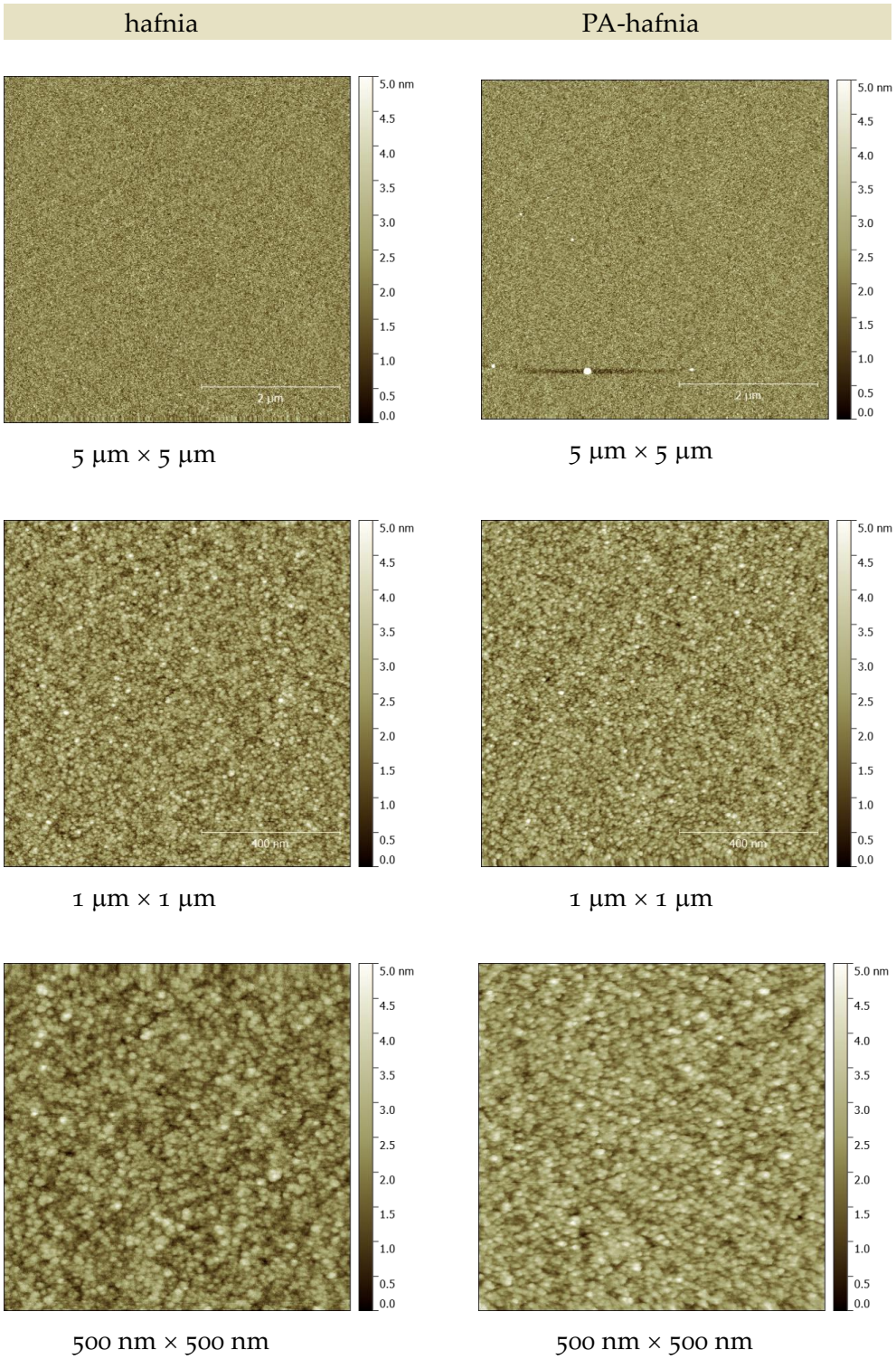

Figure 6.6. AFM images of the ALD hafnia surface and the ALD hafnia surface with palmitic acid at different magnification. The texture of the images is unaffected by the adsorption of palmitic acid. The z-scale in the image is 5 nm.

6.3.3 *Zeta potential*

Colloidal particles of hafnia both untreated and treated with palmitic acid were used for zeta potential measurements. Hafnia powder (99.95 % pure) supplied by Materion (H-1011) was used as the substrate for zeta-potential measurements. The zeta-potential of the hafnia surface in 0.001 M NaCl solution before and after palmitic acid vapor treatment at 135 °C for 60 min is presented in Figure 6.7. The isoelectric point (iep) of the hafnia surface before the palmitic acid vapor treatment was at pH ~5. When the hafnia surface is treated with palmitic acid vapor, the iep shifted to pH ~3.5. This indicates that the palmitic acid is adsorbed in a neutral state to the surface, but when immersed in NaCl solution it is in the deprotonated form even at low pH, which is below the pK_a of the acid. It is known that adsorption to surfaces causes a decrease in the apparent, pK_a^{app}, of carboxylic acids.[284] The same phenomena is observed for low molecular weight carboxylic acids adsorbed to metal oxide surfaces[256].

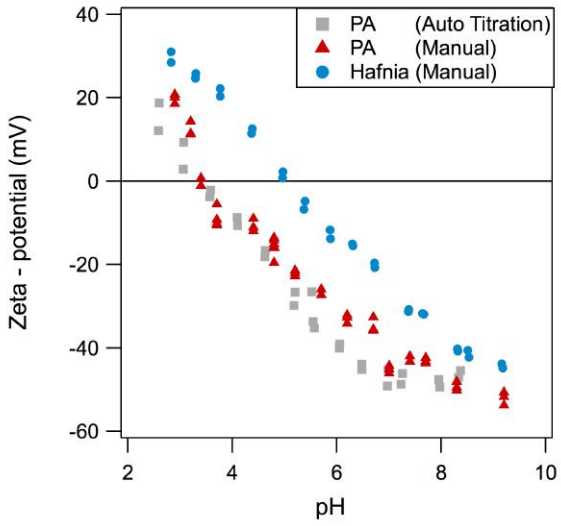

Figure 6.7: Zeta-potential as a function of pH for hafnia particles in 0.001 M NaCl solution, before (Hafnia) and after (PA) the surfaces were exposed to palmitic acid (PA) vapor at 135 °C for 60 min. Two measurements of the latter are shown, using manual pH adjustment and autotitration. The shift in the isoelectric point to lower pH is attributed to adsorption of the palmitic acid in the deprotonated state.

6.3.4 *Surface forces between PA-hafnia surfaces*

The surface forces between palmitic acid treated hafnia surfaces (PA-hafnia) were measured using an atomic force microscope with a colloid probe attached to the cantilever. There is a possibility that the palmitic acid monolayer is damaged during force measurement. This would result in the order of the measurement influencing the result measured at each pH. In order to minimize this possibility, different colloid probes were used for measurements at each pH. The forces measured at a range of pH are shown in Figure 6.8. At pH 3.2, which is close to the iep, the absence of an electric repulsion reveals an attractive force. At pH values both below (pH 2.6) and above (pH 5.2 and pH 7.2) the iep, the surfaces are charged and a long-range electric repulsion is evident. In this case, the forces are initially repulsive before an attraction is observed that causes the surfaces to jump into contact. The jump-in occurs when the separation is approximately 20 nm and 15 nm at pH 5.2 and pH 7.2, respectively. The long-range attractive forces evident in these measurements between hydrophobic surfaces are not described by DLVO theory.

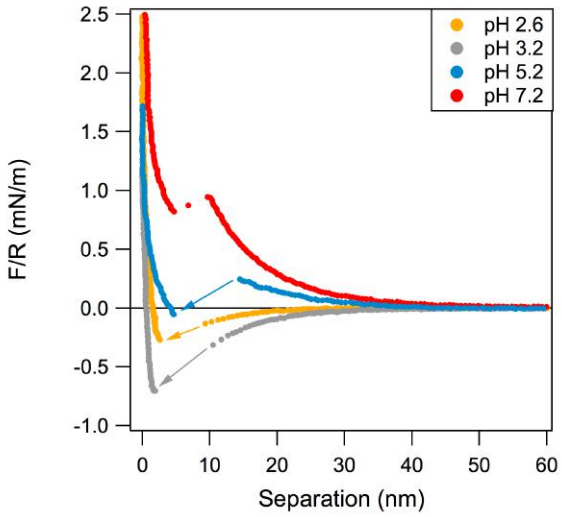

Figure 6.8: The normalized force (F/R) measured as a function of separation between PA-Hafnia surfaces during approach. The surfaces were exposed to palmitic acid vapour for 60 mins at 135 °C. In all cases a large attractive force or an attractive jump, indicated by an arrow, is evident at a separation greater than 15 nm. This extra attraction not described by DLVO theory is generally attributed to the long-range hydrophobic attraction.

It has been reported that chemisorbed hydrophobic surfaces with a high surface contact angle and a robust monolayer are prone to be decorated with nanobubbles.[286] During force measurement surface nanobubbles form a bridge between the surfaces that results in a long-range attraction.[128] Force curves with and without surface bubbles have been previously investigated.[122] It has been reported that in the presence of surface bubbles, the measured attractive forces were long-ranged (50~150 nm) and that when bubbles were removed from the hydrophobic surfaces, the attractive forces became shorter-ranged (10~20 nm). The force curves obtained in this study are comparable to those reported previously in the absence of bridging bubbles.[122-123] Here, repeated force measurements at the same location and at

three different locations for each pH were reproducible. The interaction exhibited only minor variations at the different locations (see Figure 6.9). This indicates that the interactions observed are not due to the presence of nanobubbles and also indicates that the surface treatment is reasonably uniform, which is consistent with the AFM images of the PA-hafnia surfaces.

In order to more fully understand the measured interactions, I have compared the experimental data to the DLVO theory extended to account for surface roughness (DLVO-R)[203] with a distance-dependent Hamaker coefficient calculated assuming a 1 nm thick palmitic acid layer on hafnia/titania/silica/silicon multilayer. The effect of the palmitic acid layer is to reduce the magnitude of the dispersion forces. The dielectric functions of each layer, silicon[287] , silica[288], titania[79] , hafnia[289] are blended to provide an effective dielectric function for the whole surface.[49, 83] I represent palmitic acid using the dielectric function of hexadecane[290]. The short-range behaviour (<10nm) is

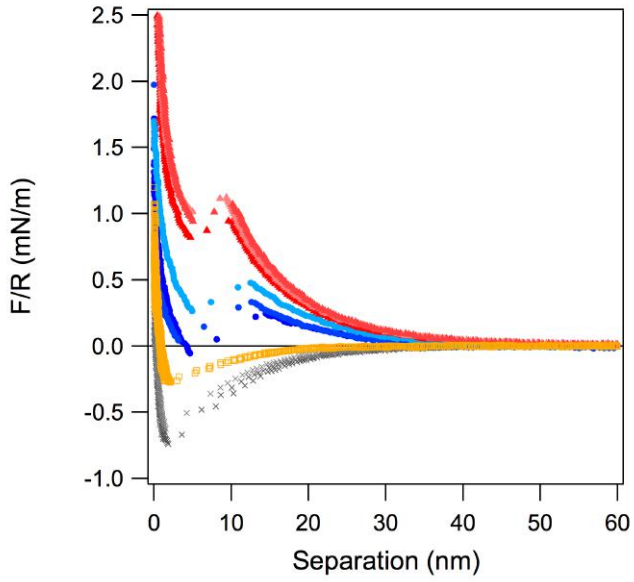

Figure 6.9: Normalised force versus separation measured between PA hafnia surfaces prepared at 135 °C for 60 min, in three different locations at pH 3.2 (Grey ×), pH 2.6 (Orange □), pH 5.2 (Blue ●), and pH 7.2 (Red ▲).

dominated by palmitic acid, which alone has a nonretarded Hamaker constant of 6.7 zJ. The hafnia (and underlying titania) layer dominates the van der Waals interaction at mid-range distances 10-100 nm (the pure nonretarded Hamaker constant of hafnia is 56.3 zJ). At long-range distances (>200 nm) the van der Waals interaction is controlled by the underlying silicon substrate, but is also attenuated by retardation. A plot of the distance-dependent Hamaker coefficient and mathematical details are given in the Appendix-A (Figure A.2). Overall, the effect of the palmitic acid layer is to reduce the magnitude of the dispersion forces, particularly at short range.

6.3.4.1 *Forces measured above the isoelectric point*

The measured normalized force versus separation at different immersion times in 0.001 M NaCl adjusted to pH 5.2 and pH 7.2 measured during the approach and retraction is shown in Figure 6.10 and Figure 6.11, respectively, along with fits to the data using DLVO theory corrected for roughness (DLVO-R theory) [203]. The fitting was conducted over the repulsive portion of the interaction, ignoring the jump to contact – i.e. ignoring the attraction usually attributed to the long-range hydrophobic force, which is not considered in DLVO theory. At pH 5.2 (Figure 6.10), the force was repulsive down to a separation of ~ 10 nm before the surfaces jumped into contact. When the force was measured 1 hour later, the electric repulsive force had become stronger and the attractive jump to contact occurred at a reduced separation of ~ 5 nm. A similar trend was observed at pH 7.2 (Figure 6.11). The electric repulsion increased over time and the separation at which the jump to contact occurred decreased slightly. At both pH, the adhesion force decreased over time. The surface potential change observed over 1 hour was -36.0 mV and -20.0 mV at pH 5.2 and pH 7.2, respectively. These changes in the surface potential over time and the changes in the measured interaction are attributed to instability of the palmitic acid film at these higher pH values leading to a decrease in hydrophobicity. The contact angle at these pH values was less stable than at low pH, thus, it is reasonable to propose that the extra attraction attributed to the hydrophobicity of the surfaces decreased between the measurements.

At these pH values, PA coated surfaces are negatively charged, thus at larger separations, surfaces will experience the electric double layer repulsion. However, at small separations, the short-range hydrophobic attraction will dominate the interaction force. Over time, as the hydrophobicity of the surfaces decreases, this decrease in the magnitude of the hydrophobic force results in an increase in the magnitude of the repulsive interaction which when fitted using DLVO-R theory is manifested as an increased surface potential. It is probable that the surface potential has not changed significantly over time, but rather the hydrophobic force that is counteracting the electric repulsion has decreased.

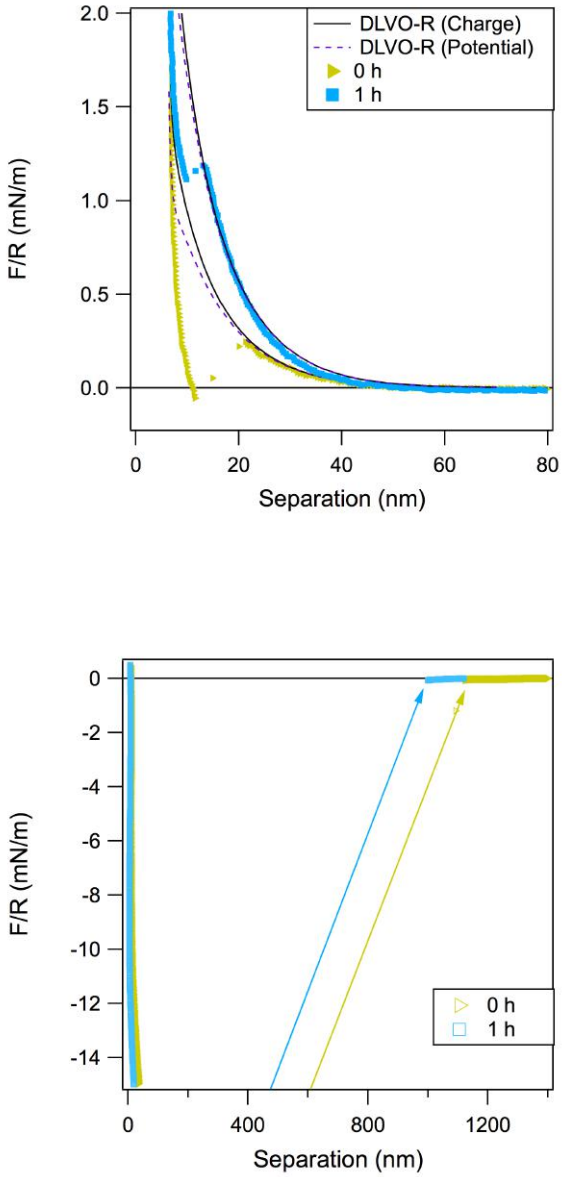

Figure 6.10: Normalised force (F/R) as a function of separation between PA-hafnia surfaces prepared at 135 °C for 60 min as a function of immersion time at pH 5.2 during approach (top) and retraction (bottom). The measured data was fitted with DLVO-R theory (surface roughness of 1.2 nm rms, asperity radius of 4 nm, and the Young's Modulus of 57 GPa) using the van der Waals attraction and with the following fitting parameters; surface potential (0 hr) = -63.3 mV, surface potential (1 hr) = -99.4 mV. The Debye length was 9.6 nm.

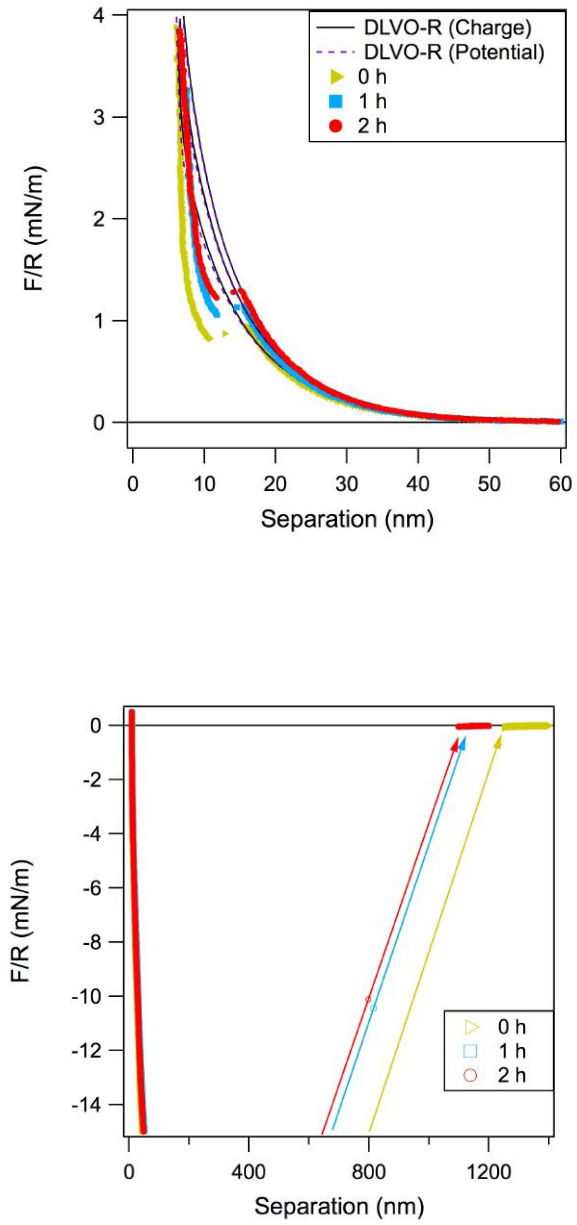

Figure 6.11: Normalised force (F/R) as a function of separation between PA-hafnia surfaces prepared at 135 °C for 60 min as a function of immersion time at pH 7.2 during approach (top) and retraction (bottom). The measured data was fitted with DLVO-R theory (surface roughness of 1.2 nm rms, asperity radius of 4 nm, and the Young's Modulus of 57 GPa) using the van der Waals attraction and with the following fitting parameters; surface potential (0 hr) = -103.4 mV, surface potential (1 hr) = -123.3 mV, surface potential (2 hr) = -142.2 mV. The Debye length was 9.6 nm.

6.3.4.2 *Forces measured below and at the isoelectric point*

The measured normalized force versus separation measured at different immersion times in 0.001 M NaCl adjusted to pH 3.2 and pH 2.6 during approach and retraction is shown in Figure 6.12 and Figure 6.13, respectively. When compared to the calculated van der Waals interaction and accounting for roughness, it is clear that the attractive force is greater in magnitude than the expected attraction due to the van der Waals force. It is worth noting that the attraction also exceeds the (larger) van der Waals force calculated for the bare hafnia surfaces without a palmitic acid layer using a Hamaker constant of 56 zJ[201]. Therefore, I conclude that the attraction cannot be attributed to dispersion forces. Measurements were repeated after waiting for 1 and 2 hours in order to determine if any changes in the monolayer of palmitic acid were influencing the hydrophobic force, recalling that the advancing contact angle for this surface at these pH's changed little with time, but the receding angle showed a small decrease (see Figure 6.4). The observation is that the interaction on approach changes little with time at both pH 3.2 and pH 2.6, whereas the decrease in adhesion with time was more apparent. I cannot be certain of the origin of these changes but suggest that it may be due to the gradual solvation of palmitic acid molecules from the surface into solution.

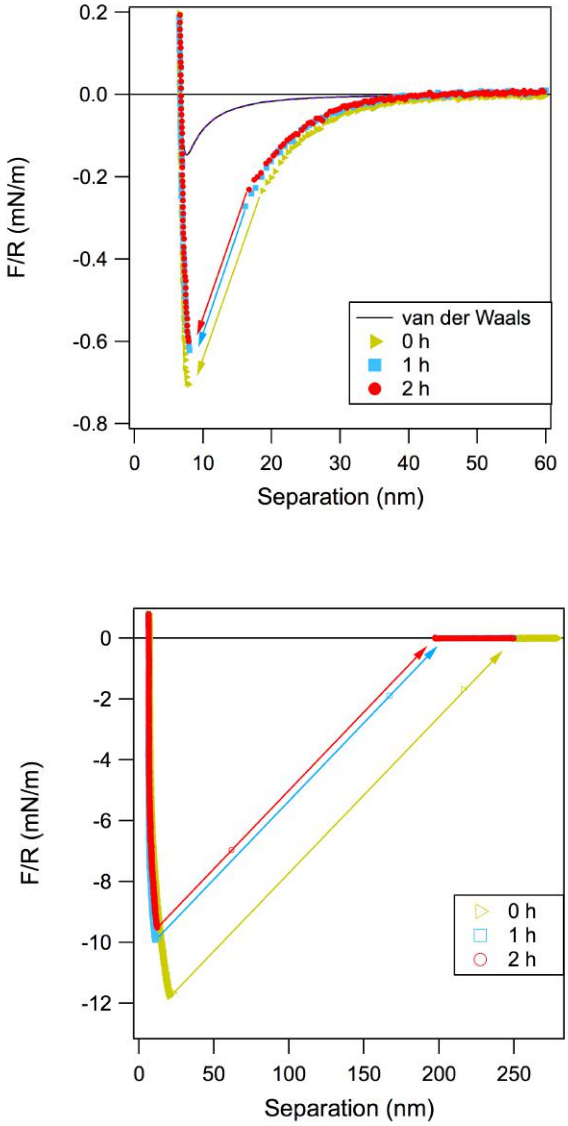

Figure 6.12: The normalized force (F/R) measured as a function of separation between PA-hafnia surfaces prepared at 135 °C for 60 min for different immersion times at pH 3.2 during approach (top) and retraction (bottom) in 0.001 M NaCl solution. The DLVO-R theory curve shown here is the pure van der Waals force with zero surface potential and surface roughness of 1.2 nm rms. Note that when roughness is accounted for the zero of separation is defined relative to the average positions of the surfaces. A hard repulsion occurs at a finite separation due to asperity-asperity contact between the surfaces.[201]

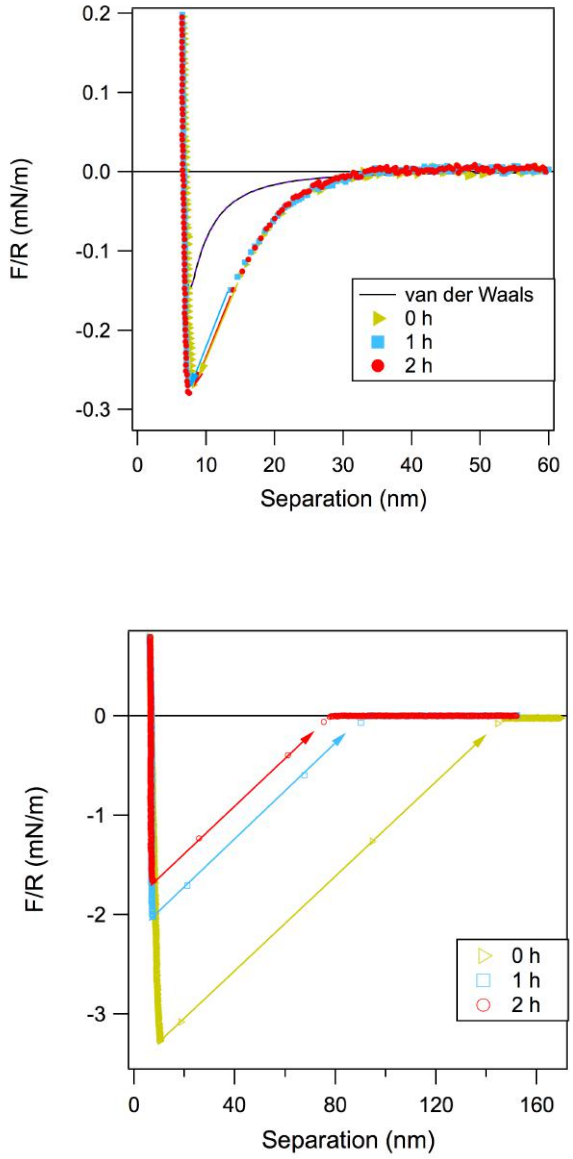

Figure 6.13: The normalized force (F/R) measured as a function of separation between PA-hafnia surfaces prepared at 135 °C for 60 min for different immersion times at pH 2.6 during approach (top) and retraction (bottom) in 0.001 M NaCl solution. The DLVO-R theory curve shown here is the pure van der Waals force with zero surface potential and surface roughness of 1.2 nm rms. Note that when roughness is accounted for the zero of separation is defined relative to the average positions of the surfaces. A hard repulsion occurs at a finite separation due to asperity-asperity contact between the surfaces.[201]

The attractive forces shown in Figure 6.12 and Figure 6.13 appear at a separation of 25 ~ 30 nm and increase exponentially until the surfaces jump into contact from a separation of ~ 10 nm, where the gradient of the force exceeds the spring constant of the cantilever. A typical force curve for physisorbed surfactant surfaces is rather long-range (> 20 nm) and the origin of the long-range attraction between physisorbed surfaces is now generally believed to be attributed to migration of the amphiphile to form bilayer patches.[69-70, 279] The bilayer patches result in a mosaic of regions of positive surface charge and regions of negative surface charge that align during the interaction giving rise to an attraction between the surfaces that are overall electroneutral[216, 280]. Langmuir–Blodgett (LB) deposited monolayers of surfactants such as dimethyl-dioctadecyl-ammonium (DODA) form patchy bilayers when immersed in water.[279] These bilayer patches are believed to freely move laterally on the surface[279] and indeed this is necessary to give rise to an attraction.

Patches on one surface align with patches of opposite charge on the other surface because this lowers the interaction energy. The interaction between net neutral surfaces with mobile charges can lead to a long-range electric attraction[216, 280] therefore this is a possible explanation for the long-range hydrophobic attraction measured between this class of surface. The model predicts an exponentially decaying attractive force with an upper limit for the decay length of one-half the Debye length. However, the force curves obtained here at both pH values (Figure 6.12 and Figure 6.13) can be fitted with an exponential function with a decay length greater than this (see Figure 6.14). The decay length is found to be 6.0 nm at pH 2.6 and 7.1 nm at pH 3.2. This compares to the Debye Lengths for these solutions of 5.1 nm at pH 2.6 and 7.5 nm at pH 3.2. Thus, the patchy charged surfaces model cannot explain the forces presented here, as the decay length is substantially larger than predicted by this model.

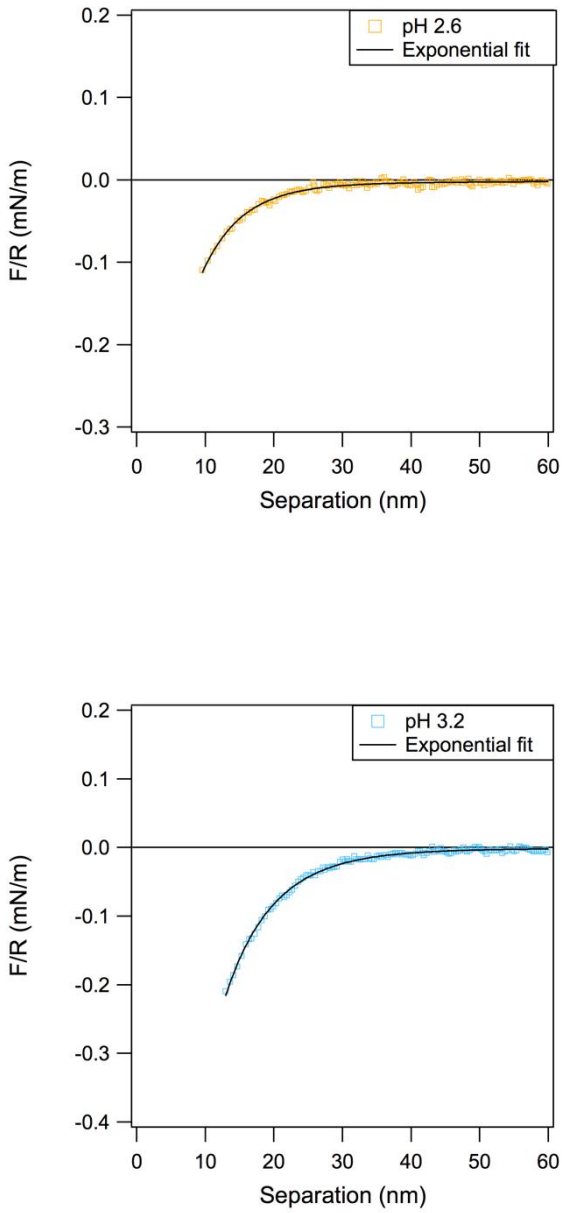

Figure 6.14: Exponential fit to the attractive force curves obtained at pH 2.6 and pH 3.2 in 0.001 M NaCl. The decay length is 6.0 nm with a pre-factor of 0.52 mN/m at pH 2.6 and 7.1 nm with a pre-factor of 1.3 mN/m at pH 3.2. This compares to the estimated Debye Lengths for these solutions of 5.1 nm at pH 2.6 and 7.5 nm at pH 3.2. The exact Debye length is not known as the amount of electrolyte required for the pH adjustment is not known.

6.3.5 *Exponentially decaying attractive force*

An explanation worth consideration is that the surfaces differ slightly and therefore at pH values around the iep it is possible that one surface is negatively charged and the other is positively charged resulting in an electrostatic double layer force between oppositely charged surfaces particularly given the exponential nature of the attraction and that the decay length of the attractive force is commensurate with the Debye length. In order to evaluate if this is the case, the attractive forces measured at pH 3.2 (Figure 6.12) and pH 2.6 (Figure 6.13) were fitted using Equation 4.2 developed by Parsegian and Gingell[94] which I described in Chapter 4 (§ 4.2.7.1). The data are fitted using the van der Waals attraction with the addition of the electric double layer attraction between surfaces of opposite charge, but the same magnitude, taking into account the roughness effect. This fit is performed using the constant potential boundary condition and is shown in Figure 6.15. The asymmetrical surface potentials required to fit the data were +45.1 mV and -45.1 mV at pH 3.2 and +20.0 mV and –20.0 mV at pH 2.6. The magnitude of the surface potentials needed to fit the data is large considering that the surfaces were prepared in the same manner and would therefore be expected to be identical and close to neutral given the proximity of the pH to the isoelectric point. I note here that I chose to use potentials of the same magnitude on each surface such that only one parameter is adjusted. I note that there is no reason to assume that the magnitude of the surface potentials are actually identical. If this constraint is removed then the potential on one surface could be chosen over a wide range and the potential on the other surface adjusted to fit the data. Regardless the two potentials would need to be significantly different to fit the data. Whilst the magnitude of the surface potentials appear to be unreasonably different for surfaces that are prepared in the same manner and remain as prepared, the fitted Debye lengths of 7.1 nm and 6.0 nm compare well with the calculated Debye lengths based on the ionic strength of the pH adjusted solutions of 7.5 nm and 5.1 nm.

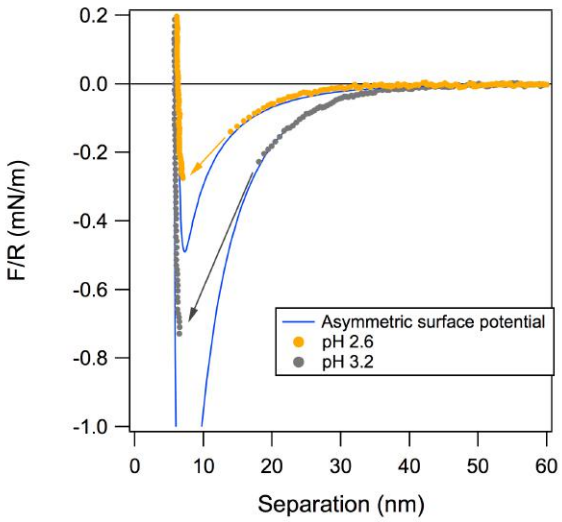

Figure 6.15: The normalized force (F/R) measured as a function of separation at pH 3.2 and pH 2.6 in 0.001 M of NaCl. The measured data were fitted using the van der Waals attraction (see Appendix-A for details of the calculation of the van der Waals interaction) with the addition of the electric double layer attraction taking into account the roughness effect (1.2 nm rms and asperity radius 4 nm, with Young's modulus of 57 GPa). The asymmetric surface potentials and Debye lengths fitted for each pH were as follows; pH 3.2: Surface potential 1 = + 45.1 mV, Surface potential 2 = - 45.1 mV, Debye length = 7.1 nm. pH 2.6: Surface potential 1 = + 20.0 mV, Surface potential 2 = - 20.0 mV, Debye length = 6.0 nm.

6.3.6 *Bilayer patches of palmitic acid*

It is known that Langmuir-Blodgett (LB) films can change configuration in solution[279] and our palmitic acid films formed by vapour deposition are analogous to LB films. Monolayer films can roll up to form bilayered structures that lower the interfacial energy of the film with the solvent. This process may also be triggered by the proximity of another surface due to repulsive electric interactions.

If we consider the possibility that in solution or during approach, the palmitic acid forms bilayered regions on the surfaces, this will leave areas in which the bare hafnia surface is exposed. The hafnia surface will be substantially more positively charged than the regions bearing palmitic acid, as evidenced by the zeta potential data (see Figure 6.7). Further, the regions with a bilayer of palmitic acid will have surface potentials more negative than regions coated with a monolayer and therefore more negative than indicated by the zeta potential. The lower energy state will be for the bi-layered regions of palmitic acid on one surface to align with the bare hafnia regions of the other surface, thus if the palmitic acid molecules are mobile this arrangement will preferentially arise resulting in an attraction between the positively charged hafnia region of one surface with the negatively charged palmitic acid coated region on the other surface – for multiple patches this is the condition which is considered by the patchy charge model[216, 280].

However due to the curvature of the colloid probe in Atomic Force Microscope measurements, the area of interaction between the surfaces is very much smaller than that between measurements using macroscopically curved surfaces such as the surface forces apparatus. The Langbein approximation[291] can be used to determine the effective area of interaction between the spherical colloid probe and the flat substrate typically used in the colloid probe AFM force measurements. This requires knowledge of the radius of the sphere and the range of the interaction. The effective area of interaction depends on the range of the force, a (Figure 6.16). The area of interaction of a colloid probe with radius R then is πy^2. By the Pythagoras theorem,

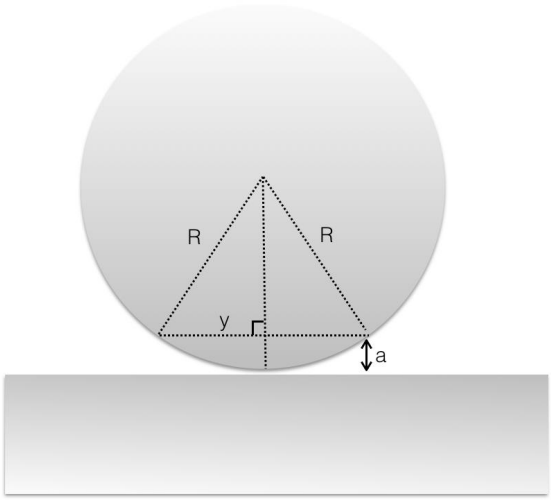

Figure 6.16: A schematic of the effective interaction area of a colloid probe with radius *R* when it interacts over a distance, *a*, with a flat surface

$$R^2 = y^2 + (R - a)^2 \tag{6.1}$$

And thus,

$$y^2 = 2Ra - (a)^2 \tag{6.2}$$

The area of interaction then depends on the radius R and the range of the force a,

$$\pi y^2 = \pi(2Ra - (a)^2) = \pi a(2R - a) \tag{6.3}$$

For a colloid probe with radius $R = 10\ \mu m$, and and interaction force that extends to a distance of $a = 30$ nm, the area of interaction is 1.9×10^6 nm^2, or a circle with radius 778 nm. Therefore, if the bilayer patches are separated by more than this distance, it is likely that a single patch on one surface will interact with a single patch on the other surface.

This is commensurate with the scale of the bilayer patches observed in previous work[279, 292]. In this case, the total interaction can be between a single patch of hafnia surface and a single patch of PA-hafnia surface that form and

align on approach of the surfaces. Such an interaction would be better described by DLVO theory than the patchy charge model, where the electric component of the interaction is due to asymmetrically charged surfaces and the decay length of the electric attraction would therefore correspond to the Debye length of the solution as observed here rather than half the Debye length of the solution as expected for the interaction of patchy charges[280]. Therefore due to the observed decay of the interaction I conclude that in these measurements the long-range attraction that I observe is due to the mobility of the palmitic acid at the interface and the interaction of a bilayered patch of palmitic acid on one surface with a bare region of hafnia surface.

In chapter 4 (§4.2.7.1), I reported that the attractive forces measured between two hafnia surfaces without any surface modification at around the iep also exhibited electrolyte concentration dependency implying its electric nature. I am aware that others have also seen similar exponential attractive forces at the iep (via personal communication with Masashi Mizukami from the Institute of Multidisciplinary Research for Advanced Materials and WPI-Advanced Institute for Materials Research, Tohoku University, Japan). It is possible that this type of electric attraction is due to the same mechanism described above. If a tiny amount of amphiphilic contaminant is present this may result in an exponentially decaying attraction between two asymmetrically charged surfaces with a decay length comparable to the Debye length of the system.

6.3.6.1 *Image of bilayer patches of palmitic acid*

In order to determine if patches form spontaneously when the PA-hafnia surface is immersed in aqueous solution, a PA-hafnia surface was imaged using an AFM both in air and solution (Figure 6.17). The same surface was imaged in air again after being dried under a stream of pure nitrogen gas (Figure 6.18). Images were obtained using a Bruker Multimode VIII AFM in ScanAsyst mode with ScanAsyst Air and ScanAsyst fluid cantilevers as appropriate. Images in solution were obtained using a closed fluid cell. These images show that there are no large scale patches of bilayers, but in water

there is a suggestion that small scale bilayer patches are present which are no longer present when the surface is dried. Note that in one location we found an isolated region of bilayered patches demonstrating that we can image such patches (Figure 6.19). During injection of water onto the surface bubbles are initially trapped on the surface. It is possible that the bilayered structures observed in Figure 6.19 may be formed during this process. Elsewhere the surfaces are very uniform and there was no evidence of such bilayers. I note that the force measurements were found to be reproducible from one location to the next supporting the observation that the surfaces are initially homogenous. This suggests that these patches form and align dynamically during the approach of the surfaces, this is consistent with the sudden onset of the attraction observed at the higher pH values following a region of electric repulsive forces (Figure 6.10 and Figure 6.11). This also explains that the soft repulsion observed after the sudden attraction seen in Figure 6.10 and Figure 6.11 is attributed to squeezing of the bilayers. Thus this interaction may be viewed as a special case of the patchy charge model of surface interaction where the curvature of the surfaces is such that the interaction involves *only one patch on each surface* and because of this the interaction is longer ranged than the case of larger lower curvature surfaces where many patches are interacting[280].

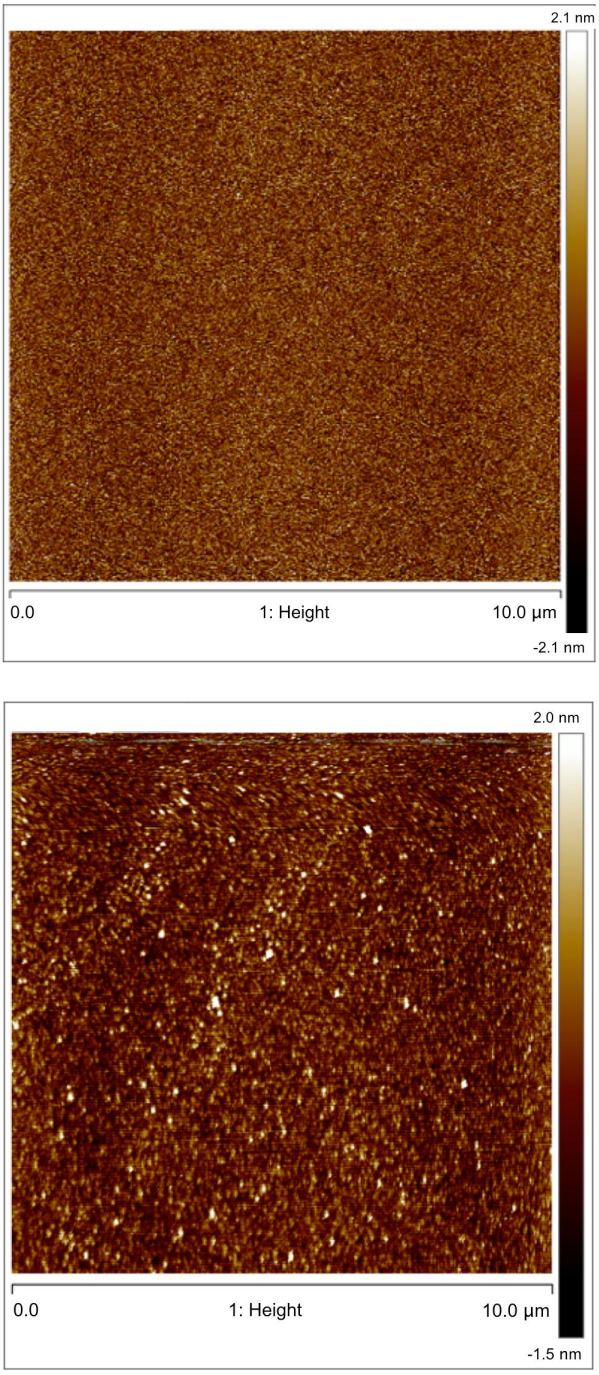

Figure 6.17: AFM height image of the PA-hafnia surface in air (top) and the same surface in water (bottom). rms roughness over a 10 µm x 10 µm scan is 0.59 nm in air and 0.49 nm in water. Note the image obtained in water is blurred in places as the O-ring acts to couple the motion of the surface to the cantilever, reducing the quality of the image.

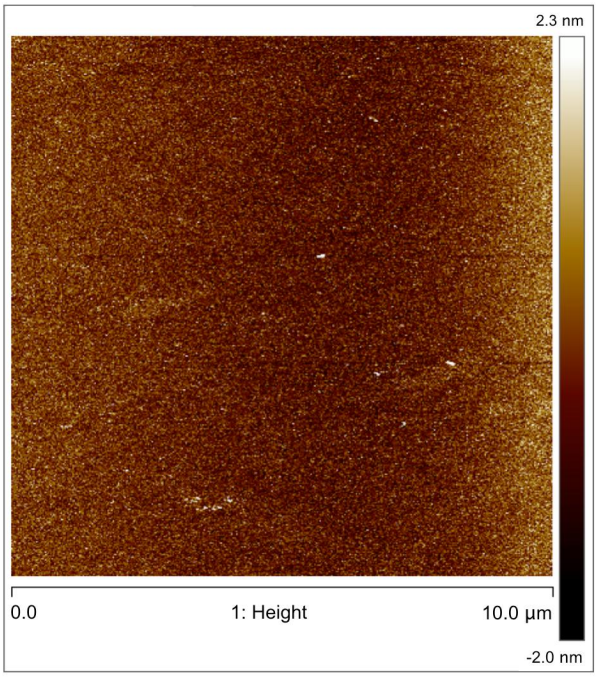

Figure 6.18: AFM height image of the same PA-hafnia surface as in Figure 6.17 after being dried under a stream of pure nitrogen gas and imaged in air. rms roughness is 0.62 nm over a 10 µm x 10 µm scan.

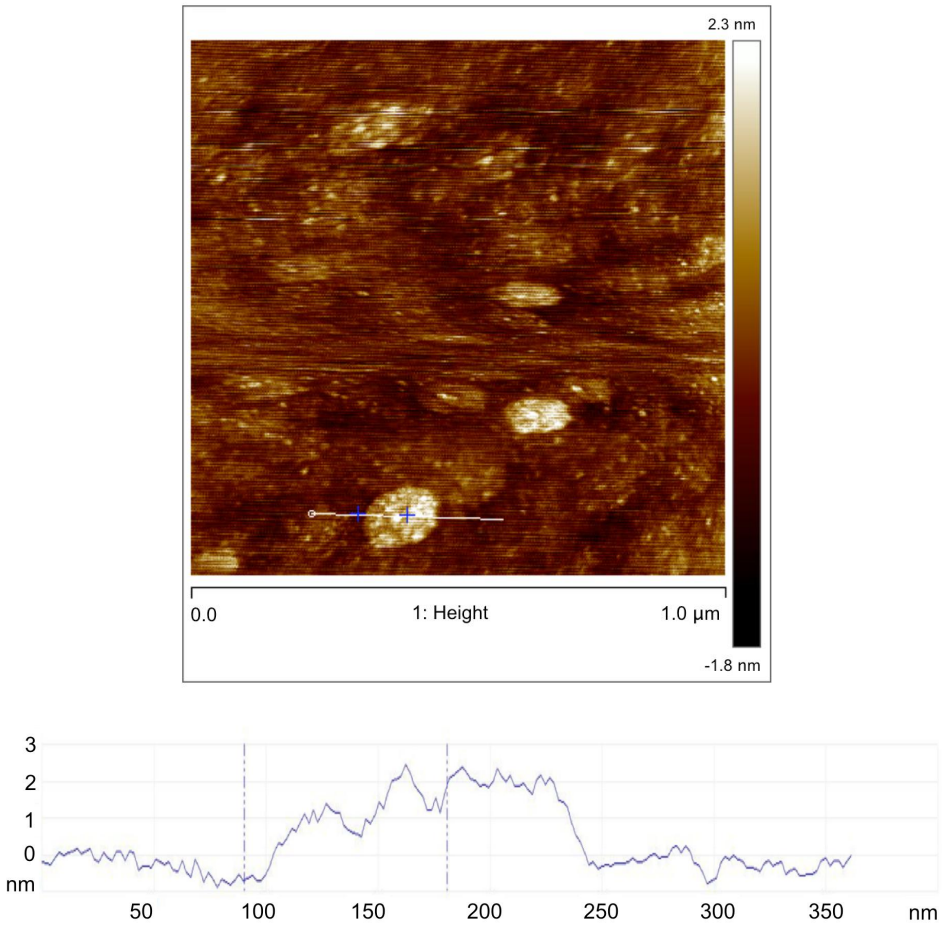

Figure 6.19: AFM height image of the same PA-hafnia surface as above imaged in water with a section across a feature as shown by the white line in the image. 1 µm x 1 µm scan. Note the image is blurred in places as the O-ring acts to couple the motion of the surface to the cantilever, reducing the quality of the image. The height of the section (~ 2 nm above the background) suggests that the lighter features are patches of palmitic acid bilayer adjacent to patches of bare surface. Note this was only observed at this location and all other locations investigated did not show such features.

Whilst this work may explain the anomalous attraction measured between a range of surfaces rendered hydrophobic by physisorption of amphiphiles, we do not propose that this explains the long-range hydrophobic attraction under all circumstances, such as that between chemically bound monolayers[293], films[294], or solid hydrophobic surfaces[32, 281]. We note that in these studies electrolyte has little influence on the magnitude and range of the attraction. Rather in all investigations the precise nature of the surface must be considered. Thus, the nature, mechanism and the range of the true hydrophobic interaction remains unexplained[272]. Regardless, the electric attraction due to patches formed by the reorganization of amphiphiles will be important in the many cases involving surfaces rendered hydrophobic by the physisorption of surfactants that arise industrially and are also likely relevant in biology. In these cases, we can expect that surfaces of high radius of curvature allow a single patch on one surface to interact with a single patch on the other surface, giving rise to an exponential electric attraction with a decay length similar to the Debye length.

6.4 SUMMARY

I have demonstrated that a monolayer with hydrophobic properties useful for surface investigations can readily be formed by exposing metal oxide surfaces to palmitic acid in the vapour phase. The surfaces produced were characterised by contact angle measurements, ellipsometry and atomic force microscopy. The surfaces remained hydrophobic in electrolyte solution for several hours. Surface forces measured between these hydrophobic surfaces exhibited a non-DLVO exponential attraction with a decay length commensurate with the Debye length that was far greater in magnitude than the van der Waals attraction. Neither the patchy bilayer model, nor surface nanobubbles, could explain the measured forces.

However, given the mobility of the palmitic acid molecules on the surface, the interaction is well described by the interaction of a single patch of bilayered palmitic acid molecules interacting with an exposed patch of the hafnia surface. Here the attraction between the oppositely charged surfaces

is electric in nature. These patches are not present on the non-interacting surfaces and therefore must arise during approach. Such an interaction is consistent with the observed exponential nature of the attraction and the equivalence of the decay length with the Debye length of the solution. As the decay length for the interaction of a single patch is twice the decay length for the interaction of a mosaic of patches, the decay length of the interaction between such surfaces will depend on the curvature of the surfaces.

CHAPTER 7

CONCLUSIONS AND FUTURE WORK

7.1 CONCLUSIONS

Here I provide a summary of the important results, conclusions and implications of the work outlined in this thesis. I have used hafnia surfaces with or without surface modification throughout the thesis as a tool to understand the fundamentals of the surface forces between a range of surfaces. Smooth hafnia surfaces were produced using atomic layer deposition (ALD), their surface properties were characterized using various techniques, and the surfaces forces between them were measured using the atomic force microscope (AFM). The important and useful implication of the conclusions made in this thesis is that most of what I have learnt from the investigation into the hafnia surfaces is applicable to a great many other metal oxide surfaces.

The very first motivation to investigate the surface forces between smooth ALD hafnia surfaces sprang from the anomalous forces measured between smooth ALD titania surfaces[49, 53]. It was a puzzling observation that at pH far from the iep, evidence for the the van der Waals attraction was not evident in the interaction measured between the titania surfaces. The meas-

ured force remained repulsive at small separations and this could not be explained by the DLVO theory, because the theory predicts a large and measureable van der Waals attraction due to the high dielectric constant of titania. In order to ascertain whether this unexplained phenomenon is peculiar to titania or occurs rather generally, I investigated other mineral oxide surfaces. For this goal, I have chosen hafnia, which also has a high dielectric constant.

In Chapter 4, the interaction forces between smooth ALD hafnia surfaces were measured at a range of pH and salt concentrations. The forces measured between hafnia surfaces at pH values remote from the iep also lacked the short range attraction expected from the van der Waals attraction in DLVO theory. However, I demonstrated that the force curves were well described by the DLVO-R theory[203] where the effect of the surface roughness is taken into account. An important implication of this work is that surface roughness fundamentally changes the nature of the interaction at pH values remote from the iep. The effect of roughness is to reduce or remove the primary minimum in the interaction forces between particles as the influence of roughness suppresses the influence of the dispersion forces at pH values remote from the iep, due to repulsive forces arising from asperity contact. I showed that the disagreement between experimental measures of surface forces and the DLVO theory seen between a range of surfaces are due to roughness even for very smooth surfaces. This is a general result and demonstrates that even very minor levels of roughness gives rise to interactions that are different in form to what is expected from DLVO theory. This is an important result as it means that predictions based on the DLVO theory, will be quantitatively and qualitatively incorrect.

Whilst the primary minima is absent at pH values remote from the iep, interaction energy analysis based on the measured forces between hafnia surfaces revealed that strong secondary minima are present. The absence of the primary minima due to the non-zero surface roughness and the presence of the significant secondary minima, indicates that two different types of flocculation can be expected. Adjusting the pH to the iep will result in flocculation in a primary minima, causing particles to strongly adhere when they

collide, which would infer open flocs that are difficult to dewater and not easily resuspended. In contrast, at pH values remote from the iep, a sufficient increase in the ionic strength will result in flocculation in a secondary minima, allowing particles to move relative to each other and thereby form denser flocs that are more easily dewatered and readily resuspended.

In Chapter 5, I reported the influence of the adsorption of citric acid to the ALD hafnia surfaces on the interaction forces. Citrate can be used as a simple model for humic and fulvic acids which are important natural chelating agents that influence the stability and dissolution of colloids and nanoparticles in the environment. Citrate adsorption changed the surface potential of hafnia and this gave rise to a significant electric repulsion between the surfaces at all pH values of 3 and above, which prevents aggregation. I demonstrated that citric acid is a very effective stabilizer for metal oxide particles as the surface forces were always repulsive and no primary adhesion was observed, even at low citric acid concentrations.

Interaction energy analysis based on the measured forces between hafnia surfaces in the presence of citric acid, revealed that strong secondary minima are present. The results showed that nanoparticles with citrate adsorbed are stable at high ionic strengths where colloidal particles are unstable. The extreme stability of nanoparticles across a wide range of pH and ionic strengths in the presence of citric acid has been revealed. As citric acid (or humic and fulvic acids) are often present at significant concentrations in the environment, the stability of nanoparticles in the presence of citrate ions implies an easy transport of nanoparticles *in vivo*, in soils and in the aquatic environment. This conclusion in turn has important implications for the distribution of engineered nanoparticles in the environment and concerns over the impact of nanoparticles on human health. The general features observed for the hafnia-citrate system are expected to be followed by a wide range of mineral oxide surfaces with isoelectric points at near-neutral pH such as titania, zirconia, magnetite, and haematite.

In Chapter 6, I introduced a new approach for easily forming a hydrophobic monolayer on flat and spherical surfaces by exposing hafnia surfaces

and other metal oxides to palmitic acid in the vapour phase. The contact angle measurements revealed that the surfaces remained hydrophobic in electrolyte solution for several hours. A non-DLVO exponential attraction of magnitude far greater than the van der Waals attraction was observed in the surface forces measured between these hydrophobic surfaces. The decay length was commensurate with the Debye length and thus the attraction could not be explained by the patchy charge model[216, 280] which predicts a decay length of one-half the Debye length. However, given the mobility of the palmitic acid molecules on the surface, the interaction was well described by the interaction of a single patch of bilayered palmitic acid molecules interacting with a single exposed patch of the hafnia surface. This interaction may be viewed as a special case of the patchy charge model of surface interaction where the curvature of the surfaces is such that the interaction involves only one patch on each surface. It is important to note that the decay length for the interaction of a single patch is twice the decay length for the interaction of a mosaic of patches. This implies that the decay length of the interaction between such surfaces will depend on the curvature of the surfaces, as this determines the area of interaction between the surfaces. In other words, the very nature of this interaction changes with particle size. The electric attraction due to patches formed by the reorganization of amphiphiles will be important in the many cases involving surfaces rendered hydrophobic by the physisorption of surfactants that arise industrially and are also likely relevant in biology.

7.2 FUTURE WORK

Conclusions and implications drawn in each chapter in this thesis lead us to some intriguing future work. Further investigation of the roughness effect on the flocculation of colloidal particles and nanoparticles is warranted. My work has shown that the surface roughness removes or reduces the primary minima while maintaining the secondary minima for colloidal particles at high electrolyte concentration. Measurements of sedimentation, resuspen-

sion and the yield stress of colloidal systems consisting of particles with different levels of roughness will reveal if this can be practically applied to control the particle interactions and the nature of flocculation. Flocculation into a primary minima or into a secondary minima can be controlled by varying the surface roughness of the colloidal particles, the pH or the ionic strength of the solution.

The extreme stability of nanoparticles at a wide range of pH and even at high electrolyte concentrations in the presence of citric acid, predicted from the surface forces should also be tested. Similar experiments using fulvic and humic acids will be useful in understanding the interactions between particles in a range of natural environments.

The technique of atomic layer deposition (ALD) has been a remarkably useful tool to produce smooth surfaces suitable for surface forces studies in this thesis. This technique has great potential to be employed in other surface force measurement techniques such as the surface force apparatus (SFA) and in a range of other surface studies. Surfaces that have not been previously investigated can now be readily produced using ALD. For example, intrinsically hydrophobic ALD surfaces such as copper sulfide with minimal roughness will be useful for investigating the hydrophobic forces.

APPENDIX – A

In this Appendix, I include the calculations of the DLVO-R model using a Gaussian roughness distribution and of the van der Waals interactions in multilayered systems performed by Dr. Drew Parsons of School of Engineering and IT, Murdoch University, Western Australia, Australia. Note that this section uses L as the separation between two surfaces rather than x as in most of this thesis. The text is from the Ref. [201] *and the submitted journal articles in the publications list (Shinohara et al. 2017, and Eom et al. 2017) and is written by Dr. Drew Parsons.*

A.1 DLVO-R model with a Gaussian roughness distribution

The DLVO theory with roughness (DLVO-R) [203] that I have employed in this thesis consists of two chief elements. Firstly, using the probability distribution of surface heights, the noncontact (DLVO type) surface force is averaged over all the surface elements between all the statistically possible surface separations. Roughness can be included in the model in two different ways, either by incorporation of a histogram of the heights of the surface features or by assuming a Gaussian roughness distribution with the magnitude described by the rms roughness. We have employed the latter in this thesis. The roughened noncontact interaction energy $G_{nc}(L)$ at surface separation L, used to calculate surface forces, is derived from the interaction G_{smooth} between smooth surfaces by averaging over the roughness distribution,

$$G_{nc}(L) = \int dh \frac{e^{-h^2/2\sigma_m^2}}{\sigma_m\sqrt{2\pi}} G_{smooth}(L+h) \tag{A.1}$$

where σ_m is the mean rms roughness $\sigma_m = \sqrt{\sigma_1^2 + \sigma_2^2}$ averaged over the rms roughnesses σ_1 and σ_2 of each surface. We take both surfaces to have identical rms roughness σ, so $\sigma_m = \sigma\sqrt{2}$. We apply the full roughness average of Equation A.1 to the conventional smooth noncontact (DLVO) interaction. But if the smooth interaction is exponentially decaying with decay length λ (e.g. Debye length), then the roughened noncontact force may be approximately represented by

$$G_{nc}(L) \approx G_{smooth}(L) \times e^{\sigma_m^2/2\lambda^2} \tag{A.2}$$

The second element of the roughness model arises from the fact that the surface asperities start to compress each other before the separation between the average heights of the surfaces becomes zero. The asperity contact force is also averaged over all the possible surface heights considering a hemispherical asperity with low aspect ratio (height/base diameter). The contact interaction energy is determined by the reduced radius $1/R_r = 1/R_1 + 1/R_2$ of asperity tips and the reduced Young's modulus of the two surfaces, $1/E_r = 1/E_1 + 1/E_2$ (taking Poisson ratios of the materials to be 1). When the surface height distribution is taken to be Gaussian with mean rms σ_m then the contact force (normalised to the radius r of the colloidal probe) may be approximated by

$$f_{contact}(L)/r \approx \left(\frac{E_r 2\sqrt{2}}{5}\right) \frac{\sigma_m^4}{\sqrt{R_r}} \frac{e^{-L^2/2\sigma_m^2}}{L^2\sqrt{L}} \tag{A.3}$$

This expression is an approximation. We use the exact analytical expression which involves Bessel functions. The total force sums both components, the roughened noncontact force derived from Equation A.1 and the contact force of Equation A.3. In practice the compliance is matched to the asperity contact force and in this manner the separation of the surfaces at contact is set relative to the average position of the interface.

A.2 Multilayered van der Waals interactions

It is convenient to model the forces measured by AFM (sphere-plane geometry) using the proximity force approximation (Derjaguin approximation) based on the interaction free energy $F_{vdW}(L)$ between two planes. The van der Waals interaction energy between two such planar multilayer surfaces may be described via a distance-dependent Hamaker coefficient $A(L)$,

$$F_{vdW}(L) = \frac{-A(L)}{12\pi L^2} \tag{A.4}$$

The Hamaker coefficient is evaluated in the usual way via a dielectric function $\varepsilon_s(i\omega)$ for each surface[49, 83]

$$A(L) = \frac{2kT}{3}\sum\int dx\, x\{ln[1-\bar{\Delta}_{mL}(i\omega_n)\bar{\Delta}_{mR}(i\omega_n)e^{-x}] + ln[1-\Delta_{mL}(i\omega_n)\Delta_{mR}(i\omega_n)e^{-x}]\} \tag{A.5}$$

where ω_n are the Matsubara frequencies $\omega_n = 2\pi kTn/\hbar$. The prime next to the summation symbol indicates that n=0 is taken with a factor ½. $r_n = 2L\omega_n\sqrt{\varepsilon_m(i\omega_n)}\bar{\Delta}$ and $\Delta$are dielectric and diamagnetic reflection coefficients:

$$\bar{\Delta}_{jk}(i\omega) = \frac{s_j\varepsilon_j - s_j\varepsilon_k}{s_j\varepsilon_j + s_j\varepsilon_k} \tag{A.6}$$

and

$$\Delta_{jk}(i\omega) = \frac{s_j\mu_j - s_j\mu_k}{s_j\mu_j + s_j\mu_k} \tag{A.7}$$

We take the materials to be nonmagnetic such that μ_i=1 for each layer. s_i is a retardation coefficient, $s_j(i\omega) = \sqrt{p^2 - 1 + \varepsilon_j(i\omega)/\varepsilon_m(i\omega)}$ where $p = xc/2\omega L\sqrt{(\varepsilon_m(i\omega))}$. The dielectric functions ε_i in Equation A.6 may be thought of as an effective dielectric function describing the combined response of all layers. But more precisely it refers to the dielectric function of each layer in turn, in which case the reflection coefficients in Equation A.5 are determined recursively from neighbouring layers,

$$\Delta_{\mathrm{mL}} = \frac{\Delta_{m,1}+\Delta_{1,L}e^{-\mathrm{x}s_1 l_1/\mathrm{pL}}}{1+\Delta_{m,1}\Delta_{1,L}e^{-\mathrm{x}s_1 l_1/\mathrm{pL}}} \tag{A.8}$$

and

$$\Delta_{\mathrm{jL}} = \frac{\Delta_{j,j+1}+\Delta_{j+1,L}e^{-\mathrm{x}s_{j+1} l_{j+1}/\mathrm{pL}}}{1+\Delta_{j,j+1}\Delta_{j+1,L}e^{-\mathrm{x}s_{j+1} l_{j+1}/\mathrm{pL}}} \tag{A.9}$$

Because of the appearance of separation distance L in these recursive reflection coefficients, the Hamaker coefficient becomes distance-dependent even in the nonretard limit $c\to\infty$.

A.2.1 *Justification for use of the nonretarded Hamaker constant (Chapter 4)*

The van der Waals interaction of the hafnia system was modelled using a standard Hamaker-style description, for which the interaction free energy per unit area between two flat surfaces is

$$G_{Ham}(L) = -\frac{A}{12\pi L^2} \tag{A.10}$$

Here A is the nonretarded Hamaker constant, which for hafnia-water-hafnia is 56 zJ.

More generally A is not a constant, but rather a distance-dependent coefficient $A(L)$. Distance dependence arises because of the finite speed of light (retardation), which causes $A(L)$ to fall in value. But it also arises in multilayered systems, even under nonretarded conditions[83]. At small separations the Hamaker coefficient follows that of the outermost layer (hafnia). At larger distances the influence of the underlaying substrate is felt.[49]

In Figure A.1 we show the distance-dependent Hamaker coefficient, comparing the retarded Hamaker coefficient of pure hafnia against the retarded and nonretarded Hamaker coefficients for our layered system (12.7 nm hafnia on silicon substrate, with intervening layers of silica (2 nm) and titania (38 nm). The retarded Hamaker coefficient of pure hafnia falls relatively quickly, attenuating to almost half its nonretarded value within a sep-

aration of 100 nm. By contrast the retarded Hamaker coefficient of the multilayered system attenuates much more slowly, losing only 15% of its nonretarded value at a separation of 100 nm. At the separations measured in this work (5-50 nm), the retarded multilayer Hamaker coefficient falls from 56 to 52 zJ, losing only 7% of its magnitude. For this reason it is reasonable to use the nonretarded Hamaker constant in this system to describe the van der Waals interaction.

The reason for the diminished retardation effect in the multilayer system can be understood from the nonretarded Hamaker coefficient, which actually increases with separation. At larger separations, the van der Waals interaction of the underlying substrate, silicon, starts to dominate. The nonretarded Hamaker coefficient rises from the value of 56 zJ for hafnia towards the value of 95 zJ for silicon.

It follows that the Hamaker coefficient may remain closer to the value of the nonretarded constant (i.e. decay more slowly) if the thickness of the hafnia layer (and titania) is made thinner.

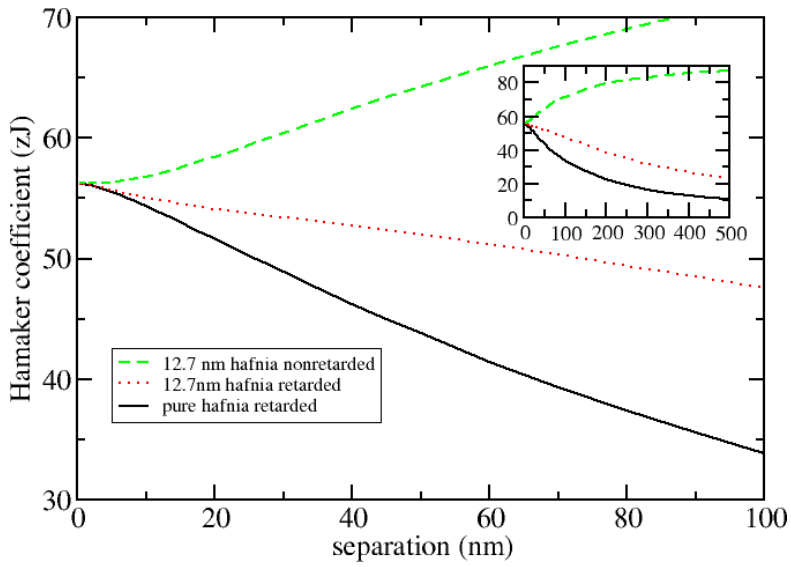

Figure A.1. Distance-dependence Hamaker coefficient of hafnia surfaces interacting across water., We compare the retarded Hamkaer coefficient of pure hafnia (solid black) against the retarded (dotted red) and nonretarded (dashed green) Hamaker coefficients of the multilayer system (12.7 nm hafnia, 38 nm titania, 2 nm silica on silicon substrate).

A.2.2 *Citric acid/hafnia system*

The van der Waals interaction for the citric acid/hafnia system in Chapter 5 was calculated using a "thin-Rayleigh" multilayer model. We assumed 0.25 mg/m² of citric acid and the same volume density of citric acid as "thin-CM". Here the composite dielectric of the citric layer is estimated from the Rayleigh mixing formula using the volume fraction p of citric acid,

$$\frac{\varepsilon_{comp}-\varepsilon_b}{\varepsilon_{comp}+2\varepsilon_b} = p\,\frac{\varepsilon_s-\varepsilon_b}{\varepsilon_s+2\varepsilon_b} \tag{A.11}$$

where ε_{comp} = composite dielectric function, ε_b = dielectric function of the background (water), ε_s = dielectric function of the solute (citric acid without water). The latter was estimated by the Clausius-Mossotti formula,

$$\frac{\varepsilon_s-1}{\varepsilon_s+2} = \frac{4\pi}{3}\rho\alpha \tag{A.12}$$

using the density of citric acid ϱ= 0.567 g/cm³ within the citric adsorption layer (from citric surface excess of 0.25 mg/m² within a layer 0.45 nm deep). The polarisability α was represented using the electronic polarisability of diprotonated citrate H_2X^-. We estimated the volume fraction p=0.33 in the Rayleigh formula by taking the ratio of the volume density in the layer relative to the volume density 1.67 g/cm³ of solid citric acid.

A.2.3 *Palmitic acid/hafnia system*

The distance-dependant Hamaker coefficient (retarded and nonretarded) for the palmitic acid coated hafnia surface is shown in Figure A.2 (the dielectric function of palmitic acid is presented using that of hexadecane). I used the retarded Hamaker coefficient in Chapter 6. Nonretarded Hamaker constants for each layer (pure solid – water – pure solid) are also shown for comparison. At short range below 10 nm the Hamaker coefficient is small, due to the outer palmitic acid layer. It rises to the value of hafnia at mid-range 10-100 nm. At large separations greater than 200 nm the Hamaker coefficient is controlled by the underlying silicon substrate, and is attenuated by retardation such

that the value of the retarded Hamaker coefficient never exceeds that of pure hafnia.

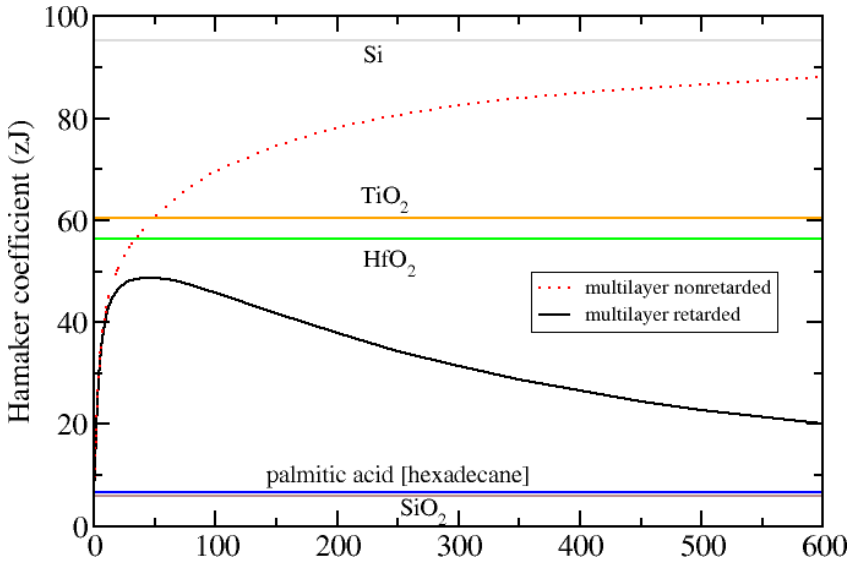

Figure A.2: Distance-dependent Hamaker coefficient for the multilayered palmitic acid coated hafnia surface. Both retarded and nonretarded Hamaker coefficients are shown, as well as the nonretarded Hamakers constants (solid-water-solid) of each layer.

APPENDIX – B

B.1 DLVO fitting, including the influence of surface roughness

In this appendix, enlarged figures of Figures 4.9 and 4.10 from Chapter 4 are presented (See § 4.2.5). The DLVO theory extended to include hydration and roughness fitted against experimental force data between two hafnia surfaces in 0.01 M and in 0.001 M NaCl at a range of pH. Three roughness values of 0.54 nm and 0.47 nm(AFM), 0.72 nm (XRR), and 1.2 nm (Best fit) for the flat surface were used. All the data were fitted with a hydration force with amplitude of 20 N/m and decay length of 0.3 nm, Young's Modulus of 57 GPa, and asperity tip curvature R = 4 nm.

See Table 4-1 in chapter 4 for fitting parameters used in this force curve fitting using DLVO-R.

0.01 M		
pH 2.8		
0.54 nm and 0.47 nm (AFM)	0.72 nm (XRR)	1.20 nm (Best fit)

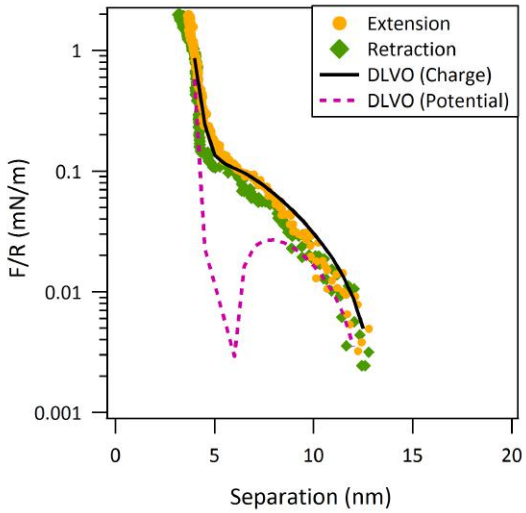

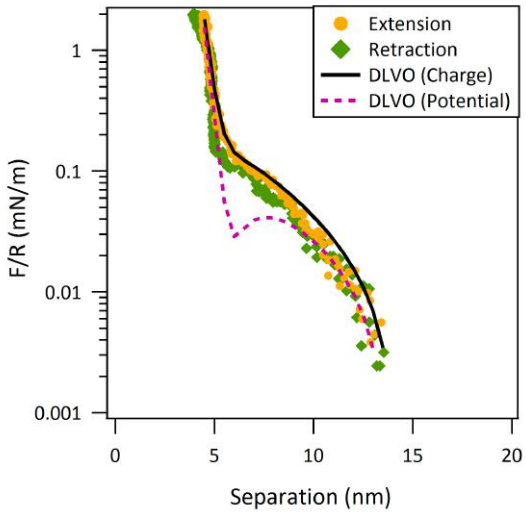

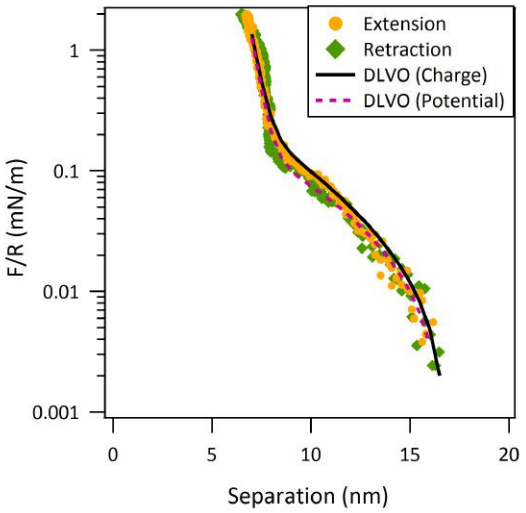

0.01 M		
pH 4.8		
0.54 nm and 0.47 nm (AFM)	0.72 nm (XRR)	1.20 nm (Best fit)

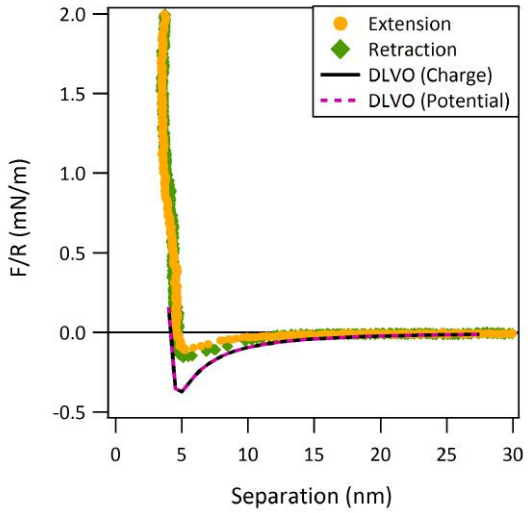

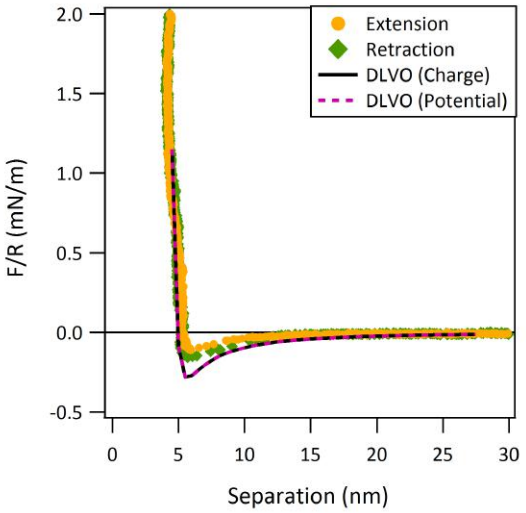

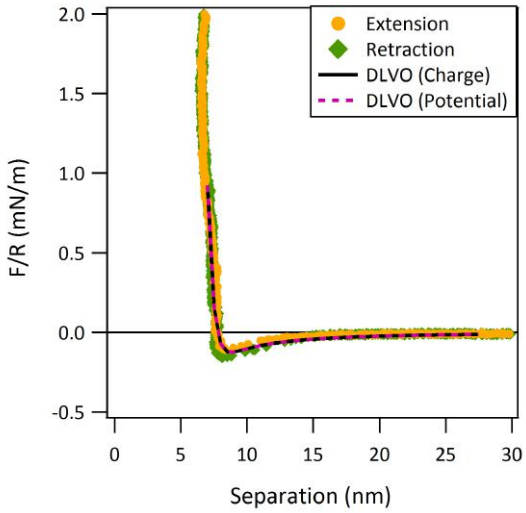

0.01 M		
pH 5.3		
0.54 nm and 0.47 nm (AFM)	0.72 nm (XRR)	1.20 nm (Best fit)

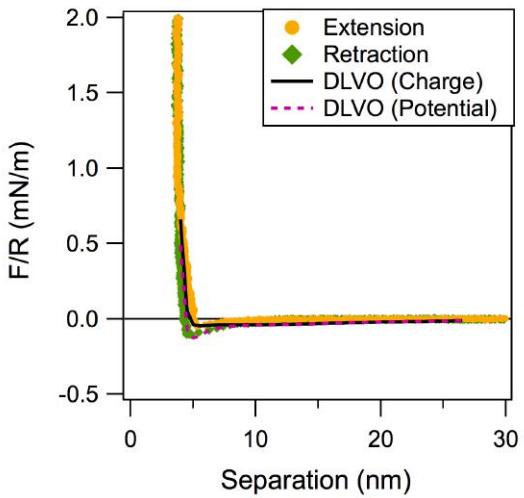

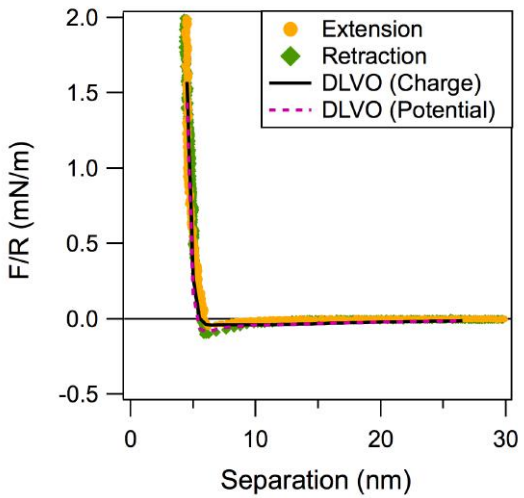

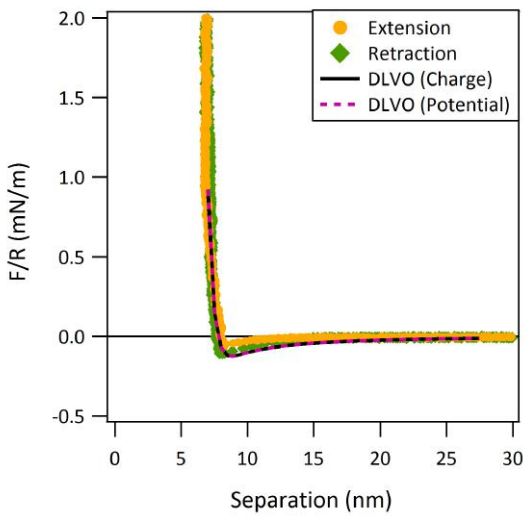

0.01 M		
pH 7.1		
0.54 nm and 0.47 nm (AFM)	0.72 nm (XRR)	1.20 nm (Best fit)

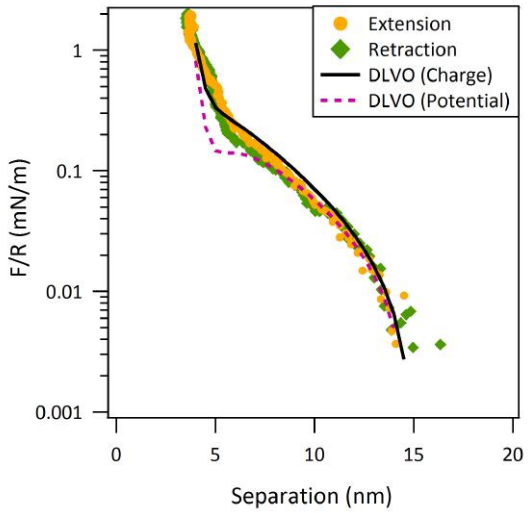

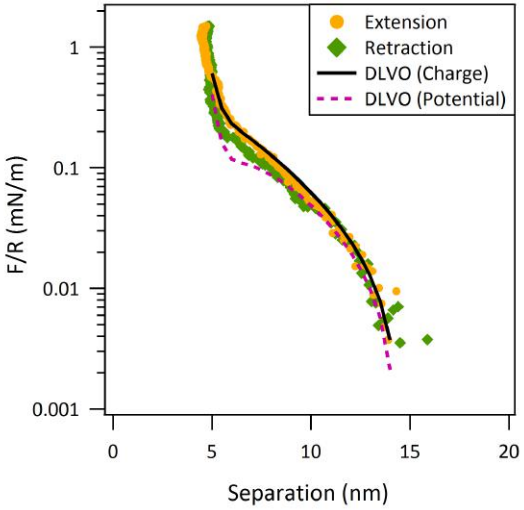

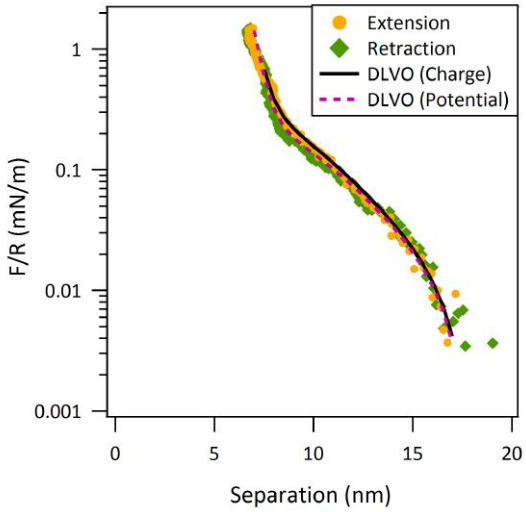

0.01 M		
pH 9.3		
0.54 nm and 0.47 nm (AFM)	0.72 nm (XRR)	1.20 nm (Best fit)

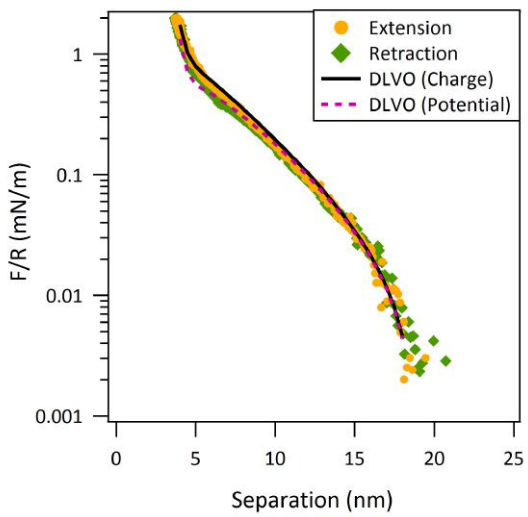

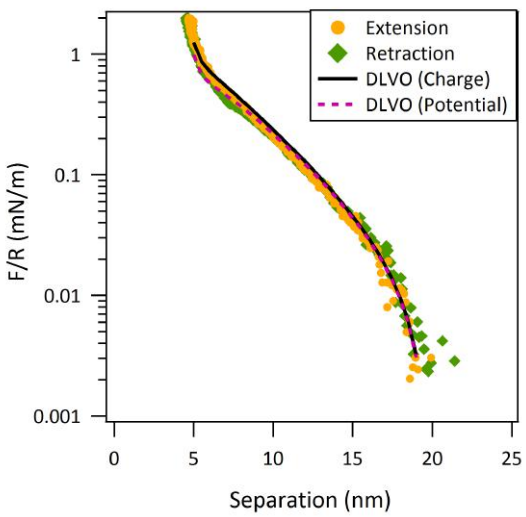

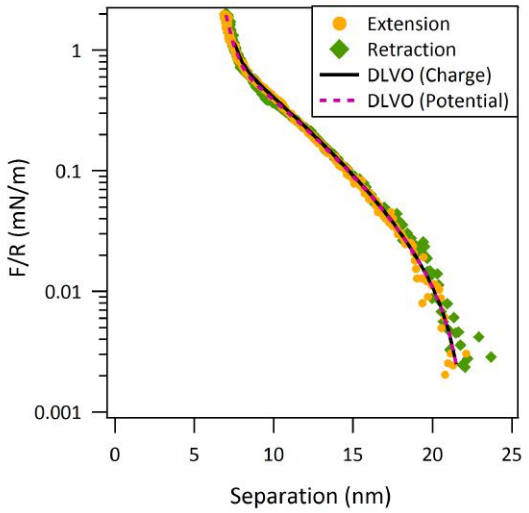

0.001 M		
pH 2.6		
0.54 nm and 0.47 nm (AFM)	0.72 nm (XRR)	1.20 nm (Best fit)

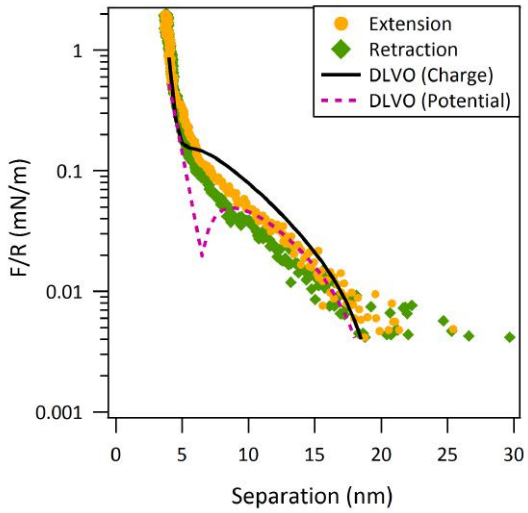

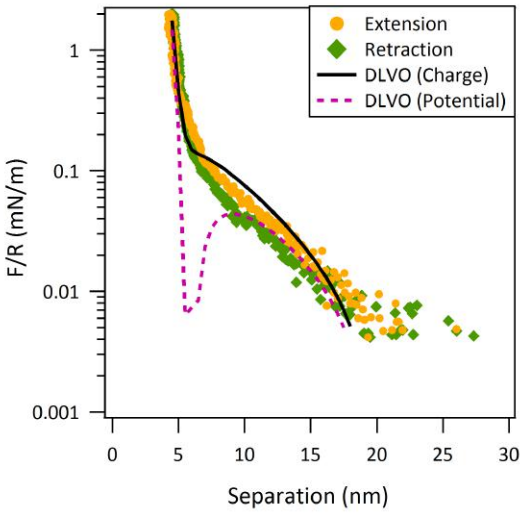

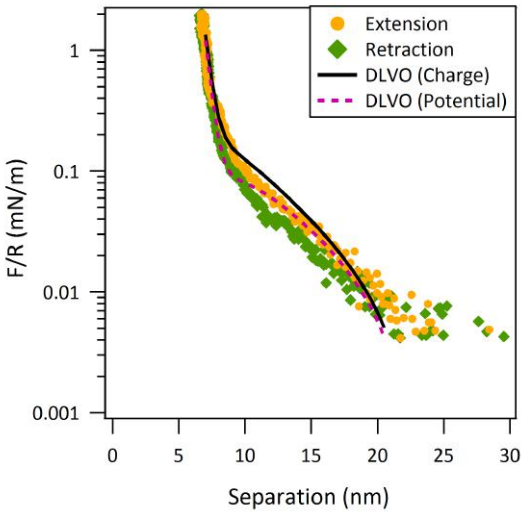

0.001 M		
pH 4.8		
0.54 nm and 0.47 nm (AFM)	0.72 nm (XRR)	1.20 nm (Best fit)

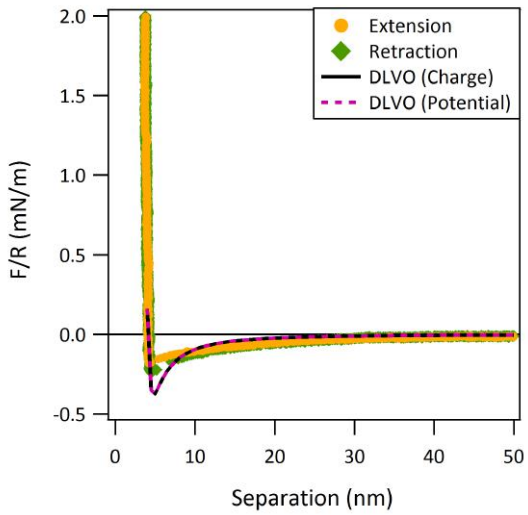

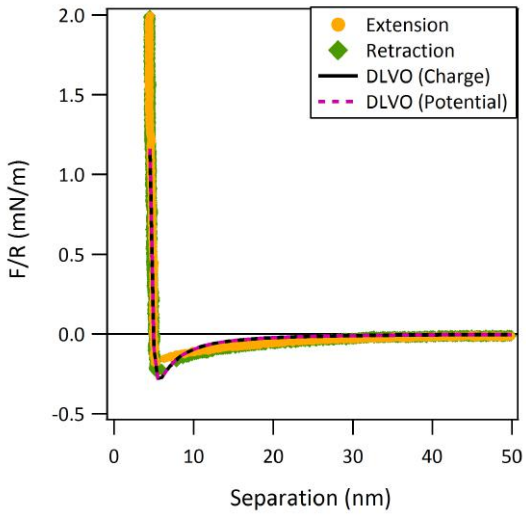

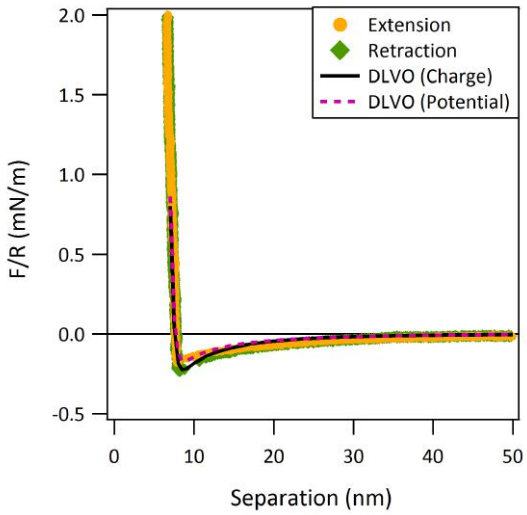

0.001 M		
pH 5.0		
0.54 nm and 0.47 nm (AFM)	0.72 nm (XRR)	1.20 nm (Best fit)

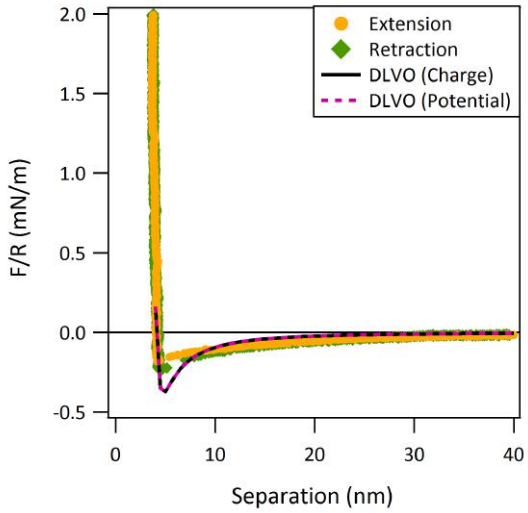

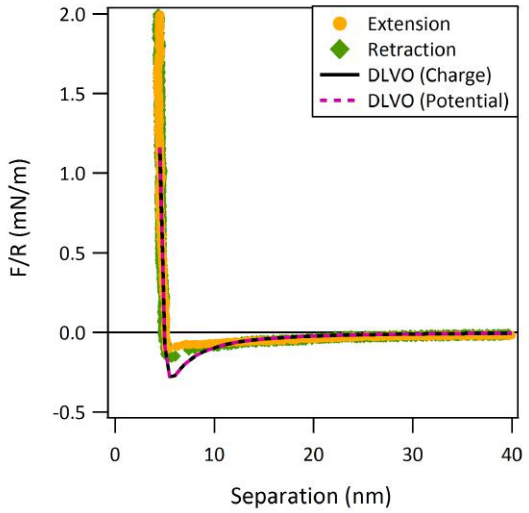

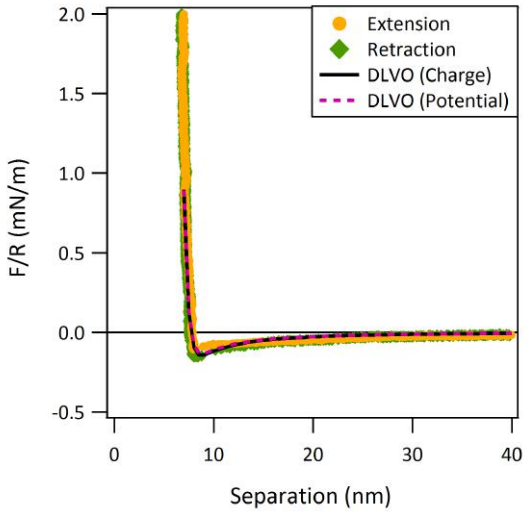

0.001 M		
pH 7.2		
0.54 nm and 0.47 nm (AFM)	0.72 nm (XRR)	1.20 nm (Best fit)

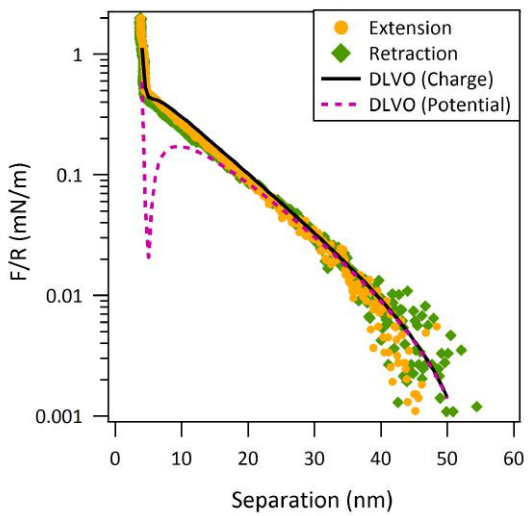

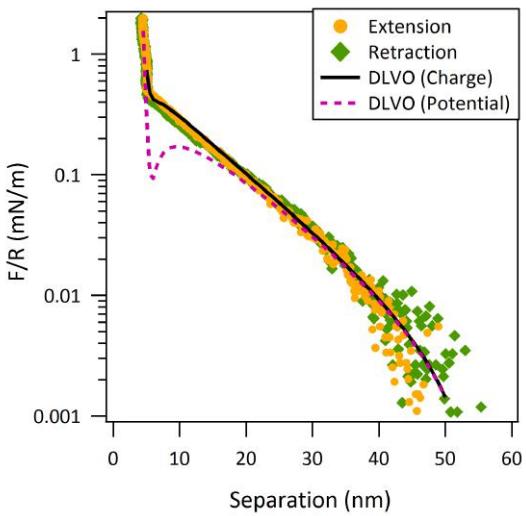

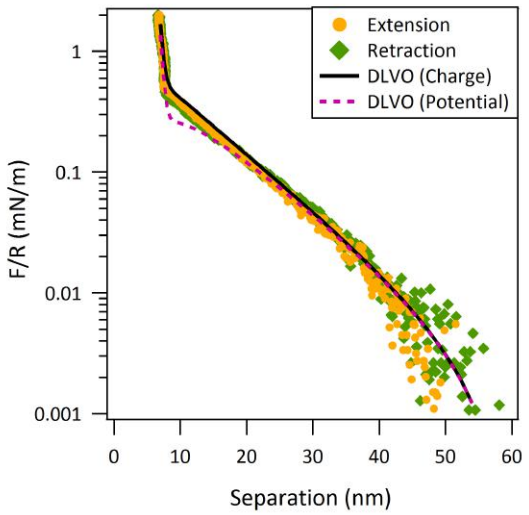

0.001 M		
pH 9.7		
0.54 nm and 0.47 nm (AFM)	0.72 nm (XRR)	1.20 nm (Best fit)

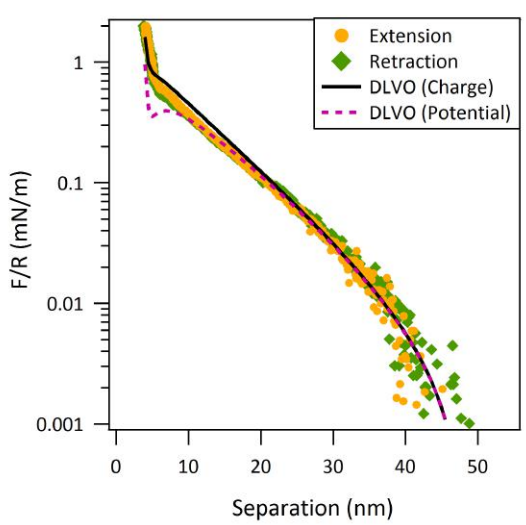

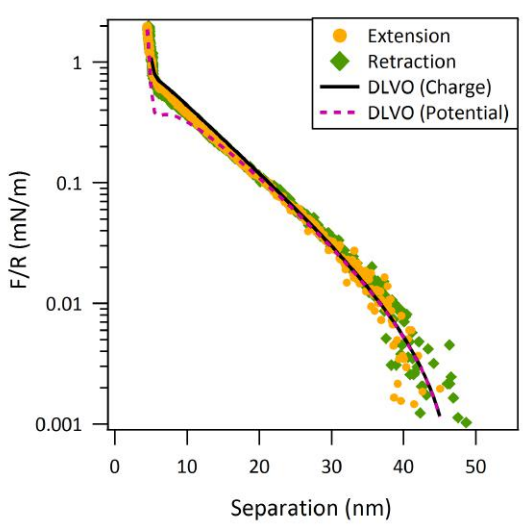

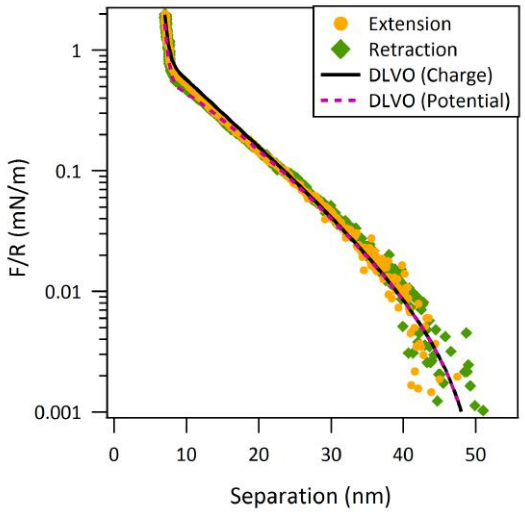

APPENDIX – C

In this appendix, I give a short description of an additional investigation done in conjunction with the work presented in Chapter 6.

C.1 Deposition of disodium sebacate monolayer on PA-hafnia

After successfully producing a monolayer of palmitic acid on hafnia surfaces, I tried to deposit a monolayer of disodium sebacate ($C_{10}H_{16}Na_2O_4$) on the hydrophobic PA-hafnia surface via self assembly to investigate its effect on the contact angle and the surface forces. A droplet of disodium sebacate solution was placed on the PA-hafnia surface and was gradually heated in an oven at 80 °C for 25 min. The surface was taken out and was washed with copious amount of purified water. The area where the diacid droplet was placed became very hydrophilic, being completely wetted by water, whilst the remaining area of the PA-hafnia surface remained hydrophobic. However, it was observed that the hydrophilicity of the area decreased after a quick washing with distilled ethanol. The thickness of the diacid layer was too thin to be measured using the Ellipsometry. It was apparent that a monolayer was deposited on the PA-hafnia surface as the wetting property changed substantially.

The contact angle of pH adjusted 0.001 M NaCl on the diacid treated region was measured. The measured contact angles did not show distinct dependency on the pH of the solution. The surface forces measured between diacid treated surfaces showed a similar trend to the forces measured between the hafnia surfaces without any surface modification, except that there were adhesion forces observed at pH 5 when the diacid layer was present.

Further experiments showed that the zeta potential and the surface force measurements were not reproducible, probably due to contamination. Because of the lack of reproducibility these measurements were not pursued or analysed further.

APPENDIX – D

In this appendix, I give the DLVO fit against the surface force measured between ALD hafnia surfaces in NaCl electrolyte solution taking account of hydration force (See § 4.2.4). *Unlike Figure 4.8 where hydration prefactor of 20 N/m was used, here hydration prefactor was increased until reasonable fits were achieved.*

D.1 DLVO fitting including Hydration force

The surface forces measured at high pH were fitted using DLVO including hydration force. The results below show that the hydration prefactor had to be increased to approximately 1000 N/m in order to achieve reasonable fits. Therefore we rule out the possibility that hydration force is responsible for the anormalous repulsion measured between ALD hafnia surfaces at short separations.

NaCl concentration	0.01 M
pH 7.1	
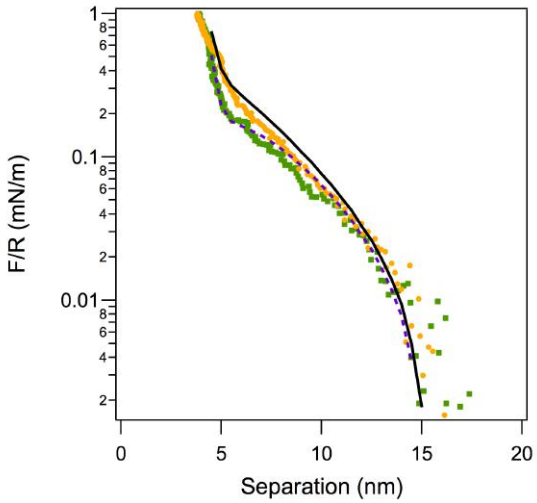	Hydration prefactor: 1000 N/m Surface potential: -34.0 mV Debye length: 3.7 nm

NaCl concentration	0.01 M
pH 9.3	
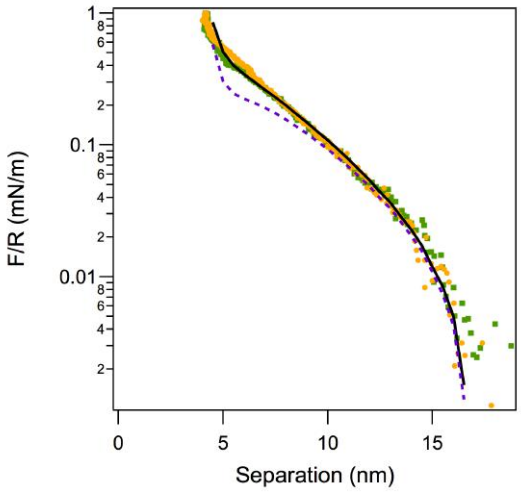	Hydration prefactor: 1000 N/m Surface potential: -36.3 mV Debye length: 3.8 nm

NaCl concentration	0.001 M
pH 7.2	
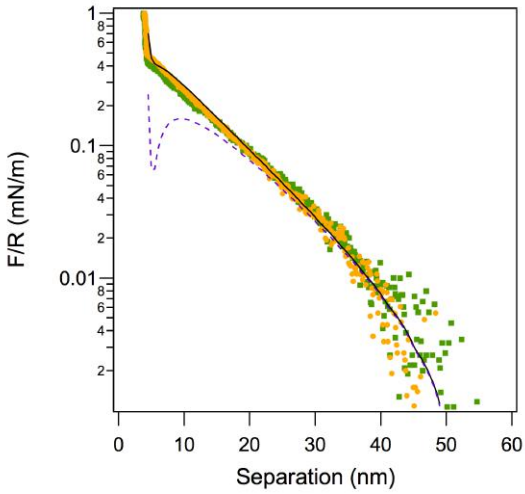	Hydration prefactor: 1000 N/m Surface potential: -31.0 mV Debye length: 9.1 nm

NaCl concentration	0.001 M
pH 9.7	
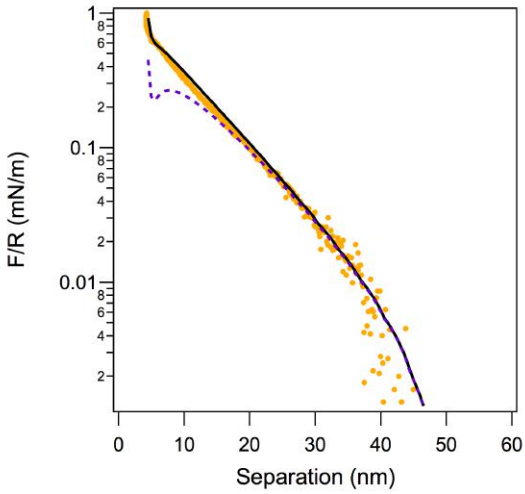	Hydration prefactor: 1000 N/m Surface potential: -38.6 mV Debye length: 8.5 nm

BIBLIOGRAPHY

[1] Hughes, R., An Introduction to Colloids. In *Colloid Science Principles, methods and applications*. 2nd ed.; Cosgrove, T., Ed. John Wiley & Sons: Bristol, UK, 2010.

[2] Berg, J. C., *An introduction to interfaces and colloids: The bridge to nanoscience.* World Scientific Publishing London 2010.

[3] Tan, K. H., *Principles of soil chemistry.* 4th ed.; CRC Press London 2011.

[4] Pashley, R. M.; Karaman, M. E., *Applied Colloid and Surface Chemistry*. John Wiley & Sons, Ltd.: West Sussex, England, 2004.

[5] Dickinson, E., *An Introduction to Food Colloids*. Oxford University Press: Oxford, England, 1992.

[6] Dickinson, E.; McClements, D. J., *Advances in Food Colloids.* Blackie Academic & Professional London 1995.

[7] Raney, K. H.; Benson, H. L., The Effect of Polar Soil Components on the Phase Inversion Temperature and Optimum Detergency Conditions. *J. Am. Oil Chem. Soc.* **1990,** *67* (11), 722-729.

[8] Lim, J. C.; Miller, C. A., Dynamic Behavior and Detergency in Systems Containing Nonionic Surfactants and Mixtures of Polar and Nonpolar Oils. *Langmuir* **1991,** *7* (10), 2021-2027.

[9] Carroll, B. J., Physical Aspects of Detergency. *Colloids Surf., A* **1993,** *74* (2-3), 131-167.

[10] Worch, E., *Adsorption Technology in Water Treatment: Fundamentals, Processes, and Modeling*. Hubert & Co. GmbH & Co. KG, Gottingen Germany, 2012; p 1-332.

[11] Ali, I.; Gupta, V. K., Advances in water treatment by adsorption technology. *Nat. Protoc.* **2006,** *1* (6), 2661-2667.

[12] Briant, J.; Denis, J.; Parc, G., *Rheological properties of lubricatns.* Editions Technip: France 1989.

[13] Blackman, G. S.; Mate, C. M.; Philpott, M. R., Atomic Force Microscope Studies of Lubricant Films on Solid-Surfaces. *Vacuum* **1990,** *41* (4-6), 1283-1286.

[14] Braithwaite, E. R., *Solid Lubricants and Surfaces.* Pergamon Press Ltd. New York, 1964.

[15] Schramm, L. L., *Surfactants: Fundamentals and Applications in the Petroleum Industry.* Cambridge University Press Cambridge, UK 2000.

[16] Nguyen, A. V.; Schulze, H. J., *Colloidal science of flotatio.* Marcel Dekker, Inc New York 2004.

[17] Laskowski, J. S.; Ralston, J., *Colloid Chemistry in mineral processing*. Elsvier New York 1992.

[18] Mishra, B.; Patel, B. B.; Tiwari, S., Colloidal nanocarriers: a review on formulation technology, types and applications toward targeted drug delivery. *Nanomed. Nanotech. Biol. Med.* **2010,** *6* (1), 9-24.

[19] Lawrence, M. J.; Rees, G. D., Microemulsion-based media as novel drug delivery systems. *Adv. Drug Deliv. Rev.* **2012,** *64*, 175-193.

[20] Derjaguin, B. V.; Landau, L., Theory of the Stability of Strongly Charged Lyophobic Sols and of the Adhesion of Strongly Charged Particles in Solutions of Electrolytes. *Acta. Phys. Chim. URSS* **1941,** *14*, 633.

[21] Verwey, E. J. W.; Overbeek, J. T. G., *Theory of the Stability of Lyophobic Colloids*. Elsevier Publishing Company: 1948.

[22] Tabor, D.; Winterton, R. H. S., Surface Forces - Direct Measurement of Normal and Retarded Van Der Waals Forces. *Nature* **1968,** *219* (5159), 1120-1121.

[23] Israelachvili, J., et al., Recent Advances in the Surface Forces Apparatus (SFA) Technique. *Rep. Prog. Phys.* **2010,** *73* (3), 036601.

[24] Binnig, G.; Quate, C. F.; Gerber, C., Atomic Force Microscope. *Phys. Rev. Lett.* **1986,** *56*, 930.

[25] Butt, H. J.; Cappella, B.; Kappl, M., Force Measurements with the Atomic Force Microscope: Technique, Interpretation and Applications. *Surf. Sci. Rep.* **2005,** *59*, 1-152.

[26] Biggs, S.; Mulvaney, P., Measurement of the Forces between Gold Surfaces in Water by Atomic-Force Microscopy. *J. Chem. Phys.* **1994,** *100* (11), 8501-8505.

[27] Giesbers, M.; Kleijn, J. M.; Stuart, M. A. C., The Electrical Double Layer on Gold Probed by Electrokinetic and Surface Force Measurements. *J. Colloid Interface Sci.* **2002,** *248* (1), 88-95.

[28] Grabbe, A.; Horn, R. G., Double-Layer and Hydration Forces Measured between Silica Sheets Subjected to Various Surface Treatments. *J. Colloid Interface Sci.* **1993,** *157* (2), 375-383.

[29] Ducker, W. A.; Senden, T. J.; Pashley, R. M., Measurement of Forces in Liquids Using a Force Microscope. *Langmuir* **1992,** *8* (7), 1831-1836.

[30] Toikka, G.; Hayes, R. A.; Ralston, J., Surface Forces between Spherical ZnS Particles in Aqueous Electrolyte. *Langmuir* **1996,** *12* (16), 3783-3788.

[31] Muster, T. H.; Toikka, G.; Hayes, R. A.; Prestidge, C. A.; Ralston, J., Interactions between zinc sulphide particles under flotation-related conditions. *Colloids. Surf., A* **1996,** *106* (2-3), 203-211.

[32] Meagher, L.; Craig, V. S. J., Effect of Dissolved Gas and Salt on the Hydrophobic Force between Polypropylene Surfaces. *Langmuir* **1994,** *10*, 2736-2742.

[33] Vinogradova, O. I.; Yakubov, G. E.; Butt, H. J., Forces Between Polystyrene Surfaces in Water-Electrolyte Solutions: Long-Range Attraction of Two Types? *J. Chem. Phys.* **2001,** *114* (18), 8124-8131.

[34] Li, Y. Q.; Tao, N. J.; Pan, J.; Garcia, A. A.; Lindsay, S. M., Direct Measurement of Interaction Forces between Colloidal Particles Using the Scanning Force Microscope. *Langmuir* **1993,** *9* (3), 637-641.

[35] Tonck, A.; Georges, J. M.; Loubet, J. L., Measurements of Intermolecular Forces and the Rheology of Dodecane between Alumina Surfaces. *J. Colloid Interface Sci.* **1988,** *126* (1), 150-163.

[36] Polat, M.; Sato, K.; Nagaoka, T.; Watari, K., Effect of pH and Hydration on the Normal and Lateral Interaction Forces between Alumina Surfaces. *J. Colloid Interface Sci.* **2006,** *304* (2), 378-387.

[37] Prica, M.; Biggs, S.; Grieser, F.; Healy, T. W., Effect of Calcination Temperature on the Electrokinetic Properties of Colloidal Zirconia. *Colloids Surf., A* **1996,** *119* (2-3), 205-213.

[38] Sun, J.; Gao, L.; Bergstrom, L.; Iwasa, M., Direct force measurements between zirconia surfaces: Influence of the concentration of polyacrylic acid, pH, and molecular weight. *Characterization and Control of Interfaces for High Quality Advanced Materials* **2005,** *146*, 35-41.

[39] Pedersen, H. G.; Bergstrom, L., Forces measured between zirconia surfaces in poly(acrylic acid) solutions. *J. Am. Ceram. Soc.* **1999,** *82* (5), 1137-1145.

[40] Browne, C.; Tabor, R. F.; Grieser, F.; Dagastine, R. R., Direct AFM force measurements between air bubbles in aqueous monodisperse sodium poly(styrene sulfonate) solutions. *J. Colloid Interface Sci.* **2015,** *451*, 69-77.

[41] Dagastine, R. R.; Stevens, G. W.; Chan, D. Y. C.; Grieser, F., Forces between two oil drops in aqueous solution measured by AFM. *J. Colloid Interface Sci.* **2004,** *273* (1), 339-342.

[42] Lockie, H. J.; Manica, R.; Stevens, G. W.; Grieser, F.; Chan, D. Y. C.; Dagastine, R. R., Precision AFM Measurements of Dynamic Interactions between Deformable Drops in Aqueous Surfactant and Surfactant-Free Solutions. *Langmuir* **2011,** *27* (6), 2676-2685.

[43] Walsh, R. B.; Howard, S. C.; Nelson, A.; Skinner, W. M.; Liu, G. M.; Craig, V. S. J., Model Surfaces Produced by Atomic Layer Deposition. *Chem. Lett.* **2012,** *41* (10), 1247-1249.

[44] Miikkulainen, V.; Leskela, M.; Ritala, M.; Puurunen, R. L., Crystallinity of Inorganic Films Grown by Atomic Layer Deposition: Overview and General Trends. *J. Appl. Phys.* **2013,** *113* (2), 021201.

[45] Leskela, M.; Ritala, M., Atomic layer deposition (ALD): from precursors to thin film structures. *Thin Solid Films* **2002,** *409* (1), 138-146.

[46] George, S. M., Atomic Layer Deposition: An Overview. *Chem. Rev.* **2010,** *110* (1), 111-131.

[47] Dasgupta, N. P.; Lee, H. B. R.; Bent, S. F.; Weiss, P. S., Recent Advances in Atomic Layer Deposition. *Chem. Mater.* **2016,** *28* (7), 1943-1947.

[48] Hausmann, D. M.; Gordon, R. G., Surface Morphology and Crystallinity Control in the Atomic Layer Deposition (ALD) of Hafnium and Zirconium Oxide Thin Films. *J. Cryst. Growth* **2003,** *249* (1-2), 251-261.

[49] Walsh, R. B.; Nelson, A.; Skinner, W. M.; Parsons, D.; Craig, V. S. J., Direct Measurement of van der Waals and Diffuse Double-Layer Forces between Titanium Dioxide Surfaces Produced by Atomic Layer Deposition. *J. Phys. Chem. C* **2012,** *116* (14), 7838-7847.

[50] Barnes, G. T.; Gentle, I. R., *Interfacial science: an introduction* 2nd ed.; Oxford University Press New York 2011.

[51] Bostrom, M.; Williams, D. R. M.; Ninham, B. W., Specific Ion Effects: Why DLVO Theory Fails for Biology and Colloid Systems. *Phys. Rev. Lett.* **2001,** *87* (16), 168103.

[52] Grasso, D.; Subramaniam, K.; Butkus, M.; Strevett, K.; Bergendahl, J., A review of non-DLVO interactions in environmental colloidal systems. *Rev. Environ. Sci. Bio.* **2002,** *1*, 17-38.

[53] Walsh, R. B.; Evans, D.; Craig, V. S. J., Surface Force Measurements between Titanium Dioxide Surfaces Prepared by Atomic Layer Deposition in Electrolyte Solutions Reveal Non-DLVO Interactions: Influence of Water and Argon Plasma Cleaning. *Langmuir* **2014,** *30* (8), 2093-2100.

[54] Kerber, A.; Cartier, E. A., Reliability Challenges for CMOS Technology Qualifications With Hafnium Oxide/Titanium Nitride Gate Stacks. *IEEE Trans. Device Mater. Rel.* **2009,** *9* (2), 147-162.

[55] Muller, J., et al., Ferroelectric Hafnium Oxide: A CMOS-compatible and highly scalable approach to future ferroelectric memories. *2013 Ieee International Electron Devices Meeting (Iedm)* **2013**.

[56] Lee, B. H.; Kang, L. G.; Nieh, R.; Qi, W. J.; Lee, J. C., Thermal stability and electrical characteristics of ultrathin hafnium oxide gate dielectric reoxidized with rapid thermal annealing. *Appl. Phys. Lett.* **2000,** *76* (14), 1926-1928.

[57] Kang, L.; Lee, B. H.; Qi, W. J.; Jeon, Y.; Nieh, R.; Gopalan, S.; Onishi, K.; Lee, J. C., Electrical characteristics of highly reliable ultrathin hafnium oxide gate dielectric. *Ieee Electron Device Letters* **2000,** *21* (4), 181-183.

[58] Buljan, S. T.; Wayne, S. F., Wear and Design of Ceramic Cutting-Tool Materials. *Wear* **1989,** *133* (2), 309-321.

[59] Benfer, S.; Popp, U.; Richter, H.; Siewert, C.; Tomandl, G., Development and characterization of ceramic nanofiltration membranes. *Sep. Purif. Technol.* **2001,** *22-3* (1-3), 231-237.

[60] Blanc, P.; Larbot, A.; Palmeri, J.; Lopez, M.; Cot, L., Hafnia ceramic nanofiltration membranes. Part I: Preparation and characterization. *J. Memb. Sci.* **1998,** *149* (2), 151-161.

[61] Zhu, D. M.; Miller, R. A., Sintering and creep behavior of plasma-sprayed zirconia- and hafnia-based thermal barrier coatings. *Surf. Coat. Technol.* **1998,** *108* (1-3), 114-120.

[62] Bergström, L., Colloidal processing of ceramics. In *Handbook of Applied Surface and Colloid Chemistry*, 1 ed.; Holmberg, K., Ed. John Wiley & Sons, Ltd 2002.

[63] Wang, J.; Li, H. P.; Stevens, R., Hafnia and Hafnia-Toughened Ceramics. *J. Mater. Sci.* **1992,** *27* (20), 5397-5430.

[64] Israelachvili, J., *Intermolecular and Surface Forces* 3rd ed.; Elsevier San Diego, USA, 2011.

[65] Myers, D., *Surfaces, Interfaces, and Colloids - Principles and Applications* 2nd ed.; John Wiley & Sons, Inc. : NY, USA 1999.

[66] Hiemenz, P. C.; Rajagopalan, R., *Principles of Colloid and Surface Chemistry* 3rd ed.; Marcel Dekker New York 1997.

[67] Parsegian, V. A., *Van der Waals Forces: A Handbook for Biologists, Chemists, Engineers, and Physicists* Cambridge University Press: New York, USA, 2006.

[68] Butt, H. J.; Kappl, M., *Surface and Interfacial Forces*. Wiley-VCH: Darmstadt, Germany, 2010.

[69] Tabor, R. F.; Grieser, F.; Dagastine, R. R.; Chan, D. Y. C., The Hydrophobic Force: Measurements and Methods. *Phys. Chem. Chem. Phys.* **2014,** *16* (34), 18065-18075.

[70] Meyer, E. E.; Rosenberg, K. J.; Israelachvili, J., Recent Progress in Understanding Hydrophobic Interactions. *Proc. Natl. Acad. Sci. U.S.A.* **2006,** *103* (43), 15739-15746.

[71] Parsegian, V. A.; Zemb, T., Hydration Forces: Observations, Explanations, Expectations, Questions. *Curr. Opin. Colloid Interface Sci.* **2011,** *16* (6), 618-624.

[72] Pashley, R. M., Hydration Forces between Mica Surfaces in Aqueous-Electrolyte Solutions. *J. Colloid Interface Sci.* **1981,** *80* (1), 153-162.

[73] Witten, T. A.; Pincus, P. A., Colloid stabilization by long grafted polymers. *Macromolecules* **1986,** *19* (10), 2509-2513.

[74] Zhulina, E. B.; Borisov, O. V.; Priamitsyn, V. A., Theory of Steric Stabilization of Colloid Dispersions by Grafted Polymers. *J. Colloid Interface Sci.* **1990,** *137* (2), 495-511.

[75] Van Der Waals, J. D. Over de Continuiteit van den Gas - en Vloeistoftoestand (On the continuity of the gas and liquid state). Leiden The Netherlands, 1873.

[76] Mahanty, J.; Ninham, B. W., *Dispersion Forces* Academic Press London 1976.

[77] Lowdin, P. O., A Note on the Quantum-Mechanical Perturbation Theory. *J. Chem. Phys.* **1951,** *19* (11), 1396-1401.

[78] Hamaker, H. C., The London-van der Waals Attraction between Spherical Particles. *Physica* **1937,** *4*, 1058.

[79] Bergstrom, L., Hamaker constants of inorganic materials. *Adv. Colloid Interface Sci.* **1997,** *70*, 125-169.

[80] Lifshitz, E. M., The Theory of Molecular Attractive Forces between Solids. *Soviet Physics Jetp-Ussr* **1956,** *2* (1), 73-83.

[81] Casimir, H. B. G.; Polder, D., The Influence of Retardation on the London-van der waals Forces. *Phys. Rev.* **1948,** *73* (4), 360-372.

[82] Parsegian, V. A.; Ninham, B. W., Application of the Lifshitz Theory to the Calculation of Van der Waals Forces across Thin Lipid Films. *Nature* **1969,** *224*, 1197.

[83] Parsegian, V. A.; Ninham, B. W., Van der Waals Forces in Many-Layered Structures - Generalizations of Lifshitz Result for two Semi-Infinite Media. *J. Theor. Biol.* **1973,** *38* (1), 101-109.

[84] Kosmulski, M., *Surface charging and points of zero charge*. CRC Press: 2010.

[85] Kosmulski, M., The pH-dependent surface charging and points of zero charge V. Update. *J. Colloid Interface Sci.* **2011,** *353* (1), 1-15.

[86] Derjaguin, B., On the repulsive forces between charged colloid particles and on the theory of slow coagulation and stability of lyophobe sols. *Trans. Faraday Soc.* **1940,** *35* (3), 0203-0214.

[87] Bouyer, F.; Robben, A.; Yu, W. L.; Borkovec, M., Aggregation of colloidal particles in the presence of oppositely charged polyelectrolytes: Effect of surface charge heterogeneities. *Langmuir* **2001,** *17* (17), 5225-5231.

[88] Crocker, J. C.; Grier, D. G., Microscopic Measurement of the Pair Interaction Potential of Charge-Stabilized Colloid. *Phys. Rev. Lett.* **1994,** *73* (2), 352-355.

[89] Westall, J.; Hohl, H., A comparison of electrostatic models for the oxide/solution interface. *Adv. Colloid Interface Sci.* **1980,** *12*, 265-294.

[90] Grahame, D. C., The Electrical Double Layer and the Theory of Electrocapillarity. *Chem. Rev.* **1947,** *41* (3), 441-501.

[91] Parsons, R., The electrical double layer: Recent experimental and theoretical developments. *Chem. Rev.* **1990,** *90*, 813-826.

[92] Derjaguin, B. V., Main Factors Affecting the Stability of Colloids. *Prog. Surf. Sci.* **1993,** *43* (1-4), 109-114.

[93] Hogg, R.; Healy, T. W.; Fuerstenau, D. W., Mutual coagulation of colloidal dispersions. *Trans. Faraday Soc.* **1966,** *62*, 1638.

[94] Parsegian, V. A.; Gingell, D., On the Electrostatic Interaction across a Salt Solution between Two Bodies Bearing Unequal Charges. *Biophys. J.* **1972,** *12* (9), 1192-1204.

[95] Ninham, B. W.; Lo Nostro, P., *Molecular Forces and Self Assembly in Colloid, Nano Sciences and Biology*. Cambridge University Press: New York, USA, 2010.

[96] Carnie, S. L.; Chan, D. Y. C., Interaction Free-Energy between Plates with Charge Regulation - a Linearized Model. *J. Colloid Interface Sci.* **1993,** *161* (1), 260-264.

[97] Trefalt, G.; Behrens, S. H.; Borkovec, M., Charge Regulation in the Electrical Double Layer: Ion Adsorption and Surface Interactions. *Langmuir* **2016,** *32* (2), 380-400.

[98] Chan, D. Y.; Pashley, R.; White, L. R., A Simple Algorithm for the Calculation of the Electrostatic Repulsion between Identical Charged Surfaces in Electrolyte. *J. Colloid Interface Sci.* **1980,** *77* (1), 283-285.

[99] Visser, J., On Hamaker constants: A comparison between Hamaker constants and Lifshitz van der Waals constants. *Adv. Colloid Interface Sci.* **1972,** *3*, 331-363.

[100] Behrens, S. H.; Borkovec, M., Influence of the Secondary Interaction Energy Minimum on the Early Stages of Colloidal Aggregation. *J. Colloid Interface Sci.* **2000,** *225*, 460-465.

[101] Hogg, R.; Yang, K. C., Secondary coagulation *J. Colloid Interface Sci.* **1976,** *56*, 573-576.

[102] Hahn, M. W.; Abadzic, D.; O'Melia, C. R., Aquasols, On the Role of Secondary Minima. *Environ. Sci. Technol.* **2004,** *38*, 5915-5924.

[103] Ninham, B. W., On progress in forces since the DLVO theory. *Adv. Colloid Interface Sci.* **1999,** *83* (1-3), 1-17.

[104] Derjaguin, B. V., Analysis of Friction and Adhesion, IV. The Theory of the Adhesion of Small Particles. *Kolloid Z.* **1934,** *69*, 155-164.

[105] Cosgrove, T., *Colloid Science: Principles, Methods and Applications*. 2nd ed.; John Wiley & Sons, Inc.: Bristol, UK, 2010.

[106] Parsegian, V. A.; Rand, R. P.; Fuller, N. L., Direct osmotic stress measurements of hydration and electrostatic double-layer forces between bilayers of double-chained ammonium acetate surfactants. *J. Phys. Chem.* **1991,** *95* (12), 4777-4782.

[107] Parsegian, V. A.; Rand, R. P.; Rau, D. C., Osmotic stress, crowding, preferential hydration, and binding: A comparison of perspectives. *Proc. Natl. Acadm. Sci.* **2000,** *97* (8), 3987-3992.

[108] Hansen, P. L.; Podgornik, R.; Parsegian, V. A., Osmotic properties of DNA: Critical evaluation of counterion condensation theory. *Phys. Rev. E* **2001,** *64* (2), 021907.

[109] Hansen, P. L.; Cohen, J. A.; Podgornik, R.; Parsegian, V. A., Osmotic Properties of Poly(Ethylene Glycols): Quantitative Features of Brush and Bulk Scaling Laws. *Biophys. J.* **2003,** *84* (1), 350-355.

[110] Harries, D.; Rau, D. C.; Parsegian, V. A., Solutes Probe Hydration in Specific Association of Cyclodextrin and Adamantane. *J. Am. Chem. Soc.* **2005,** *127* (7), 2184-2190.

[111] Israelachvili, J. N.; Pashley, R. M., Molecular Layering of Water at Surfaces and Origin of Repulsive Hydration Forces. *Nature* **1983,** *306* (5940), 249-250.

[112] Valle-Delgado, J. J.; Molina-Bolivar, J. A.; Galisteo-Gonzalez, F.; Galvez-Ruiz, M. J.; Feiler, A.; Rutland, M. W., Hydration forces between silica surfaces: Experimental data and predictions from different theories. *J. Chem. Phys.* **2005,** *123* (3).

[113] Yoon, R. H.; Vivek, S., Effects of short-chain alcohols and pyridine on the hydration forces between silica surfaces. *J. Colloid Interface Sci.* **1998,** *204* (1), 179-186.

[114] Manciu, M.; Ruckenstein, E., Role of the hydration force in the stability of colloids at high ionic strengths. *Langmuir* **2001,** *17* (22), 7061-7070.

[115] Marcelja, S.; Radic, N., Repulsion of Interfaces Due to Boundary Water. *Chem. Phys. Lett.* **1976,** *42* (1), 129-130.

[116] Attard, P.; Patey, G. N., Continuum Electrostatic Interactions between Planar Lattices of Dipoles and the Possible Relevance to the Hydration Force. *Phys. Rev. A* **1991,** *43* (6), 2953-2962.

[117] Donaldson, S. H.; Lee, C. T.; Chmelka, B. F.; Israelachvili, J., Recent progress in understanding the hydrophobic interaction between surfaces in the nm to adhesive contact distance regime. *Abstr. Pap. Am. Chem. Soc.* **2011,** *241*.

[118] Israelachvili, J.; Pashley, R., The Hydrophobic Interaction Is Long-Range, Decaying Exponentially with Distance. *Nature* **1982,** *300* (5890), 341-342.

[119] Pashley, R. M.; Mcguiggan, P. M.; Ninham, B. W.; Evans, D. F., Attractive Forces between Uncharged Hydrophobic Surfaces - Direct Measurements in Aqueous-Solution. *Science* **1985,** *229* (4718), 1088-1089.

[120] Christenson, H. K.; Claesson, P. M., Cavitation and the Interaction between Macroscopic Hydrophobic Surfaces. *Science* **1988,** *239* (4838), 390-392.

[121] Claesson, P. M.; Christenson, H. K., Very Long-Range Attractive Forces between Uncharged Hydrocarbon and Fluorocarbon Surfaces in Water. *J. Phys. Chem.* **1988,** *92* (6), 1650-1655.

[122] Soga, Y.; Imanaka, H.; Imamura, K.; Ishida, N., Effect of Surface Hydrophobicity on Short-Range Hydrophobic Attraction between Silanated Silica Surfaces. *Adv. Powder Technol.* **2015,** *26* (6), 1729-1733.

[123] Ishida, N.; Kusaka, Y.; Ushijima, H., Hydrophobic Attraction between Silanated Silica Surfaces in the Absence of Bridging Bubbles. *Langmuir* **2012,** *28* (39), 13952-13959.

[124] Parker, J. L.; Cho, D. L.; Claesson, P. M., Plasma Modification of Mica - Forces between Fluorocarbon Surfaces in Water and a Nonpolar Liquid. *J. Phys. Chem.* **1989,** *93* (16), 6121-6125.

[125] Wood, J.; Sharma, R., How long is the long-range hydrophobic attraction? *Langmuir* **1995,** *11* (12), 4797-4802.

[126] Christenson, H. K.; Yaminsky, V. V., Is the long-range hydrophobic attraction related to the mobility of hydrophobic surface groups? *Colloids Surf., A* **1997,** *129*, 67-74.

[127] Parker, J. L.; Claesson, P. M.; Attard, P., Bubbles, cavities and the long-ranged attraction between hydrophobic surfaces. *J. Phys. Chem.* **1994,** *98* (34), 8468-8480.

[128] Ishida, N.; Sakamoto, M.; Miyahara, M.; Higashitani, K., Attraction between Hydrophobic Surfaces with and without Gas Phase. *Langmuir* **2000,** *16* (13), 5681-5687.

[129] Carambassis, A.; Jonker, L.; Attard, P.; Rutland, M., Forces measured between hydrophobic surfaces due to a submicroscopic bridging bubble. *Phys. Rev. Lett.* **1998,** *80* (24), 5357-5360.

[130] Craig, V. S. J., Very Small Bubbles at Surfaces-The Nanobubble Puzzle. *Soft Matter* **2011,** *7* (1), 40-48.

[131] Alheshibri, M.; Qian, J.; Jehannin, M.; Craig, V. S. J., A History of Nanobubbles. *Langmuir* **2016,** *32* (43), 11086-11100.

[132] Pincus, P., Colloid stabilization with grafted polyelectrolytes. *Macromolecules* **1991,** *24*, 2912-2919.

[133] Rubinstein, M.; Colby, R. H., *Polymer physics*. Oxford University Press London 2003.

[134] Butt, H. J.; kappl, M.; Mueller, H.; Raiteri, R.; Meyer, W.; Ruhe, J., Steric Forces Measured with the Atomic Force Microscope at Various Temperatures. *Langmuir* **1999,** *15*, 2559-2565.

[135] Biggs, S., Steric and Bridging Forces between Surfaces Bearing Adsorbed Polymer: An Atomic Force Microscopy Study. *Langmuir* **1995,** *11*, 156-162.

[136] Leong, Y. K.; Scales, P. J.; Healy, T. W.; Boger, D. V.; Buscall, R., Rheological Evidence of Adsorbate-Mediated Short-range Steric Forces in Concentrated Dispersions. *J. Chem. Soc., Faraday Trans.* **1993,** *89* (14), 2473-2478.

[137] Craig, V. S. J., An Historical Review of Surface Force Measurement Techniques. *Colloids Surf., A* **1997,** *129*, 75-93.

[138] Tomlinson, G. A., Molecular cohesion. *Philos. Mag.* **1928,** *6* (37), 695.

[139] Bradley, M. A., The cohesive force between solid surfaces and the surface energy of solids. *Philos. Mag.* **1932,** *13* (86), 853.

[140] Rayleigh, J. W. S., A study of glass surfaces in optical contact. *Proc. R. Soc. London Ser. A* **1936,** *156*, 326.

[141] Derjaguin, B. V.; Titijevskaia, A. S.; Abricossova, I. I.; Malkina, A. D., Investigations of the Forces of Interaction of Surfaces in Different Media and

Their Application to the Problem of Colloid Stability. *Discuss. Faraday Soc.* **1954,** (18), 24-41.

[142] Israelachvili, J. N., Thin-Film Studies Using Multiple-Beam Interferometry. *J. Colloid Interface Sci.* **1973,** *44* (2), 259-272.

[143] Horn, R. G.; Clarke, D. R.; Clarkson, M. T., Direct Measurement of Surface Forces between Sapphire Crystals in Aqueous-Solutions. *J. Mater. Res.* **1988,** *3* (3), 413-416.

[144] Chen, N. H.; Maeda, N.; Tirrell, M.; Israelachvili, J., Adhesion and friction of polymer surfaces: The effect of chain ends. *Macromolecules* **2005,** *38* (8), 3491-3503.

[145] Connor, J. N.; Horn, R. G., Extending the surface force apparatus capabilities by using white light interferometry in reflection. *Rev. Sci. Instrum.* **2003,** *74* (11), 4601-4606.

[146] Kawai, H.; Sakuma, H.; Mizukami, M.; Abe, T.; Fukao, Y.; Tajima, H.; Kurihara, K., New surface forces apparatus using two-beam interferometry. *Rev. Sci. Instrum.* **2008,** *79* (4).

[147] Georges, J. M.; Millot, S.; Loubet, J. L.; Tonck, A., Drainage of Thin Liquid-Films between Relatively Smooth Surfaces. *J. Chem. Phys.* **1993,** *98* (9), 7345-7360.

[148] Frantz, P.; Agrait, N.; Salmeron, M., Use of capacitance to measure surface forces .1. Measuring distance of separation with enhanced spatial and time resolution. *Langmuir* **1996,** *12* (13), 3289-3294.

[149] Stewart, A. M., Capacitance dilatometry attachment for a surface-force apparatus. *Meas. Sci. Technol.* **2000,** *11* (3), 298-304.

[150] Ashkin, A.; Dziedzic, J. M.; Bjorkholm, J. E.; Chu, S., Observation of a Single-Beam Gradient Force Optical Trap for Dielectric Particles. *Opt. Lett.* **1986,** *11* (5), 288-290.

[151] Simmons, R. M.; Finer, J. T.; Chu, S.; Spudich, J. A., Quantitative measurements of force and displacement using an optical trap. *Biophys. J.* **1996,** *70* (4), 1813-1822.

[152] Tolić-Nørrelykke, S. F., Calibration of optical tweezers with positional detection in the back focal plane. *Rev. Sci. Instrum.* **2006,** *77*, 103101.

[153] Svoboda, K.; Block, S. M., Biological Applications of Optical Forces. *Annu. Rev. Biophys. Biomol. Struct.* **1994,** *23*, 247-285.

[154] Alexander, B. M.; Prieve, D. C., A Hydrodynamic Technique for Measurement of Colloidal Forces. *Langmuir* **1987,** *3* (5), 788-795.

[155] Walz, J. Y., Measuring particle interactions with total internal reflection microscopy. *Curr. Opin. Colloid Interface Sci.* **1997,** *2*, 600-606.

[156] Axelrod, D., Total internal reflection fluorescence microscopy in cell biology. *Traffic* **2001,** *2* (11), 764-774.

[157] Biggs, S.; Prieve, D. C.; Dagastine, R. R., Direct Comparison of Atomic Force Microscopic and Total Internal Reflection Microscopic Measurements in the Presence of Nonadsorbing Polyelectrolytes. *Langmuir* **2005,** *21*, 5421-5428.

[158] Prieve, D. C., Measurement of colloidal forces with TIRM. *Adv. Colloid Interface Sci.* **1999,** *82* (1-3), 93-125.

[159] Giessibl, F. J., Advances in atomic force microscopy. *Rev. Mod. Phys.* **2003,** *75*, 949.

[160] Haugstad, G., *Atomic Force Microscopy: Understanding Basic Modes and Advanced Applications* John Wiley & Sons, Inc: New Jersey 2012.

[161] Ralston, J.; Larson, I.; Rutland, M. W.; Feiler, A. A.; Kleijn, M., Atomic force microscopy and direct surface force measurements - (IUPAC technical report). *Pure Appl. Chem.* **2005,** *77* (12), 2149-2170.

[162] Ghislain, L. P.; Switz, N. A.; Webb, W. W., Measurement of small forces using an optical trap. *Rev. Sci. Instrum.* **1994,** *65*, 2762-2768.

[163] Redding, B.; Pan, Y. L., Optical trap for both transparent and absorbing particles in air using a single shaped laser beam. *Opt. Lett.* **2015,** *40* (12), 2798-2801.

[164] Axelrod, D.; Thompson, N. L.; Burghardt, T. P., Total Internal-Reflection Fluorescent Microscopy. *J. Microsc.* **1983,** *129*, 19-28.

[165] Temple, P. A., Total Internal-Reflection Microscopy - a Surface Inspection Technique. *Appl. Opt.* **1981,** *20* (15), 2656-2664.

[166] Johnson, R. W.; Hultqvist, A.; Bent, S. F., A brief review of atomic layer deposition: from fundamentals to applications. *Mater. Today* **2014,** *17* (5), 236-246.

[167] Ducker, W. A.; Senden, T. J.; Pashley, R. M., Direct Measurement of Colloidal Forces Using an Atomic Force Microscope. *Nature* **1991,** *353* (6341), 239-241.

[168] Suntola, T.; Antson, J. Method for Producing Compound Thin Films. Nov. 25 1977.

[169] Benick, J.; Hoex, B.; van de Sanden, M. C. M.; Kessels, W. M. M.; Schultz, O.; Glunz, S. W., High efficiency n-type Si solar cells on Al2O3-passivated boron emitters. *Appl. Phys. Lett.* **2008,** *92* (25).

[170] Schmidt, H.; Zilberberg, K.; Schmale, S.; Flugge, H.; Riedl, T.; Kowalsky, W., Transient characteristics of inverted polymer solar cells using titaniumoxide interlayers. *Appl. Phys. Lett.* **2010,** *96* (24).

[171] Palomares, E.; Clifford, J. N.; Haque, S. A.; Lutz, T.; Durrant, J. R., Control of charge recombination dynamics in dye sensitized solar cells by the use of conformally deposited metal oxide blocking layers. *J. Am. Chem. Soc.* **2003,** *125* (2), 475-482.

[172] Lim, J. S.; Kim, Y. K.; Choi, S. J.; Lee, J. H.; Kim, Y. S.; Lee, B. T.; Park, H. S.; Park, Y. W.; I., L. S., Novel Aluminium Oxide capacitor for high density DRAMs In *ICVC '99. 6th International Conference* VLSI and CAD: Seoul, South Korea 1999; pp 506-509.

[173] Mistry, K., et al., A 45nm logic technology with high-k plus metal gate transistors, strained silicon, 9 Cu interconnect layers, 193 nm dry patterning, and 100% Pb-free packaging. *2007 Ieee International Electron Devices Meeting, Vols 1 and 2* **2007**, 247-+.

[174] Son, K. S.; Bae, K.; Kim, J. W.; Ha, J. S.; Shim, J. H., Ion conduction in nanoscale yttria-stabilized zirconia fabricated by atomic layer deposition with various doping rates. *J. Vac. Sci. Technol.* **2013,** *31* (1).

[175] Chao, C. C.; Park, J. S.; Tian, X.; Shim, J. H.; Gur, T. M.; Prinz, F. B., Enhanced Oxygen Exchange on Surface-Engineered Yttria-Stabilized Zirconia. *Acs Nano* **2013,** *7* (3), 2186-2191.

[176] Knez, M.; Niesch, K.; Niinisto, L., Synthesis and surface engineering of complex nanostructures by atomic layer deposition. *Adv. Mater.* **2007,** *19* (21), 3425-3438.

[177] Pore, V.; Hatanpaa, T.; Ritala, M.; Leskela, M., Atomic Layer Deposition of Metal Tellurides and Selenides Using Alkylsilyl Compounds of Tellurium and Selenium. *J. Am. Chem. Soc.* **2009,** *131* (10), 3478-+.

[178] Chen, P.; Mitsui, T.; Farmer, D. B.; Golovchenko, J.; Gordon, R. G.; Branton, D., Atomic layer deposition to fine-tune the surface properties and diameters of fabricated nanopores. *Nano Lett.* **2004,** *4* (7), 1333-1337.

[179] Aarik, J.; Aidla, A.; Kiisler, A. A.; Uustare, T.; Sammelselg, V., Influence of Substrate Temperature on Atomic Layer Growth and Properties of HfO2 Thin Films. *Thin Solid Films* **1999,** *340* (1-2), 110-116.

[180] Hausmann, D. M.; Kim, E.; Becker, J.; Gordon, R. G., Atomic Layer Deposition of Hafnium and Zirconium Oxides Using Metal Amide Precursors. *Chem. Mater.* **2002,** *14* (10), 4350-4358.

[181] Moreno-Herrero, F.; Colchero, J.; Gomez-Herrero, J.; Baro, A. M., Atomic force microscopy contact, tapping, and jumping modes for imaging biological samples in liquids. *Phys. Rev. E.,* **2004,** *69* (3).

[182] Cleveland, J. P.; Manne, S.; Bocek, D.; Hansma, P. K., A Nondestructive Method for Determining the Spring Constant of Cantilevers for Scanning Force Microscopy. *Rev. Sci. Instrum.* **1993,** *64* (2), 403-405.

[183] Hutter, J. L.; Bechhoefer, J., Calibration of Atomic-Force Microscope Tips. *Rev. Sci. Instrum.* **1993,** *64* (7), 1868-1873.

[184] Sader, J. E.; Chon, J. W. M.; Mulvaney, P., Calibration of rectangular atomic force microscope cantilevers. *Rev. Sci. Instrum.* **1999,** *70* (10), 3967-3969.

[185] Ecke, S.; Raiteri, R.; Bonaccurso, E.; Reiner, C.; Deiseroth, H. J.; Butt, H. J., Measuring normal and friction forces acting on individual fine particles. *Rev. Sci. Instrum.* **2001,** *72* (11), 4164-4170.

[186] Malovichko, I. M., Measuring AFM Cantilever Stiffness from a Thermal Noise Spectrum. *Bull. Russ. Acad. Sci. Physics.* **2013,** *77*, 1073-1075.

[187] Butt, H.-J., Measuring Electrostatic, van der Waals, and Hydration Forces in Electrolyte Solutions with an Atomic Force Microscope. *Biophys. J.* **1991,** *60* (6), 1438-1444.

[188] Sader, J. E.; Larson, I.; Mulvaney, P.; White, L. R., Method for the Calibration of Atomic-Force Microscope Cantilevers. *Rev. Sci. Instrum.* **1995,** *66* (7), 3789-3798.

[189] Henry, C. L.; Parkinson, L.; Ralston, J. R.; Craig, V. S. J., A mobile gas-water interface in electrolyte solutions. *J. Phys. Chem. C* **2008,** *112* (39), 15094-15097.

[190] Als-Nielsen, J.; McMorrow, D., *Elements of Modern X-ray Physics* John Wiley & Sons, Ltd New York, 2001.

[191] Chason, E.; Mayer, T. M., Thin Film and Surface Characterization by Specular X-ray Reflectivity. *Crit. Rev. Solid State Mater. Sci.* **1997,** *22* (1), 1-67.

[192] Parrat, L. G., Surface Studies of Solids by Total Reflection of X-Rays. *Phys. Rev.* **1954,** *95*, 359-369.

[193] Nelson, A., Motofit - Integrating Neutron Reflectometry Acquisition, Reduction and Analysis into One, Easy to use, Package. *J. Phys. Conf. Ser.* **2010,** *251*, 012094.

[194] Yasaka, M., X-Ray Thin-Film Measurement Techniques V. X- Ray Reflectivity Measurement. *Rigaku J.* **2010,** *26* (2), 1-9.

[195] Hunter, R. J., *Zeta potential in colloid science: Principles and Applications* Academic Press London 1986.

[196] Obrien, R. W.; White, L. R., Electrophoretic Mobility of a Spherical Colloidal Particle. *J. Chem. Soc., Faraday Trans.* **1978,** *74*, 1607-1626.

[197] Application Note: Measuring Surface Zeta Potential using the Surface Zeta Potential Cell. Malvern Instruments Limited: Worcestershire, UK, 2014.

[198] Reichelt, R., Scanning Electron Microscopy In *Science of Microscopy* Hawkes, P. W.; Spence, J. C. H., Eds. Springer New York, 2007.

[199] Young, T. J.; Monclus, M. A.; Burnett, T. L.; Broughton, W. R.; Ogin, S. L.; Smith, P. A., The Use of the PeakForceTM Quantitative Nanomechanical Mapping AFM-Based Method for High-Resolution Young's Modulus Measurement of Polymers. *Meas. Sci. Technol.* **2011,** *22*, 125703.

[200] Neto, C.; Craig, V. S. J., Colloid Probe Characterization: Radius and Roughness Determination. *Langmuir* **2001,** *17* (7), 2097-2099.

[201] Eom, N.; Parsons, D. F.; Craig, V. S. J., Roughness in Surface Force Measurements: Extension of DLVO Theory To Describe the Forces between Hafnia Surfaces. *J. Phys. Chem. B* **2017,** *121*, 6442-6453.

[202] Eom, N.; Walsh, R. B.; Liu, G.; Parsons, D. F.; Craig, V. S. J., Surface Forces in Particle Technology: Wet Systems. *Procedia Eng.* **2015,** *102*, 24-34.

[203] Parsons, D. F.; Walsh, R. B.; Craig, V. S. J., Surface Forces: Surface Roughness in Theory and Experiment. *J. Chem. Phys.* **2014,** *140* (16), 164701.

[204] Park, T. J.; Byun, Y.; Wallace, R. M.; Kim, J., Reduced impurities and improved electrical properties of atomic-layer-deposited HfO2 film grown at a low temperature (100 ◦C) by Al2O3 incorporation. *Appl. Surf. Sci.* **2016,** *371*, 360-364.

[205] NIST Center for Neutron Research, Neutron activation and scattering calculator. https://www.ncnr.nist.gov/resources/activation/.

[206] Canet-Ferrer, J.; Coronado, E.; Forment-Aliaga, A.; Pinilla-Cienfuegos, E., Correction of the tip convolution effects in the imaging of nanostructures studied through scanning force microscopy. *Nanotechnology* **2014,** *25*, 395703.

[207] Thormann, E., Surface Forces between Rough and Topographically Structured Interfaces. *Curr. Opin. Colloid Interface Sci.* **2017,** *27*, 18-24.

[208] Elzbieciak-Wodka, M.; Popescu, M. N.; Ruiz-Cabello, F. J. M.; Trefalt, G.; Maroni, P.; Borkovec, M., Measurements of dispersion forces between colloidal latex particles with the atomic force microscope and comparison with Lifshitz theory. *J. Chem. Phys.* **2014,** *140* (10), 11.

[209] Wong, B. P.; Mittal, A.; Starr, G. W.; Zach, F.; Moroz, V.; Kahng, A., *Nano-CMOS Design for Manufacturability: Robust Circuit and Physical Design for Sub-65nm Technology Nodes*. John Wiley & Sons, Inc.: New Jersey, 2009.

[210] Valtiner, M.; Banquy, X.; Kristiansen, K.; Greene, G. W.; Israelachvili, J. N., The Electrochemical Surface Forces Apparatus: The Effect of Surface Roughness, Electrostatic Surface Potentials, and Anodic Oxide Growth on Interaction Forces, and Friction between Dissimilar Surfaces in Aqueous Solutions. *Langmuir* **2012,** *28* (36), 13080-13093.

[211] Kane, V.; Mulvaney, P., Double-Layer Interactions between Self-Assembled Monolayers of Omega-Mercaptoundecanoic Acid on Gold Surfaces. *Langmuir* **1998,** *14* (12), 3303-3311.

[212] Adler, J. J.; Rabinovich, Y. I.; Moudgil, B. M., Origins of the Non-DLVO Force between Glass Surfaces in Aqueous Solution. *J. Colloid Interface Sci.* **2001,** *237* (2), 249-258.

[213] Larson, I.; Drummond, C. J.; Chan, D. Y. C.; Grieser, F., Direct Force Measurements between Dissimilar Metal-Oxides. *J. Phys. Chem.* **1995,** *99* (7), 2114-2118.

[214] Popa, I.; Sinha, P.; Finessi, M.; Maroni, P.; Papastavrou, G.; Borkovec, M., Importance of Charge Regulation in Attractive Double-Layer Forces between Dissimilar Surfaces. *Phys. Rev. Lett.* **2010,** *104* (22), 228301.

[215] Besteman, K.; Zevenbergen, M. A. G.; Heering, H. A.; Lemay, S. G., Direct observation of charge inversion by multivalent ions as a universal electrostatic phenomenon. *Phys. Rev. Lett.* **2004,** *93* (17), 170802.

[216] Miklavic, S. J.; Chan, D. Y. C.; White, L. R.; Healy, T. W., Double-Layer Forces between Heterogeneous Charged Surfaces. *J. Phys. Chem.* **1994,** *98* (36), 9022-9032.

[217] Miklavcic, S. J., Double-Layer Forces between Heterogeneous Charged Surfaces - The Effect of Net Surface-Charge. *J. Chem. Phys.* **1995,** *103* (11), 4794-4806.

[218] Taylor, M. L.; Morris, G. E.; Smart, R. S., Influence of aluminum doping on titania pigment structural and dispersion properties. *J. Colloid Interface Sci.* **2003,** *262* (1), 81-88.

[219] Saidur, R.; Leong, K. Y.; Mohammad, H. A., A review on applications and challenges of nanofluids. *Renew. Sustainable Energy Rev.* **2011,** *15* (3), 1646-1668.

[220] Buffle, J.; Wilkinson, K. J.; Stoll, S.; Filella, M.; Zhang, J. W., A generalized description of aquatic colloidal interactions: The three-colloidal component approach. *Environ. Sci. Technol.* **1998,** *32* (19), 2887-2899.

[221] Hierrezuelo, J.; Sadeghpour, A.; Szilagyi, I.; Vaccaro, A.; Borkovec, M., Electrostatic Stabilization of Charged Colloidal Particles with Adsorbed Polyelectrolytes of Opposite Charge. *Langmuir* **2010,** *26* (19), 15109-15111.

[222] Fritz, G.; Schadler, V.; Willenbacher, N.; Wagner, N. J., Electrosteric stabilization of colloidal dispersions. *Langmuir* **2002,** *18* (16), 6381-6390.

[223] Heller, W.; Pugh, T. L., Steric Stabilization of Colloidal Solutions by Adsorptions of Flexible Macromolecules. *J. Polym. Sci.* **1960,** *47* (0149), 203-217.

[224] Teh, E. J.; Leong, Y. K.; Craig, V. S. J., Surface Forces and Rheology of Titanium Dioxide in the Presence of Dicarboxylic Acids: From Molecular Interactions to Yield Stress. *Langmuir* **2017,** *33*, 1496-1506.

[225] Leong, Y. K., Molecular configuration of adsorbed cis- and trans-1,2-ethylene dicarboxylic acids and interparticle forces in colloidal dispersions. *Langmuir* **2002,** *18* (6), 2448-2449.

[226] Leong, Y. K., Role of Molecular Architecture of Citric and Related Polyacids on the Yield Stress of alpha-Alumina Slurries: Inter- and Intramolecular Forces. *J. Am. Ceram. Soc.* **2010,** *93* (9), 2598-2605.

[227] Leong, Y. K.; Scales, P. J.; Healy, T. W.; Boger, D. V., Interparticle Forces Arising from Adsorbed Polyelectrolytes in Colloidal Suspensions. *Colloids Surf., A.* **1995,** *95* (1), 43-52.

[228] Das, K. K.; Somasundaran, P., Flocculation-Dispersion Characteristics of Alumina using a Wide Molecular Weight Range of Polyacrylic Acids. *Colloids Surf., A.* **2003,** *223* (1-3), 17-25.

[229] Penniston, K. L.; Nakada, S. Y.; Holmes, R. P.; Assimos, D. G., Quantitative Assessment of Citric Acid in Lemon Juice, Lime Juice, and Commercially-Available Fruit Juice Products. *J. Endourol.* **2008,** *22*, 567-570.

[230] Sacks, M. D.; Tseng, T.-Y., Role of Sodium Citrate in Aqueous Milling of Aluminum Oxide. *J. Am. Ceram. Soc.* **1983,** *66* (4), 242-247.

[231] Xiao, C.; Chen, H.; Yu, X.; Gao, L.; Guo, L., Dispersion of Aqueous Alumina Suspensions with Biodegradable Polymers Dispersion of Alumina

Suspensions with Biodegradable Polymers. *J. Am. Ceram. Soc. 94* (10), 3276-3281.

[232] Zhang, J.; Xu, Q.; Ye, F.; Lin, Q.; Jiang, D.; Iwasa, M., Effect of citric acid on the adsorption behavior of polyethylene imine (PEI) and the relevant stability of SiC slurries. *Colloids Surf., A* **2006,** *276* (1–3), 168-175.

[233] Hanaor, D.; Michelazzi, M.; Leonelli, C.; Sorrell, C. C., The effects of carboxylic acids on the aqueous dispersion and electrophoretic deposition of ZrO2. *J. Eur. Ceram. Soc.* **2012,** *32* (1), 235-244.

[234] Teh, E. J.; Leong, Y. K.; Liu, Y.; Fourie, A. B.; Fahey, M., Differences in the Rheology and Surface Chemistry of Kaolin Clay Slurries: The Source of the Variations. *Chem. Eng. Sci.* **2009,** *64* (17), 3817-3825.

[235] Leong, Y.-K.; Teo, J.; Teh, E.; Smith, J.; Widjaja, J.; Lee, J.-X.; Fourie, A.; Fahey, M.; Chen, R., Controlling attractive interparticle forces via small anionic and cationic additives in kaolin clay slurries. *Chem. Eng. Res. Des.* **2012,** *90* (5), 658-666.

[236] Chun, J.; Poloski, A. P.; Hansen, E. K., Stabilization and control of rheological properties of Fe2O3/Al(OH)3-rich colloidal slurries under high ionic strength and pH. *J. Colloid Interface Sci.* **2010,** *348* (1), 280-288.

[237] Khoo, K. S.; Teh, E. J.; Leong, Y. K.; Ong, B. C., Hydrogen Bonding and Interparticle Forces in Platelet alpha-Al2O3 Dispersions: Yield Stress and Zeta Potential. *Langmuir* **2009,** *25* (6), 3418-3424.

[238] Hidber, P. C.; Graule, T. J.; Gauckler, L. J., Citric acid - A Dispersant for Aqueous Alumina Suspensions. *J. Am. Ceram. Soc.* **1996,** *79* (7), 1857-1867.

[239] Mudunkotuwa, I. A.; Grassian, V. H., Citric Acid Adsorption on TiO2 Nanoparticles in Aqueous Suspensions at Acidic and Circumneutral pH:

Surface Coverage, Surface Speciation, and Its Impact on Nanoparticle-Nanoparticle Interactions. *J. Am. Chem. Soc.* **2010,** *132* (42), 14986-14994.

[240] Henglein, A.; Giersig, M., Formation of colloidal silver nanoparticles: Capping action of citrate. *J. Phys. Chem. B* **1999,** *103* (44), 9533-9539.

[241] Lin, Y.; Pan, G. B.; Su, G. J.; Fang, X. H.; Wan, L. J.; Bai, C. L., Study of citrate adsorbed on the Au(111) surface by scanning probe microscopy. *Langmuir* **2003,** *19* (24), 10000-10003.

[242] Hu, Y. Y.; Rawal, A.; Schmidt-Rohr, K., Strongly bound citrate stabilizes the apatite nanocrystals in bone. *Proc. Natl. Acadm. Sci.* **2010,** *107* (52), 22425-22429.

[243] Mann, K. G.; Whelihan, M. F.; Butenas, S.; Orfeo, T., Citrate anticoagulation and the dynamics of thrombin generation. *J. Thromb. Haemost.* **2007,** *5* (10), 2055-2061.

[244] Cieslinski, G.; Van Rees, K. C. J.; Szmigielska, A. M.; Krishnamurti, G. S. R.; Huang, P. M., Low-molecular-weight organic acids in rhizosphere soils of durum wheat and their effect on cadmium bioaccumulation. *Plant Soil* **1998,** *203* (1), 109-117.

[245] Jones, D. L.; Brassington, D. S., Sorption of organic acids in acid soils and its implications in the rhizosphere. *Eur. J. Soil. Sci.* **1998,** *49* (3), 447-455.

[246] Jones, D. L., Organic acids in the rhizosphere - a critical review. *Plant Soil* **1998,** *205* (1), 25-44.

[247] Bailey, G. W.; Shevchenko, S. M.; Yu, Y. S.; Kamermans, H., Combining scanning tunneling microscopy and computer simulation of humic substances: Citric acid, a model. *Soil Sci. Soc. Am. J.* **1997,** *61* (1), 92-101.

[248] Lenhart, J. J.; Cabaniss, S. E.; MacCarthy, P.; Honeyman, B. D., Uranium(VI) complexation with citric, humic and fulvic acids. *Radiochim. Acta* **2000,** *88* (6), 345-353.

[249] Biggs, S.; Scales, P. J.; Leong, Y.-K.; Healy, T. W., Effects of Citrate Adsorption on the Interactions between Zirconia Surfaces. *J. Chem. Soc., Faraday Trans.* **1995,** *91* (17), 2921-2928.

[250] van Zwol, P. J.; Palasantzas, G.; van de Schootbrugge, M.; de Hosson, J. T. M.; Craig, V. S. J., Roughness of microspheres for force measurements. *Langmuir* **2008,** *24* (14), 7528-7531.

[251] Wangchareansak, T.; Craig, V. S. J.; Notley, S. M., Adsorption Isotherms and Structure of Cationic Surfactants Adsorbed on Mineral Oxide Surfaces Prepared by Atomic Layer Deposition. *Langmuir* **2013,** *29* (48), 14748-14755.

[252] Dijt, J.; Stuart, M. C.; Hofman, J.; Fleer, G., Kinetics of polymer adsorption in stagnation point flow. *Colloids surf.* **1990,** *51*, 141-158.

[253] Howard, S. C.; Craig, V. S. J., Adsorption of the cationic surfactant CTAB to silica in the presence of sodium salicylate: surface excess and kinetics. *Langmuir* **2009,** *25*, 13015-13024.

[254] Howard, S. C.; Craig, V. S. J., Very slow surfactant adsorption at the solid-liquid interface is due to long lived surface aggregates. *Soft Matter* **2009,** *5* (16), 3061-3069.

[255] Azzam, R.; Bashara, N.; Burns, D. T., Ellipsometry and polarized light. *Anal. Chim. Acta* **1987,** *199*, 283-284.

[256] Hwang, Y. S.; Lenhart, J. J., Adsorption of C4-Dicarboxylic Acids at the Hematite/Water Interface. *Langmuir* **2008,** *24* (24), 13934-13943.

[257] Masu, K.; Ishihara, N.; Nakayama, N.; Sato, T.; Amakawa, S., Physical design challenges to nano-CMOS circuits. *Ieice Electronics Express* **2009,** *6* (11), 703-720.

[258] Grahame, D. C., Diffuse Double Layer Theory for Electrolytes of Unsymmetrical Valence Types. *J. Chem. Phys.* **1953,** *21*, 1054-1060.

[259] Jones, D. L.; Dennis, P. G.; Owen, A. G.; van Hees, P. A. W., Organic acid behavior in soils - misconceptions and knowledge gaps. *Plant Soil* **2003,** *248* (1-2), 31-41.

[260] Jones, D. L.; Darrah, P. R., Role of root derived organic-acids in the mobilization of nutrients from the rhizosphere. *Plant Soil* **1994,** *166* (2), 247-257.

[261] Miyasaka, S. C.; Buta, J. G.; Howell, R. K.; Foy, C. D., Mechanism of aluminum tolerance in snapbeans - root exudation of citric-acid. *Plant Physiol.* **1991,** *96* (3), 737-743.

[262] Nel, A.; Xia, T.; Madler, L.; Li, N., Toxic potential of materials at the nanolevel. *Science* **2006,** *311* (5761), 622-627.

[263] Smita, S.; Gupta, S. K.; Bartonova, A.; Dusinska, M.; Gutleb, A. C.; Rahman, Q., Nanoparticles in the environment: assessment using the causal diagram approach. *Environ. Health* **2012,** *11*.

[264] Nowack, B.; Bucheli, T. D., Occurrence, behavior and effects of nanoparticles in the environment. *Environ. Pollut.* **2007,** *150* (1), 5-22.

[265] Mueller, N. C.; Nowack, B., Exposure modeling of engineered nanoparticles in the environment. *Environ. Sci. Techn.* **2008,** *42* (12), 4447-4453.

[266] Heyder, J.; Gebhart, J.; Rudolf, G.; Schiller, C. F.; Stahlhofen, W., Deposition of particles in the human respiratory-tract in the size range 0.005-15-microns. *J. Aerosol Sci.* **1986,** *17* (5), 811-825.

[267] Monopoli, M. P.; Aberg, C.; Salvati, A.; Dawson, K. A., Biomolecular coronas provide the biological identity of nanosized materials. *Nat. Nanotech.* **2012,** *7* (12), 779-786.

[268] Nel, A. E.; Madler, L.; Velegol, D.; Xia, T.; Hoek, E. M. V.; Somasundaran, P.; Klaessig, F.; Castranova, V.; Thompson, M., Understanding biophysicochemical interactions at the nano-bio interface. *Nat. Mater.* **2009,** *8* (7), 543-557.

[269] Liu, J.; Aruguete, D. A.; Jinschek, J. R.; Rimstidt, J. D.; Hochella, M. F., The non-oxidative dissolution of galena nanocrystals: Insights into mineral dissolution rates as a function of grain size, shape, and aggregation state. *Geochim. Cosmochim. Acta.* **2008,** *72* (24), 5984-5996.

[270] Blake, T. D.; Kitchener, J. A., Stability of Aqueous Films on Hydrophobic Methylated Silica. *J. Chem. Soc., Faraday Trans.* **1972,** *68*, 1435-1442.

[271] Tanford, C., *The Hydrophobic Effect*. 2nd ed.; Wiley: New York, 1980.

[272] Ducker, W. A.; Mastropietro, D., Forces between extended hydrophobic solids: Is there a long-range hydrophobic force? *Curr. Opin. Colloid Interface Sci.* **2016,** *22*, 51-58.

[273] Parker, J. L.; Claesson, P. M.; Wang, J.-H.; Yasuda, H. K., Surface forces between plasma polymer films *Langmuir* **1994,** *10*, 2766-2773.

[274] Wood, J.; Sharma, R., Interaction forces between hydrophobic mica surfaces. *J. Adhes. Sci. Technol.* **1995,** *9*, 1075 - 1085.

[275] Christenson, H. K.; Fang, J.; Ninham, B. W.; Parker, J. L., Effect of divalent electroylte on the hydrophobic attraction *J. Phys. Chem.* **1990,** *94*, 8004-8006.

[276] Hato, M., Attractive Forces between Surfaces of Controlled "Hydrophobicity" across Water: A Possible Range of "Hydrophobic Interactions" between Macroscopic Hydrophobic Surfaces across Water. *J. Phys. Chem.* **1996,** *100*, 18930-18538.

[277] Claesson, P. M.; Blom, C. E.; Herder, P. C.; Ninham, B. W., Interactions between water-stable hydrophobic langmuir-blodgett monolayers on mica. *J. Colloid Interface Sci.* **1986,** *114* (1), 234-242.

[278] Claesson, P. M.; Christenson, H. K., Very long range attractive forces between uncharged hydrocarbon and fluorocarbon surfaces in water. *J. Phys. Chem.* **1988,** *92* (6), 1650-1655.

[279] Meyer, E. E.; Lin, Q.; Hassenkam, T.; Oroudjev, E.; Israelachvili, J. N., Origin of the Long-Range Attraction between Surfactant-Coated Surfaces. *Proc. Natl. Acad. Sci. U.S.A* **2005,** *102* (19), 6839-6842.

[280] Kekicheff, P.; Spalla, O., Long-Range Electrostatic Attraction between Similar, Charge-Neutral Walls. *Phys. Rev. Lett.* **1995,** *75* (9), 1851-1854.

[281] Karaman, M. E.; Meagher, L.; Pashley, R. M., Surface-chemistry of emulsion polymerization. *Langmuir* **1993,** *9* (5), 1220-1227.

[282] Tabor, R. F.; Wu, C.; Grieser, F.; Dagastine, R. R.; Chan, D. Y. C., Measurement of the Hydrophobic Force in a Soft Matter System. *J. Phys. Chem. Lett.* **2013,** *4* (22), 3872-3877.

[283] Rustan, A. C.; Drevon, C. A., *Fatty Acids: Structures and Properties. Encyclopedia of Life Sciences*. Nature Publishing: London, 2000.

[284] Ouimet, J.; Croft, S.; Pare, C.; Katsaras, J.; Lafleur, M., Modulation of the polymorphism of the palmitic acid/cholesterol system by the pH. *Langmuir* **2003,** *19* (4), 1089-1097.

[285] Slacik, S. Structural Characterization of the Interface between a Fatty Acid Langmuir Monolayer and Water using Molecular Simulations. Charles University Prague, 2011.

[286] Ishida, N.; Inoue, T.; Miyahara, M.; Higashitani, K., Nano Bubbles on a Hydrophobic Surface in Water Observed by Tapping-Mode Atomic Force Microscopy. *Langmuir* **2000,** *16* (16), 6377-6380.

[287] Senden, T. J.; Drummond, C. J., Surface-Chemistry and Tip Sample Interactions in Atomic-Force Microscopy. *Colloids Surf., A* **1995,** *94* (1), 29-51.

[288] Grabbe, A., Double-layer interactions between silylated silica surfaces. *Langmuir* **1993,** *9* (3), 797-801.

[289] Garcia, J. C.; Scolfaro, L. M. R.; Leite, J. R.; Lino, A. T.; Freire, V. N.; Farias, G. A.; da Silva, E. F., Effective masses and complex dielectric function of cubic HfO2. *Appl. Phys. Lett.* **2004,** *85* (21), 5022-5024.

[290] Masuda, T.; Matsuki, Y.; Shimoda, T., Spectral parameters and Hamaker constants of silicon hydride compounds and organic solvents. *J. Colloid Interface Sci.* **2009,** *340* (2), 298-305.

[291] Langbein., D., *Theory of van der Waals Attraction* Springer-Verlag: New York 1974; Vol. 72.

[292] Perkin, S.; Kampf, N.; Klein, J., Stability of self-assembled hydrophobic surfactant layers in water. *J. Phys. Chem. B* **2005,** *109* (9), 3832-3837.

[293] Ishida, N.; Kusaka, Y.; Ushijima, H., Effect of Electrolyte and Alcohol in Solution on the Hydrophobic Attraction between Alkoxylated Silica Surfaces. *Chem. Lett.* **2012,** *41* (10), 1273-1275.

[294] Donaldson, S. H.; Das, S.; Gebbie, M. A.; Rapp, M.; Jones, L. C.; Roiter, Y.; Koenig, P. H.; Gizaw, Y.; Israelachvili, J. N., Asymmetric Electrostatic and Hydrophobic–Hydrophilic Interaction Forces between Mica Surfaces and Silicone Polymer Thin Films. *ACS Nano* **2013,** *7* (11), 10094-10104.

Final Version as of April 20, 2018